

# Northumbria Research Link

Citation: Ramadan, Ahmed Mohamed (2017) Investigation of flow and heat transfer in a large-scale spent nuclear fuel cooling pond. Doctoral thesis, Northumbria University.

This version was downloaded from Northumbria Research Link:  
<http://nrl.northumbria.ac.uk/id/eprint/42057/>

Northumbria University has developed Northumbria Research Link (NRL) to enable users to access the University's research output. Copyright © and moral rights for items on NRL are retained by the individual author(s) and/or other copyright owners. Single copies of full items can be reproduced, displayed or performed, and given to third parties in any format or medium for personal research or study, educational, or not-for-profit purposes without prior permission or charge, provided the authors, title and full bibliographic details are given, as well as a hyperlink and/or URL to the original metadata page. The content must not be changed in any way. Full items must not be sold commercially in any format or medium without formal permission of the copyright holder. The full policy is available online: <http://nrl.northumbria.ac.uk/policies.html>



**Northumbria  
University**  
NEWCASTLE



**UniversityLibrary**

**Investigation of Flow and Heat Transfer  
in a Large-Scale Spent Nuclear Fuel  
Cooling Pond**

**Ahmed Ramadan**

**Ph.D.**

**2017**

Investigation of Flow and Heat Transfer  
in a Large-Scale Spent Nuclear Fuel  
Cooling Pond

Ahmed Ramadan

A thesis submitted in partial fulfilment of  
the requirements of the University of  
Northumbria at Newcastle for the degree of  
Doctor of Philosophy

Research undertaken in the Faculty of  
Engineering and Environment

August 2017

## Abstract

The recent focus on nuclear power has led to the need for more efficient and economical methods of operating the Spent Nuclear Fuel (SNF) cooling ponds as well as complying with the strict safety and environmental legislations imposed by the IAEA and the UK Government. Like many other industrial applications, the design and operation of the SNF cooling ponds have evolved from experience; trial and error. Since the stored materials in such ponds are radioactive, it is very difficult to perform experimental studies. As a result, a rigorous scientific study based on fundamental principles has to be performed.

The present research explores analytically and numerically the main processes that take place across the pond installation. The body of the present study includes four main parts: the first part is involved in modelling the heat loss from the free water surface, mainly due to evaporation, using analytical and single-phase numerical approaches, which represents a critical factor in the modelling of the large-scale cooling ponds. The predicted results were in good agreement with experimental data available in open literature.

In the second part, a thermal model using Microsoft Excel spreadsheet was developed for the cooling pond based on an analytical approach. The well-mixed hypothesis was adopted to describe the water zone as well as the humid air zone. Also, the ventilation system was considered within this model. The developed spreadsheet tool was validated against reliable data available for Maine Yankee pool as well as temperature measurements collected from the Sellafield site. This spreadsheet tool is able to describe the transient behaviour with low computational cost, allowing many "what-if" scenarios to be rapidly investigated.

In the third part, Computational Fluid Dynamics (CFD) was used to model the cooling pond at both macro and micro levels. The macro level modelling involved in developing a CFD model for Sellafield's cooling pond where the fuel regions were approximated to porous medium. The computational domain was produced for the water zone only, where the humid air zone was introduced to the model by coupling of the spreadsheet model with the CFD model. This model was validated and used to examine the distribution of water temperature to confirm the reliability of the adopted well-mixed approach in the analytical model. The outcomes from the CFD and spreadsheet models were used to



provide some boundary conditions to the micro-level model of the fuel assemblies. The modelling methodology of the fuel assemblies was partially validated with experimental data for heat transfer around vertical cylinder. The maximum temperature of the water within the rack arrangement was determined under various conditions and a correlation was proposed.

Finally, a sensitivity study was performed using Taguchi method and the statistical method of ANOVA to assess the influence of the cooling systems as well as the environmental conditions on the thermal performance of the cooling pond. The spreadsheet model was implemented to carry out the calculations. The outcomes from this study were presented in the form of recommendations that may be able to aid the organisation to manage their cooling pond more efficiently and safely during the normal operating conditions as well as recovery from an accident scenario.

## Table of Contents

<b>Abstract.....</b>	<b>I</b>
<b>Table of Contents .....</b>	<b>III</b>
<b>List of Figures.....</b>	<b>VIII</b>
<b>List of Tables .....</b>	<b>XIII</b>
<b>Acknowledgment.....</b>	<b>XV</b>
<b>Declaration.....</b>	<b>I</b>
<b>Nomenclature.....</b>	<b>II</b>
<b>Chapter 1    Introduction .....</b>	<b>1</b>
1.1    Research background .....	1
1.2    SNF and waste management .....	2
1.3    Sellafield site.....	5
1.4    Research aims and objectives.....	7
1.5    Project methodology .....	8
1.6    Contribution to knowledge.....	9
1.7    List of publications.....	10
1.8    Thesis structure .....	10
<b>Chapter 2    Literature Review.....</b>	<b>12</b>
2.1    Introduction .....	12
2.2    SNF cooling ponds .....	12
2.3    Evaporation from free water surface.....	22
2.4    Studies on natural convection flow around vertical cylinders .....	29
2.5    Concluding remarks .....	36

<b>Chapter 3</b>	<b>Methodology of CFD Modelling and Data Analysis .....</b>	<b>38</b>
3.1	Introduction .....	38
3.2	CFD methodology .....	38
3.2.1	Continuity equation .....	39
3.2.2	Momentum conservation equation .....	39
3.2.3	Turbulence modelling .....	40
3.2.4	Energy conservation equation .....	43
3.2.5	Natural convection .....	44
3.2.6	Modelling porous media .....	44
3.3	Data analysis .....	46
3.3.1	Taguchi method .....	46
3.3.2	Analysis of variance (ANOVA) .....	47
3.3.3	Minitab software .....	48
<b>Chapter 4</b>	<b>Heat Loss from Water Surface Undergoing Free Evaporation .....</b>	<b>49</b>
4.1	Introduction .....	49
4.2	Analytical modelling of heat and mass transfer from water surface .....	49
4.2.1	Evaporation heat loss .....	50
4.2.2	Convection and radiation heat loss .....	53
4.2.3	Top surface heat transfer coefficient .....	54
4.3	Numerical modelling and validation .....	56
4.4	Considerations for high water temperatures .....	61
4.5	Summary .....	63

<b>Chapter 5</b>	<b>Analytical Modelling of SNF Cooling Pond.....</b>	<b>65</b>
5.1	Introduction .....	65
5.2	Sellafield spent fuel cooling ponds .....	66
5.3	Spreadsheet model .....	67
5.3.1	Modelling assumptions .....	68
5.3.2	Modelling methodology .....	68
5.3.3	Mass balance of water zone .....	70
5.3.4	Pond water elevation .....	71
5.3.5	Mass balance of humid air zone.....	72
5.3.6	Energy balance of water zone .....	74
5.3.7	Energy balance of humid air zone.....	75
5.4	Spreadsheet model validation .....	78
5.4.1	Validation with Maine Yankee pool data .....	78
5.4.2	Validation with Sellafield cooling pond data.....	81
5.5	Graphical user interface (GUI) of the spreadsheet model.....	83
5.6	Summary .....	87
<b>Chapter 6</b>	<b>Numerical Modelling of Sellafield SNF Cooling Pond .....</b>	<b>88</b>
6.1	Introduction .....	88
6.2	Modelling methodology .....	88
6.2.1	Geometry of the pond.....	89
6.2.2	Generation of the computational grid .....	92
6.2.3	Numerical model and boundary conditions .....	93

6.3	Model validation and verification .....	96
6.4	CFD results and discussion .....	98
6.4.1	Flow field and streamlines .....	99
6.4.2	Temperature profiles .....	102
6.5	Effect of recirculation and heat load distribution.....	105
6.6	Summary .....	112
<b>Chapter 7</b>	<b>Micro-Level Numerical Analysis of the Cooling Pond .....</b>	<b>114</b>
7.1	Introduction .....	114
7.2	Modelling of fluid flow and heat transfer around vertical cylinders .....	115
7.2.1	Modelling methodology .....	115
7.2.2	Performance of turbulence models.....	117
7.2.3	Heat transfer characteristics .....	120
7.2.4	Visualisation of surface temperature.....	122
7.3	Modelling of the fuel rack assembly .....	123
7.3.1	Flow field and streamlines .....	125
7.3.2	Temperature distribution.....	126
7.3.3	Determination of maximum water temperature .....	128
7.4	Summary .....	130
<b>Chapter 8</b>	<b>Study of Thermal Performance of the SNF Ponds Using Spreadsheet Model</b>	<b>132</b>
8.1	Introduction .....	132
8.2	Analysis of the pond thermal behaviour .....	132
8.2.1	Maximum heat load.....	132

8.2.2	Loss of cooling scenario.....	134
8.2.3	Rate of temperature increase.....	137
8.2.4	Impact of weather conditions.....	139
8.3	Sensitivity study.....	140
8.3.1	Screening process.....	141
8.3.2	ANOVA at different heat loads.....	147
8.3.3	Recommendations based on ANOVA results.....	154
8.4	Summary.....	156
<b>Chapter 9</b>	<b>Conclusion and Recommendations for Future Work.....</b>	<b>157</b>
9.1	Conclusion.....	157
9.2	Future work.....	159
<b>References</b>	<b>.....</b>	<b>161</b>
<b>Appendix A</b>	<b>Stability Analysis.....</b>	<b>175</b>
<b>Appendix B</b>	<b>Detailed Dimensions of Sellafield's Cooling Ponds.....</b>	<b>178</b>
<b>Appendix C</b>	<b>UDF for the Overall Heat Transfer Coefficient.....</b>	<b>179</b>

## List of Figures

Figure 1.1: Concept map of waste management options. ....	4
Figure 1.2: Decay heat as a function of time for different burn-ups [14]. ....	5
Figure 1.3. SNF cooling ponds at Sellafield site [15]. ....	6
Figure 2.1: Description of the transport processes within a water tank and evaporation from the free water surface. ....	23
Figure 2.2: Natural convection boundary layer on the lateral surface of the vertical cylinder [92]. ....	30
Figure 3.1. Effect of $y^+$ value on transition onset [17]. ....	42
Figure 3.2: Steps for Taguchi method. ....	47
Figure 4.1: Comparison of calculated evaporation rate and experimental data for Bower et al. [82]. ....	51
Figure 4.2: Plot of $m''$ versus $\Delta\rho v$ and $\Delta\rho/\rho_{av}$ over range of surface temperature. ....	52
Figure 4.3: Effect of relative humidity and water surface temperature on the evaporation rate. ....	53
Figure 4.4: Overall heat transfer coefficient at a range of water surface temperature and its curve-fit from Eq. (4.13). ....	55
Figure 4.5: Schematic of the water tank used in the experiment conducted by Bower et al. [82]. ....	56
Figure 4.6: Numerical results and experimental data reported by Bower et al. [82] during the cooling process of the water tank. ....	58
Figure 4.7: Temperature distribution and streamlines are shown on mid-section plane ( $t=600$ sec). ....	59
Figure 4.8: Distribution of localised heat loss from the free water surface ( $t=600$ sec). ....	60

Figure 4.9: Proportions of the heat transfer components over a range of surface temperature.....	61
Figure 4.10: Comparison of evaporation rates predicted using Stefan’s law and concentration difference definitions.....	63
Figure 5.1: Schematic diagram of Sellafield SNF cooling ponds.....	65
Figure 5.2: Description of the processes taking place within the pond installation.....	67
Figure 5.3: Zones used in the spreadsheet model. ....	67
Figure 5.4: Flowchart representation of the spreadsheet model. ....	69
Figure 5.5. Water temperatures that obtained by the spreadsheet model and Maine Yankee pool [45] under the accident case.....	80
Figure 5.6. Water level that obtained by the spreadsheet model and Maine Yankee pool [45] under the accident case.....	81
Figure 5.7: Contribution percentage of different heat removal modes for validation case 1, case 2, and case 3. ....	83
Figure 5.8: A snapshot of the GUI for Sellafield cooling pond (the first file).....	85
Figure 5.9: A snapshot of the GUI for Sellafield cooling pond (the second file). ....	86
Figure 6.1: 3-D view of the computational domain for the Sellafield cooling pond. ....	89
Figure 6.2: Cooling pond geometry and overall dimensions. ....	91
Figure 6.3: A close-up view of the mesh structure for the actual cooling pond. ....	93
Figure 6.4: Overall heat transfer coefficient of the water surface as a function of the surface temperature. ....	94
Figure 6.5: Volume average pond water temperature at steady state. ....	98
Figure 6.6: Increase of average pond water temperature. ....	98
Figure 6.7: Breakdown of planes used to display CFD results.....	99



Figure 6.8: Streamlines coloured by velocity magnitudes. ....	100
Figure 6.9: Velocity contours on chosen planes (a) at the water top surface, (b) on Y-1 plane and (c) on Y-2 plane. ....	101
Figure 6.10: Velocity contours on X-2 plane at the inlet pond. ....	102
Figure 6.11: Temperature profiles on chosen planes (a) at the water top surface, (b) on Y-1 plane and (c) on Y-2 plane. ....	103
Figure 6.12: Temperature profiles on Z-2 plane. ....	103
Figure 6.13: Temperature profiles on X-2 plane at the inlet pond. ....	104
Figure 6.14: Heat loss from the water top surface. ....	104
Figure 6.15: Breakdown of pond sections. ....	107
Figure 6.16: CFD temperature distribution for make-up flow rate of 57.5 kg/s under different recirculation and fuel locations: (a) both ponds, (b) Pond A, and (c) Pond B. ....	108
Figure 6.17: CFD temperature distribution for make-up flow rate of 115 kg/s under different recirculation and fuel locations: (a) both ponds, (b) Pond A, and (c) Pond B. ....	110
Figure 7.1: Half geometry of the fuel rack assembly. ....	115
Figure 7.2: Sketch of the experimental apparatus used by Kimura et al. [103]. ....	116
Figure 7.3: Grid distribution of the computational domain. ....	117
Figure 7.4: Local heat transfer coefficient for $d = 10$ mm. ....	118
Figure 7.5: Local heat transfer coefficient for $d = 26$ mm. ....	119
Figure 7.6: Local heat transfer coefficient for $d = 165$ mm. ....	119
Figure 7.7: Water dynamic viscosity and thermal conductivity distributions along the cylinder surface for $d = 10$ mm. ....	120

Figure 7.8: Comparisons of a local Nusselt number for different diameters (a) $d = 10$ mm, (b) $d = 26$ mm, and (c) $d = 165$ mm. ....	121
Figure 7.9: Numerical and experimental [103] temperature distribution along the cylinder surface (a) $d = 10$ mm, (b) $d = 26$ mm, and (c) $d = 165$ mm. ....	122
Figure 7.10: Computational grid for a fuel assembly. ....	124
Figure 7.11: Streamlines of the flow through the rack arrangement. ....	125
Figure 7.12: Velocity contour on the symmetry plane. ....	126
Figure 7.13: Vector field on the symmetry plane. ....	126
Figure 7.14: Temperature profiles on the symmetry plane. ....	127
Figure 7.15: Temperature distributions on the horizontal planes at (a) $Y = 1$ m and (b) $Y = 3$ m measured from the bottom. ....	128
Figure 7.16: Maximum Temperature difference as a function of the heat flux and pond temperature. ....	130
Figure 8.1. Water and air temperatures of the cooling pond under the maximum heat load. ....	133
Figure 8.2. Contribution of different heat removal modes under the maximum heat load. ....	134
Figure 8.3. Water temperature during the loss of cooling scenario and after injection of make-up water. ....	135
Figure 8.4. Water level during the loss of cooling scenario and after injection of make-up water. ....	136
Figure 8.5. Water temperature under different heat loads for the Sellafield spent fuel cooling ponds. ....	137
Figure 8.6: Rate of temperature increase per day for different heat load values. ....	138
Figure 8.7: Time to reach steady state for different heat load values. ....	139

Figure 8.8. Effect of outside ambient air temperature on water temperature assuming 0% relative humidity. ....	140
Figure 8.9. Effect of outside relative humidity on water temperature assuming an air temperature of 25 °C. ....	140
Figure 8.10: Comparison between PCRs obtained by Taguchi method and full factorial design. ....	147
Figure 8.11: PCR of the input parameters for heat load of 1 MW. ....	149
Figure 8.12: PCR of the input parameters for heat load of 2 MW. ....	149
Figure 8.13: PCR of the input parameters for heat load of 5 MW. ....	150
Figure 8.14: PCR of the input parameters for heat load of 10 MW. ....	150
Figure 8.15: Effect of heat load on the PCR of the outside air temperature. ....	152
Figure 8.16: Effect of heat load on the PCR of the cooling tower efficiency. ....	152
Figure 8.17: Effect of heat load on the PCR of the ventilation inlet flow rate. ....	153
Figure 8.18: Effect of heat load on the PCR of the make-up water flow rate. ....	153
Figure 8.19: Effect of heat load on the PCR of the recirculation flow rate. ....	154
Figure 8.20: Illustration of the main events during the loss of cooling scenario and recommended reactions to be taken. ....	155

## List of Tables

Table 2.1: Summary of the key literature on the spent fuel ponds. ....	19
Table 2.2: Comparison between previous studies for $Sh - Ra$ power law parameters....	28
Table 2.3: Selected literature on natural convection from vertical cylinder. ....	34
Table 4.1: Thermodynamic constants for physical properties of water [105]. ....	57
Table 5.1. Input data and comparison between values predicted by the spreadsheet model and data for the Maine Yankee pool [45].....	79
Table 5.2. Breakdown of the heat generated from the fuel assemblies.....	81
Table 5.3. Input parameters used in validation with the Sellafield spent fuel cooling ponds data. ....	82
Table 5.4. Comparison between measured and predicted results for Sellafield pond. ...	83
Table 6.1: Comparison between different time step sizes.....	96
Table 6.2: comparison between different mesh sizes.....	96
Table 6.3: Parameters used in the transient calculations of the validation exercise. ....	97
Table 6.4: Parameters used in the study of the effect of recirculation and heat load distribution on the uniformity of water temperature for a heat load of 10 MW. ....	106
Table 6.5: Summary of water temperature for test cases with a make-up flow rate of 57.5 kg/s. ....	111
Table 6.6: Summary of water temperature for test cases with a make-up flow rate of 115 kg/s. ....	112
Table 7.1: Pond temperature and heat flux used in the parametric study. ....	129
Table 8.1: Configurations used in the case of normal operating conditions.....	133
Table 8.2: Input parameters and levels used in the screening process.....	143

Table 8.3: Experimental design of $L_{32}(2^7)$ Taguchi orthogonal array.....	145
Table 8.4: Summary of ANOVA for the screening process using Taguchi method.....	146
Table 8.5: Input parameters and levels used in the ANOVA analysis with 5 input parameters. ....	148

## Acknowledgment

First and foremost, I must thank Almighty Allah for giving me the courage, determination and guidance in conducting this work.

My special thanks go to my supervision team Dr Reaz Hasan and Dr Roger Penlington, for their invaluable guidance, encouragement and support over the duration of this work.

This research is supported by Sellafield Ltd. which is gratefully acknowledged. We are especially grateful to John Rowley and Bob Burns for their support and the detailed information provided.

I would like to express my appreciation to my beloved parents for their continuous support and wisdom over the course of my academic journey. Furthermore, I would like to thank my sisters for their care and assistance throughout my years of education. Special thanks, of course, are due to my loving wife for her love, support, care and patience since the beginning of this work.

Also, I am indebted to my colleagues and friends for providing an enjoyable and fun environment. Many thanks are due to the academic and technical staff at Northumbria University for their support and encouragement.

Ahmed Ramadan  
*Northumbria University*  
August 2017

## Declaration

I declare that the work contained in this thesis has not been submitted for any other award and that is all my own work. I also confirm that this work fully acknowledges opinions, ideas and contributions from the work of others.

I declare that the Word Count of this Thesis, excluding bibliography and appendices, is 37012 words.

Name: Ahmed Ramadan

Signature:

Date: August 2017

## Nomenclature

$a$	thermodynamics constant
$A$	surface area ( $\text{m}^2$ )
$B$	$Sh - Ra$ power law coefficient
$c$	coefficient depends on wind speed
$C$	specific heat capacity ( $\text{J/kg K}$ )
$C_p$	specific heat capacity at constant pressure ( $\text{J/kg K}$ )
$d$	diameter ( $\text{m}$ )
$D$	mass diffusivity of water vapour in air ( $\text{m}^2/\text{s}$ )
$Gr$	Grashof number, $Gr = g\Delta\rho L^3/\rho\nu^2$
$H$	height ( $\text{m}$ )
$h_c$	convection heat transfer coefficient ( $\text{W/m}^2 \text{K}$ )
$h_{con}$	condensation mass transfer coefficient ( $\text{m/s}$ )
$h_e$	evaporation mass transfer coefficient ( $\text{m/s}$ )
$h_v(T)$	enthalpy of vapour at a given temperature ( $\text{kJ/kg}$ )
$h_{fg}$	latent heat of vaporization for water ( $\text{kJ/kg}$ )
$k$	thermal conductivity ( $\text{W/m K}$ )
$L$	characteristic length
$m$	mass ( $\text{kg}$ )
$\dot{m}$	mass flow rate ( $\text{kg/s}$ )
$\dot{m}_e''$	evaporation mass flux ( $\text{kg/s m}^2$ )
$M$	molecular weight ( $\text{kg/kmol}$ )
$N$	mole number ( $\text{kmol}$ )
$\dot{N}$	molar flow rate ( $\text{kmol/s}$ )
$Nu$	Nusselt number, $Nu = h_c L/k$



$P$	pressure (Pa)
$Per$	perimeter (m)
$Pr$	Prandtl number, $Pr = \nu/\alpha$
$q$	heat flux (W/m <sup>2</sup> )
$\dot{Q}$	heat transfer rate (W)
$Ra$	Rayleigh number, $Ra = g\beta\Delta TL^3/\alpha\nu$
$RH$	relative humidity (%)
$R_o$	universal gas constant (J/K kmol)
$Sc$	Schmidt number, $Sc = \nu/D$
$Sh$	Sherwood number, $Sh = h_m L/D_m$
$T$	temperature (K)
$V$	Volume (m <sup>3</sup> )
$W$	tank width (m)
$x$	wall thickness (m)
$y$	mole fractions
$\Delta t$	time step size (s)
$Z$	tank depth (m)

**Greek symbols**

$\alpha$	thermal diffusivity (m <sup>2</sup> /s)
$\beta$	coefficient of volumetric expansion (1/K)
$\delta_T$	thermal boundary layer thickness (m)
$\varphi$	thermodynamics property
$\varepsilon$	emissivity
$\theta$	rate of temperature increase (°C/day)
$\mu$	dynamic viscosity (N/m <sup>2</sup> s)

$\nu$	kinematics viscosity ( $\text{m}^2/\text{s}$ )
$\rho$	density ( $\text{kg}/\text{m}^3$ )
$\sigma$	Stefan Boltzmann constant ( $\text{W}/\text{m}^2 \text{K}^4$ )
$\zeta$	cooling tower efficiency

**Subscripts**

$a$	dry air
$av$	average value
$\infty$	ambient
$b$	bulk
$c$	convection
$con$	condensation
$cr$	critical value
$d$	decay heat
$D$	designed value
$e$	evaporation
$h$	hall
$l$	leakage
$m$	make-up
$p$	pond
$r$	radiation
$R$	rack
$s$	surface
$sat$	saturation
$t$	total
$v$	vapour

<i>vent</i>	ventilation
<i>w</i>	water
<i>x</i>	local value

**Acronyms**

ANOVA	Analysis of Variance
CFD	Computational Fluid Dynamics
EVM	Eddy Viscosity Models
GUI	Graphical User Interface
ISFSI	Independent Spent Fuel Storage Installations
MEB	Multi-Element-Bottle
NPP	Nuclear Power Plant
PCR	Percentage Contribution Ratio
PWR	Pressurized Water Reactor
SFM	Spent Fuel Management
SNF	Spent Nuclear Fuel
UDF	User-Defined-Function

# Chapter 1 Introduction

## 1.1 Research background

For several decades, the conventional technology for the generation of electricity has mainly relied on the burning of fossil fuels [1]. However, the limited sources of fossil fuels and the high levels of CO<sub>2</sub> emissions have prompted an interest in alternative ways of power production. Enhanced interest in recent years of utilising nuclear power for electricity generation has gained increased attention due to its significant advantages over fossil fuels. Despite this, there remains a debate over implementing this technology amongst engineers, scientists, decision makers and even the public, as issues surrounding its safety in normal operating conditions as well as accident scenarios come into scrutiny. This debate even increased, particularly, following the recent disaster of Fukushima Daiichi Nuclear Power Plant (NPP), Japan on March 11, 2011, when Fukushima city was hit by an earthquake about 110 miles off the coast. At this time, three reactors were in operation, and automatic emergency shutdown began. After several minutes, tsunamis started to hit the site resulting in flooding the facilities and shutting off the emergency power supply to units 1, 2, 3 and 4 in addition to waste fuel ponds [2, 3]. More information regarding this incident and the timeline of events that led to the damage of the units and the fuel pond can be found in this reference [4].

A further disadvantage of using nuclear power to generate electricity is that it produces radioactive waste products such as Spent Nuclear Fuel (SNF), which remains radioactive for many years before it goes into long-term storage. The issue of long-term storage was not taken very seriously when initial decisions were made regarding the fuel cycle [5]. Traditionally, SNF received a lot less attention than the reactor itself. Recently, waste management has become one of the major policy issues in most of the nuclear power programmes around the world. This because of that the chosen options for waste management can have a significant effect on the political debates, propagation risks, environmental threats, and economic costs of the nuclear fuel cycle.

While the SNF is still radioactive, the fuel can be stored in either wet or dry interim storages before it goes to its final repository. In the current study, the effort was devoted to the wet storages, where the SNF is held under water in SNF cooling ponds to prevent the radiation emissions being released to the environment. SNF cooling ponds consist of a large water pool contained in heavy concrete walls, where evaporation takes place from the free water surface to provide some cooling to the water body. The SNF can be stored in fuel rods surrounded by a circular Multi-Element-Bottle (MEB) or a rectangular fuel container to allow heat exchange [6]. MEB's are stacked under water on racks specifically designed in such a way that they are always kept immersed to prevent radiation leakage. While the fuel assemblies are submerged under the water level, the generated heat from the fuel causes a density variation within the water layers resulting in initiating a natural convection current. This density difference along with the gravity produces buoyancy forces, which cause the hotter water to move upwards and the colder water to go downwards, inducing a buoyancy driven flow. Water pumps are used to maintain a steady stream of water to avoid any risk of overheating or losing of the pond water level due to water loss via evaporation.

Investigations and experience suggest that some SNF cooling ponds can be a reliable method for storage for up to 30 years [5]. However, longer periods are required allowing enough time while developing more permanent solutions for waste management [7, 8].

## **1.2 SNF and waste management**

In the past decades, implementation of the nuclear power for electricity generation has gained much attention amongst the scientific society. As a result, the nuclear reactors around the world are discharging a large amount of a spent nuclear fuel which is expected to be approximately 445,000 t HM (metric tonnes of heavy metal) by 2020 [9]. This includes 69,000 t in Europe and 60,000 t in North America. Despite the recent incident of Fukushima, Japan [10], the nuclear power generation continue to grow in developed countries. This can be evidenced by the recent massive investment in the nuclear power by the UK government by approving £18bn nuclear plant at Hinkley Point C which will deliver 7% of Britain's electricity needs for the next six decades [11].

After the reactor is shut down for refuelling, the discharged SNF is sent to interim storage before it goes to its final destination. Figure 1.1 represents the main available options of nuclear waste management. The interim storages can be either at or away from the reactor site. Each option can have two configurations; wet or dry storage, where the former is the commonly used option. If the storage capacity at reactor site cannot keep up with the incoming SNF, it can be sent to centralised SNF cooling ponds or Independent Spent Fuel Storage Installations (ISFSI), which is dry storage. In the wet storage, water or boric acid is used as heat transfer medium to provide cooling to the fuel assemblies as well as shielding to prevent the radioactive materials of reaching the environment. In the dry storage, air is used as the heat transfer medium, and the cooling is achieved by maintaining natural or forced air circulation. There are substantial differences between wet and dry storage regarding design and cost. However, both can be safe methods. Wet storage usually requires more operational attention as it consists of a large number of mechanical components such as pumps, piping and other instrumentation. Besides, there is the risk associated with water leakage from the pond, which may be contaminated with radioactive materials and can affect the environment. On the other hand, the dry storage is much simpler in operation, as it is almost entirely passive. This offers a lot fewer chances for human error as well as mechanical failures. However, dry storage is not suitable for high-level waste, especially when it is coming out just after the reactor has been shut down. In some occasions, the high-level waste can be stored in dry storage after it has been stored in a wet storage facility for few years.

The SNF continuously generate heat due to the decay of residual radioactive elements. When the SNF is just discharged from the reactor core, the decay heat can be up to around 6.5% of the previous core power. During the first week, the decay heat drops very rapidly to 0.2% of the previous core power [12]. The following relationship can be used to estimate the decay heat, which is valid from 10 seconds up to 100 days [13].

$$\frac{\text{decay power}}{\text{reactor power before shutdown}} = 0.066[(t - t_s)^{-0.2} - t^{-0.2}] \quad (1.1)$$

where  $t$  is the time since reactor start-up and  $t_s$  is the time of reactor shutdown measured from the time of start-up.

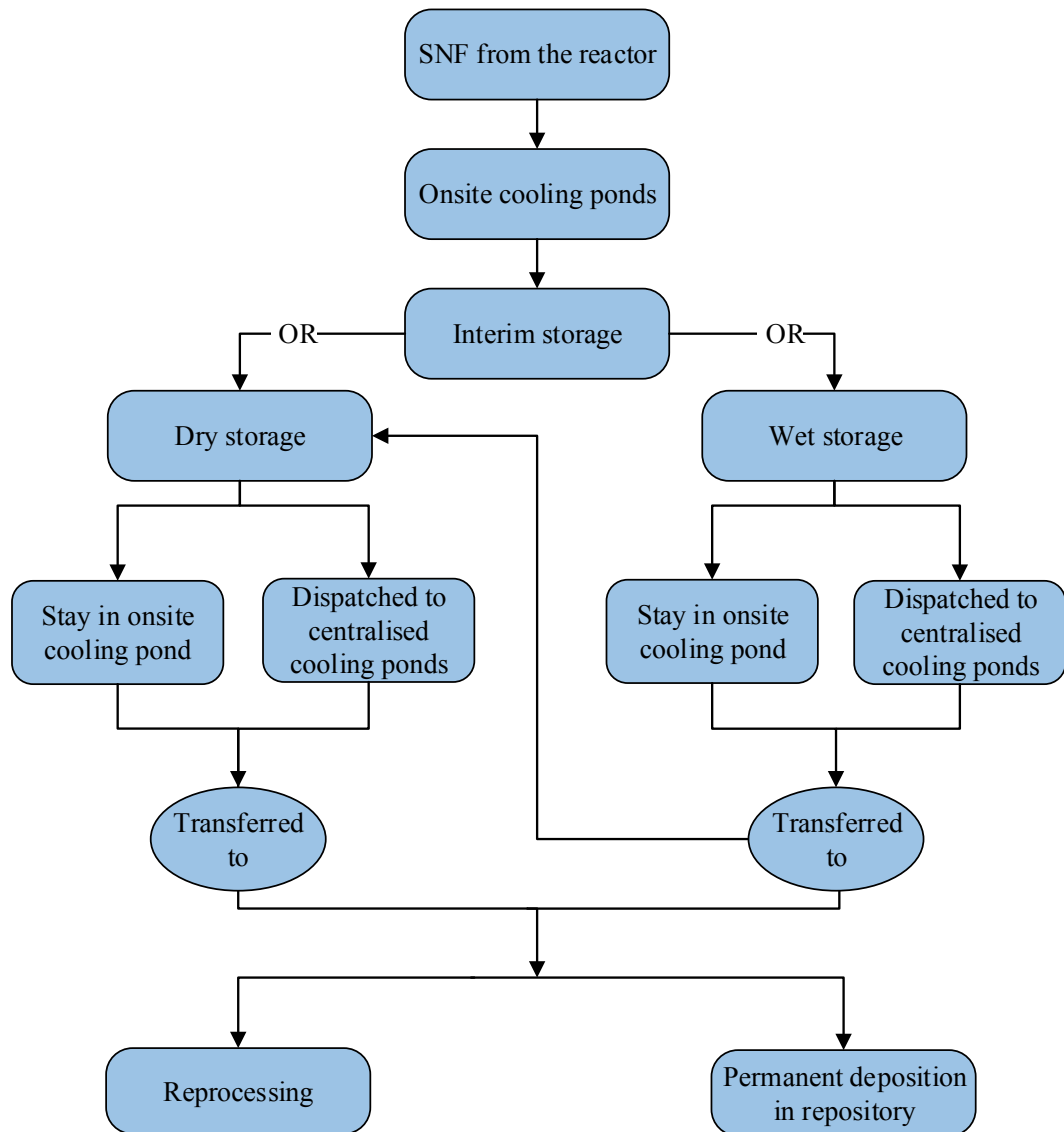


Figure 1.1: Concept map of waste management options.

Figure 1.2 shows how the decay heat drops over a period starting from about one week after the reactor shutdown up to 100 years. It can be seen that, after one year, the decay heat decreases by about 90% of its initial value.

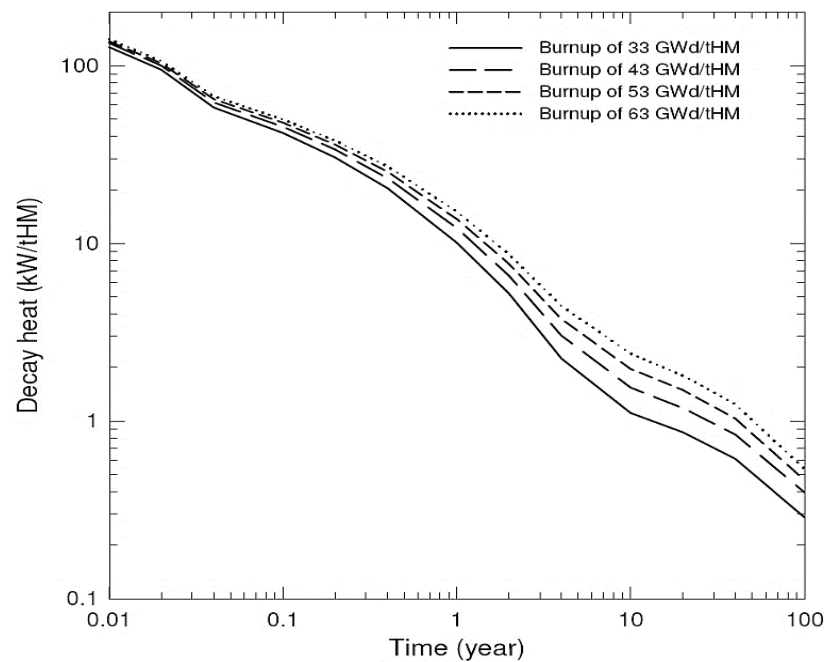


Figure 1.2: Decay heat as a function of time for different burn-ups [14].

### 1.3 Sellafield site

Sellafield Ltd is the company responsible for safely delivering the reprocessing and nuclear waste management activities, decommissioning, and clean-up of the UK's civil nuclear legacy. Spent Fuel Management (SFM) at Sellafield includes the reprocessing of spent Magnox nuclear fuel from stations across the UK and also the reprocessing of spent oxide fuel from other countries. Reprocessing takes used fuel which has been removed from a nuclear reactor for recovery of reusable materials. After about four years in a reactor, the fuel becomes economically unviable. Reprocessing allows around 97% of this used fuel to be recycled back into new fuel. SFM also includes the storage of spent nuclear fuel that is going for reprocessing. Figure 1.3 shows photographs of the cooling ponds at the Sellafield site.



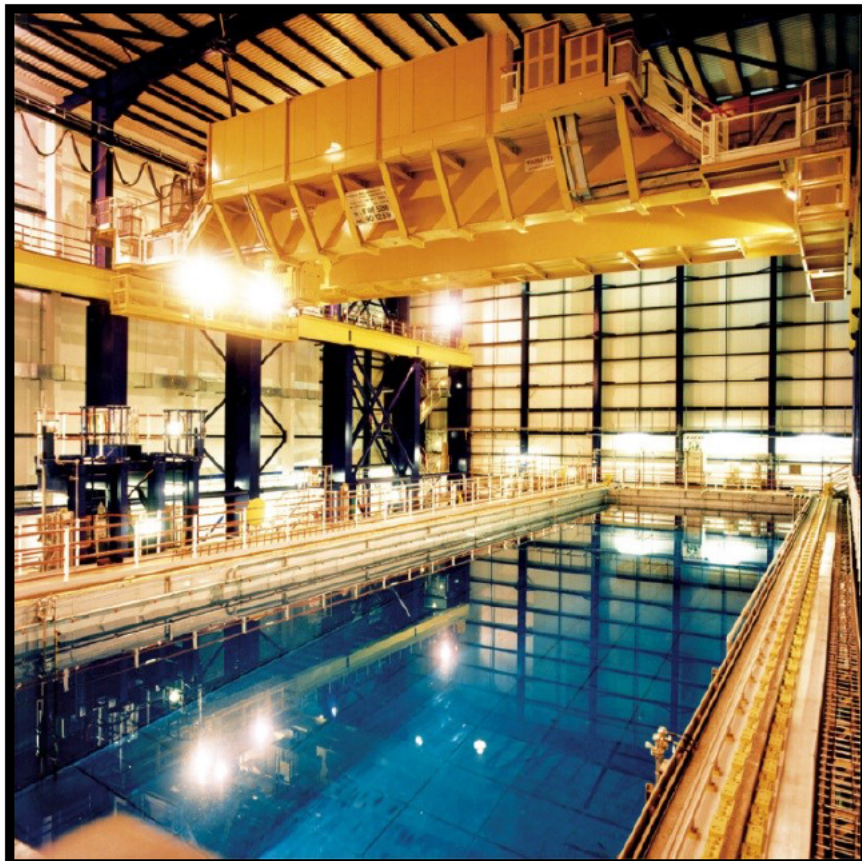
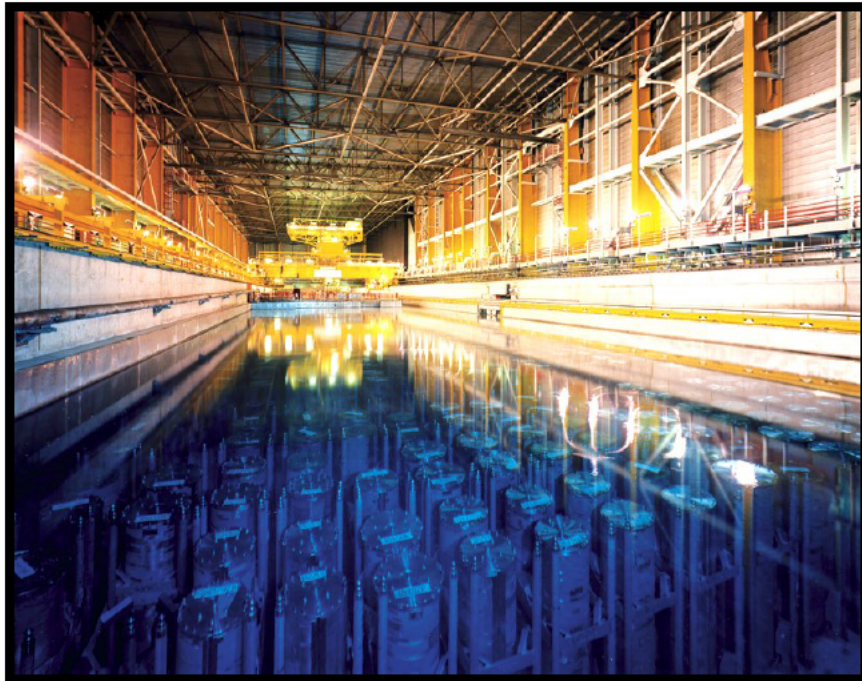


Figure 1.3. SNF cooling ponds at Sellafield site [15].

## 1.4 Research aims and objectives

The primary goal of the proposed research is to investigate and analyse the flow and heat transfer in a large-scale spent nuclear fuel cooling ponds. Another goal is to develop a spreadsheet-based user-friendly tool to aid the organisation in the operation of their cooling ponds more efficiently. To achieve the above aims, the following objectives were set.

- i. Establish a valid methodology for estimating the heat loss from the free water surface. This will involve modelling the heat loss from the water surface using analytical and numerical approaches.
- ii. Produce an analytical model for the cooling pond taking into account the water body as well as the volume of humid air above the water surface. In this part, Excel spreadsheet tool will be used to produce the analytical model of the SNF cooling ponds.
- iii. Generate a valid CFD model for the water body of the cooling pond. This will involve creating an efficient mesh for the Sellafield cooling pond to reduce computing time and hence allowing several parametric studies to be performed more rapidly.
- iv. Conduct parametric study for different operation conditions using the CFD model of the SNF cooling ponds. This study will be focused on examining the effect of the recirculation pump on the distribution of the water temperature. Also, different layouts of loading the fuel inside the cooling ponds will be explored.
- v. Establish a numerical methodology to model the free convection heat transfer from vertical cylinder. This methodology will be used to produce a CFD model of the fuel arrangement to study the micro behaviour of the pond.
- vi. Perform a comprehensive sensitivity study using statistical methods. The spreadsheet model will be used to perform the calculations. This study will help to understand the effect of the cooling systems and the environmental conditions on the performance of the cooling ponds.

## 1.5 Project methodology

The research work will consist of analytical and numerical investigations. In order to establish a CFD model for SNF cooling ponds, actual temperature measurements will be compared against the CFD results. After that, a number of parametric studies will be performed dealing with various operational conditions. As a result, a user-friendly spreadsheet will be developed to provide the organisation with an efficient tool to assist in the operation of the cooling ponds.

### 1.5.1.1 *Analytical part*

It was evidenced that the numerical model for the SNF cooling pond is computationally very demanding, as it requires the use of multiphase models. Therefore, the numerical approach alone may not be an efficient practice. One other approach to model the SNF cooling ponds is to analytically model the governing phenomena within the pond structure and generate a user-friendly Excel spreadsheet, which allows many "what-if" scenarios to be rapidly investigated without repetitive calculation. However, the analytical approach does not provide localised information for the temperature distribution within the water body. Also, the outcomes from the analytical model will be coupled with the numerical model to specify the boundary condition at the free water surface.

### 1.5.1.2 *Numerical part*

CFD technique will be implemented to predict flow field and heat transfer in the SNF cooling ponds on a macro level. This methodology is well-known and has been used in a wide range of applications [16]. In this study, the CFD package ANSYS Fluent software will be used to develop the numerical model for the cooling ponds [17]. In some cases, User-Defined-Function (UDF) will be introduced to the CFD solver to specify the material properties as well as appropriate boundary conditions for heat transfer.

The outcomes of the macro model will be used to provide some boundary conditions to the micro model of the rack assemblies. Another use of the CFD approach will be in the modelling of the fluid flow and heat transfer around vertical cylinders to provide some validation for the used methodology in the fuel rack modelling.

### **1.5.1.3 *Analysis of the cooling ponds behaviour***

In this part, Taguchi method and the statistical method of ANOVA will be used to assess the influence of the cooling systems and the environmental conditions on the thermal performance of the cooling pond.

## **1.6 Contribution to knowledge**

Study of the existing literature shows that investigations on the SNF cooling ponds have been mainly focused on ponds located at the reactor site, which is relatively small in size. Also, the analysis of the cooling ponds is almost always restricted to accident scenarios and related topics. This shows the importance of modelling and analysing the behaviour of the large-scale ponds under accident scenarios as well as under normal operating conditions. The following points summarise the main contribution to original knowledge.

- A numerical methodology for modelling heat loss from the water surface undergoing free evaporation using single-phase flow was established. This would be much less resource intensive without compromising the accuracy.
- A spreadsheet model of the cooling pond was produced taking into account the water zone and volume of humid air above the water surface. This model is validated and used in the operation of Sellafield SNF cooling ponds.
- A three-dimensional CFD model was developed and validated for a large-scale cooling pond considering the water zone. To the best of our knowledge, this is the first study for such large-scale pond.
- A comparative performance of five RANS turbulence models for computation of heat transfer characteristics of vertical cylinder involving flow transition from laminar to turbulent. This will be useful to model flow in situations where a large number of heated cylinders are involved.
- A comprehensive analysis of the SNF cooling pond behaviour was carried out using ANOVA analysis. Findings from this analysis would be useful for day-to-day operation, strategic planning and future development to ensure safety.

## 1.7 List of publications

- [1] Ramadan, A, Hasan, R and Penlington, R, “*A Single-Phase Flow Approach for Modelling Spent Nuclear Fuel Cooling Ponds*”. To be submitted to Applied Thermal Engineering in September 2017.
- [2] Ramadan, A, Hasan, R and Penlington, R, “*Comprehensive Analysis of Spent Fuel Cooling Ponds using ANOVA Approach*”. To be submitted to Progress in Nuclear Energy in September 2017.
- [3] Ramadan, A, Hasan, R and Penlington, R, “*Spreadsheet Transient Model of Large-Scale Cooling Ponds using Well-Mixed Approach*”. Submitted to Annals of Nuclear Energy in July 2017.
- [4] Ramadan, Ahmed, Hasan, Reaz and Penlington, Roger (2016) *Analytical and Numerical Modelling of Spent Fuel Cooling Ponds*. In: 2<sup>nd</sup> International Conference on Advances in Mechanical Engineering, 10-13 May 2016, Istanbul, Turkey.
- [5] Ramadan, Ahmed, Hasan, Reaz and Penlington, Roger (2016) *Modelling Heat Transfer from Water Surface Undergoing Free Evaporation*. In: IX International Conference on Computational Heat and Mass Transfer, 23-26 May 2016, Cracow, Poland.
- [6] Ramadan, Ahmed, Hasan, Reaz and Penlington, Roger (2015) *Numerical Simulation of Flow and Heat Transfer around Vertical Cylinder Submerged in Water*. In: UK Heat Transfer Conference, 7-8 September 2015, Edinburgh University.
- [7] Hasan, Reaz, Tudor, Jenna and Ramadan, Ahmed (2015) *Modelling of Flow and Heat Transfer in Spent Fuel Cooling Ponds*. In: International Congress on Advances in Nuclear Power Plants, 3-5 May 2015, Nice, France.

## 1.8 Thesis structure

- Chapter 1 provides an introduction to spent nuclear fuel and waste management strategy. Also, it highlights research aims and objectives along with research methodology and contributions.
- Chapter 2 presents a comprehensive review of the studies that are relevant to the current research topic. The review focuses on the methods used to describe the thermal-hydraulic processes within the cooling ponds as well as the type of the

analyses that were carried out. Also, this chapter discusses the evaporation phenomenon from water surface and natural convection heat transfer around heated vertical cylinders.

- Chapter 3 describes the main governing equations of the CFD method, which addresses the flow and heat transfer in the cooling pond. Additionally, the statistical methods of Taguchi and ANOVA are discussed, and will be used to perform the sensitivity study and analyse its results.
- Chapter 4 focuses on establishing a single-phase flow numerical methodology for modelling heat loss from a water surface undergoing free evaporation. Also, it presents a comparison of results with experimental data from the literature.
- Chapter 5 describes an analytical model of a large-scale cooling pond based on well-mixed hypothesis using Microsoft Excel spreadsheet. This model is validated against reliable data reported in the literature as well as some measurements collected from Sellafield site to examine its reliability under large-scale ponds.
- Chapter 6 reports numerical modelling of Sellafield's cooling pond coupled with the spreadsheet analytical model. The model is validated with data from the Sellafield site. This model is used to examine the validity of the well-mixed approach in the spreadsheet model as well as to examine the effect of the recirculation on the uniformity of the water temperature.
- Chapter 7 reports CFD analysis of the fuel assemblies to study its thermal-hydraulic characteristics. It also provides modelling methodology of natural convection heat transfer around vertical cylinder, which forms a validation exercise of the modelling methodology of the fuel assemblies.
- Chapter 8 analyses the thermal behaviour of the pond under normal operating conditions as well as at accident scenario using the spreadsheet model. Also, a sensitivity study is conducted using Taguchi method and the statistical method of ANOVA to assess the effect of the operational configurations on the cooling performance. Some recommendations to aid the organisation to manage their cooling pond more efficiently are also discussed in this chapter.
- Chapter 9 summarises the major findings, presents the main conclusion from this study, and proposes recommendations for future investigations.

## Chapter 2 Literature Review

### 2.1 Introduction

This chapter presents the literature relevant to our research investigation. As highlighted in the previous chapter, the work involves investigation of the heat and mass transfer in SNF cooling ponds with an emphasis on fundamental understanding of the thermo-fluid processes that determine the operation of the ponds. Due to such a broad scope and in line with our thesis presentation, the literature is also divided under three major sections. In section 2.2, the relevant studies that were focused on the overall SNF cooling ponds are discussed. In this category it was found two different kinds of methodology one that uses the CFD and another that uses so-called ‘system codes’. In section 2.3, the effort was devoted to the literature related to passive evaporation from water bodies – the reason being that this forms the most dominant mode of heat loss from the water surface and hence forms an important fundamental process. In section 2.4, literature on flow and heat transfer from vertical heated cylinders are considered. The reason is that the fuels that are stored under water can essentially be represented by vertical submerged cylinders. An understanding of such basic flow is essential in explaining the heat and fluid flow within the ponds. Finally, section 2.5 summarises the main findings from the literature which underpins the current investigation.

### 2.2 SNF cooling ponds

Following the recent incident of Fukushima Daiichi, rapid responses to the disaster are noted in the literature by the scientists. Some of these responses were in the form of study of the impact of leakage of the radioactive materials into the environment [18-21]. Nevertheless, other responses were focused on the analysis of accident scenario in the SNF cooling ponds where others have discussed mitigation measures. The interest in investigating and analysing the SNF cooling pond seems to be an ongoing issue as a result of the growth of the nuclear industry.

As mentioned before, the nuclear waste can be stored in either wet or dry storage. However, detailed and comprehensive review of this field of research is beyond the scope of the study, and an interesting and relevant research papers can be found in [22-34].

Several research investigations can be found in the open literature considered the thermal-hydraulic behaviour of the SNF cooling ponds, which are mainly focused on accident scenarios and its consequences. A summary of the published work on the spent fuel cooling ponds is shown in Table 2.1. In these studies, typically, there are two main approaches were implemented in these studies to analyse such cooling ponds: CFD and so-called system codes. Numerical methods such as CFD, in principle, can address details of thermo-fluid phenomena in cooling ponds. The CFD methodology is now well established, but the available literature indicates that a full CFD model of the spent fuel cooling pond has not been reported before. This is may be due to the existence of the evaporation phenomenon and hence involves the multiphase flow models. However, some studies have reported CFD modelling of the spent fuel ponds that is taking into account only the water body without considering the humid air zone and the ventilation besides their effect on the evaporation rate.

On the other hand, system codes such as RELAP, TRACE, ATHLET, MELCOR and ASTEC are based on dividing the system into a network of pipes, pumps, vessels, and heat exchangers. Mass, momentum and energy conservation equations are then solved in one-dimensional form. Many phenomena and physical behaviours such as two-phase flows and pressure drop due to friction rely on empirical correlations. These codes are suitable for systems that can be represented by one-dimensional flows. However, when such a system involves multi-dimensional phenomena, these codes do not provide a good approximation. Some attempts have been made to improve their capability to handle multi-dimensional flows. One of these attempts considers the system as an array of parallel one-dimensional pipes, where the interaction between them is allowed through cross-flow coupling. Although they provide improved approximations compared with purely one-dimensional approaches, these models do not offer appropriate descriptions of multi-dimensional flows. The MARS code is an example of attempts to include a multi-dimensional analysis capability in system codes [3].



A good example of typical implementations of the CFD approach is the work reported by Hung et al. [35] who have produced a 3-D model to predict the cooling capability of Kuoshen spent fuel pool. Besides, to examine the reliability of the existing configuration to provide an adequate cooling to maintain the maximum water temperature below 60 °C in order to meet the licensing regulations. A unique aspect of their work is that they have used the CFD in a more advanced way than most other reported studies to predict the local boiling within the pool water, which reflects the strength of the CFD approach. In their model, the fuel region was considered as a single porous medium zone, and the heat transfer from the free water surface was treated using the heat and mass transfer analogy. However, no validation was provided to confirm the reliability of such assumptions.

Ye et al. [36] have used the CFD approach to design a new passive cooling system to provide an adequate cooling to CAP1400 spent fuel pool in the emergency situations. This system is based on implementing the cooling technology of the high-efficiency heat pipe. In a different paper from the same authors [37], experimental investigations were carried out to confirm the reliability of using such heat pipe to remove the decay heat as well as to study its thermal performance under different conditions. In their experiment, the test rig was simplified to include heat pipe with only one evaporator and one condenser. They showed that a single set of evaporator and condenser is able to remove about 10.5 kW of heat.

Yanagi et al. [38] developed a 3-dimensional numerical model of Fukushima Daiichi cooling pond considering the water body only to evaluate heat loss and water temperature. The heat loss from the free water surface was estimated based on a correlation that was experimentally derived in the same study. However, this correlation is valid only for air velocity ranging between 0.33 to 2.08 m/s. Fuel assemblies were simplified to a porous medium where the decay heat was assumed to be uniformly distributed. The authors noted that the variations between the water temperatures were small except regions near to the water surface. Also, it was confirmed that the heat loss from the concrete walls is small, about one order of magnitude smaller, compared to the heat transfer from the water surface. In a different paper from the same authors [39], the CFD model was further extended to predict the pond behaviour after the shutdown of its cooling system.

CFD approach can be used to study the flow and heat transfer characteristics within fuel assemblies, for example, the study conducted by Chen et al. [40]. They have investigated the flow and heat transfer within a 17 x 17 rod bundle using a three-dimensional model. The computational grid was generated with 16 million cells. A heat flux of about 2 kW was assumed uniformly distributed on the outer surface the fuel rod. This heat flux is not high enough to realise the turbulent flow, and hence the flow is considered laminar. They observed that the flow characteristics within the rod bundle are significantly affected by the support grids. Moreover, they have shown that the predicted Nusselt number from the CFD is higher than the correlation proposed by Churchill and Chu [41], which is adopted in RELAP5 code.

On the other hand, most of the studies that have adapted the system codes were concerned with investigating the accident scenarios and analysing its consequences. The study of the accident scenario can be broadly split into two categories (a) loss of cooling analysis and (b) loss of coolant analysis. In the first category, the typical analysis is to evaluate the change in the water temperature as well as the drop in the water level. Once the fuel assemblies start to uncover, the loss of coolant analysis is conducted to determine the increase in the fuel cladding temperature and the rate of hydrogen generation around the pond periphery.

Ahn et al. [42] investigated severe accident scenario in OPR1000 spent fuel pond located in a typical Pressurized Water Reactor (PWR) using MELCOR software [43]. The investigations were carried out under three different conditions: loss of cooling, loss of coolant and complete loss of coolant. Under these circumstances, they estimated the timeline of three events: (a) fuel assemblies uncovering, (b) pool dry-out and (c) cladding oxidation. Such predictions are very useful from risk and accident management point of view to evaluate the time available to take appropriate actions.

Chen et al. [44] used GOTHIC code to model the spent fuel pool Mark III, which is owned by Taiwan Power Company, to analyse the pool behaviour under loss of coolant scenarios. The response of the pool to spray mitigation was examined under loss of coolant situations for large and small leakages. They showed that the pool spray can compensate the water loss and maintains the water level above the fuel assemblies only for small leakages. On the other hand, high leakages can drain off the full water allowing

air to flow through the fuel assemblies resulting in enhancement of the cooling effect. The worst case was when the fuel region was partially uncovered where it cannot be cooled by neither water nor air. However, the peak cladding temperature was well below the critical level.

Carlos et al. [45] conducted an investigation on Maine Yankee spent fuel pool to assess the reliability of TRACE best estimate code to simulate the thermal-hydraulic behaviour of such ponds under steady and transient conditions. The steady state calculations were performed to simulate the pool under normal operating conditions as well as licensing case where the maximum possible amount of spent fuel is stored in the pond. The transient calculation was carried out to study the pond behaviour under loss of cooling and loss of coolant scenarios. No heat transfer was considered to take place from the free water surface except the boiling heat transfer. The water surface area is 142 m<sup>2</sup>, and the water level is 11.1 m. The results obtained by the TRACE code were compared with previously reported actual measurements and predicted data by GFLOW software for the licensing case [46]. From the comparison, they observed a good agreement TRACE results and data for Maine Yankee pool.

Ognerubov et al. [47] investigated the loss of water scenarios in spent fuel pool in Ignalina NPP using various codes (RELAP5, RELAP/SCDAPSIM, ATHLETE-CD and ASTEC) to identify the potential unrealistic parameters and assess their impact on the results while performing the calculations. They proposed few recommendations to be considered while using the system codes. First, they suggested to start the modelling process with a simplified model of a single pool and then to extend the model to include more zones. Second, errors due to the modelling assumptions must be taken into account to ensure reliable results. Finally, due to the lack of the experimental data for the consequences of a severe accident, it is recommended to use different codes to increase the confidence of the results.

Groudev et al. [48] used RELAP5/MOD3.2 code to predict the timeline of the pond dry out, heat up of the fuel rods and recovery actions from operators when transferring the fuel from Kozloduy NPP reactor vessel to the cooling pool. They observed that under leakage from the primary side, the pool could dry out after ten hours. Moreover, the

temperature of the fuel cladding exceeded 1473 K and can be prevented from reaching this level by maintaining the fuel assemblies covered by few centimetres of water.

Few papers have reported an investigation of accident mitigation options using the system codes. For example, Wu et al. [49] analysed the behaviour of CPR1000 pool under accident scenario using MAAP5 code. Moreover, they assessed the effectiveness of two mitigation measures: recovering the cooling system and make-up water. They concluded that if the fuel assemblies had uncovered the fuel cladding would be oxidised and the peak pressure in the building could reach 0.191 MPa due to the hydrogen combustion. Eventually, the fuel rods would melt down, and after ten days, the concrete floor would experience an erosion with a depth of roughly 0.95 m. To prevent such consequences, they showed that the fuel rods should be kept submerged under the water and the make-up rate should be higher than the evaporation rate. Another analysis was conducted by Wang et al. [50] for CPR1000 spent fuel using RELAP5 to evaluate the increase of the cooling water temperature in the case of failure of the cooling system. They revealed that the pool would boil off in less than 10 hr since losing the cooling.

Fu et al. [51] proposed a design of a long-term passive cooling system of the spent fuel pool at CAP1400 NPP. The two-phase heat pipe technology was implemented to provide the passive cooling. A two-phase thermosyphon loop was investigated numerically using RELAP5 code where the effect of the fill charge ratio was scrutinised. Ammonia is used as the working fluid in the heat pipe loop. They observed that the optimal ratio should fall within the range of 30% to 80%. After that, the thermosyphon loop was introduced into the fuel pool, and the cooling performance was examined using the CFD software ANSYS Fluent. It was evidenced that the implementation of the thermosyphon loop is capable of keeping the maximum water temperature below 81 °C with relatively uniform distribution.

Kaliatka et al. [52] carried out an analysis of the processes in spent fuel storage at Ignalina NPP during the loss of the cooling water due to leakage. Various severe accidents codes (ATHLET-CD, ASTEC, and RELAP/SCDAPSIM) were used to predict the potential risk of fuel overheating due to leakage of the cooling water and to compare between the capabilities of these codes. Also, the accident mitigation measure is discussed in the context of late injection of the make-up water. Good agreement was observed between

the results of the above-mentioned codes regarding the fuel temperature. However, disagreement was detected in the results of the hydrogen mass generation. In a previous study from the same authors [53], analysis of the pool performance during the loss of heat removal was conducted. The degradation of the of the fuel assemblies due to long term loss of cooling was studied using the same codes. They showed that the pool requires approximately 110 hr to heat up from 50 °C to 100 °C and around 600 hr to increase the temperature of the fuel cladding to exceed 1000 °C.

Kuo et al. [10] performed a transient analysis under the loss of cooling conditions employing RELAP5 code. Systematic evaluations of the increase of the water temperature and drop in water level were conducted for Daya Bay pool. Also, the effect of integrating a passive cooling, heat exchanger loops, was examined. It was shown that such heat exchangers would delay the consequences of the boiling process.

Wang et al. [54] used the CFD approach along with TRACE best estimate code to model the spent fuel pool of Chinshan NPP. A three-dimension CFD model was generated simplifying the fuel bundles to porous media. The results revealed a good agreement between the CFD and TRACE models. Moreover, the fuel rods start to uncover after 2.7 days. Grgic et al. [55] investigated the impact of rearranging the fuel assemblies on the thermal-hydraulic performance of NPP Krško spent fuel pool. GOTHIC computer code was used to perform the calculations for the steady state condition as well as during the loss of cooling situations.

The cited literature shows that the CFD approach is more convenient for improving the design of the cooling ponds, as it offers an in-depth understanding of the heat transfer and fluid mixing. On the other hand, the best-estimate thermal-hydraulic codes such as TRACE are more suitable for analysing the safety issues of such ponds. In general, most of the reported studies focused on investigations of the severe accident scenarios. In contrast, none of the studies has investigated the thermal performance of the cooling ponds during the normal operating conditions to understand the effect of each of the cooling systems. Furthermore, all of the spent fuel cooling ponds that have been considered have relatively small size. However, due to the continued increase in the spent fuel production, some countries tend to construct centralised ponds to keep up with the incoming spent fuel until a more permanent solution is found.

Table 2.1: Summary of the key literature on the spent fuel ponds.

No.	Author	Code used	Type of analysis	Size (m) length x width x depth	Heat load	Location
1	Hung et al. [35], (2013)	Fluent CFD [17]	Evaluation of cooling capability and local boiling	11 x 7.5 x 11	3000 MW	At-reactor, Kuoshen NPP, Taiwan
2	Ye et al. [36], (2013)	Fluent CFD [17]	Accident mitigation, new design was proposed using heat pipe	12.7 x 6.4 x 13.08	16 MW	At reactor, CAP1400 PWR, Chania
3	Yanagi et al. [38], (2012)	Fluent CFD [17]	Determination of water temperature	15 x 10 x 12	5 MW	At reactor, Fukushima Daiichi NPP, Japan
4	Yanagi et al. [39], (2012)	Fluent CFD [17]	Loss of cooling analysis after the shutdown	15 x 10 x 12	5 MW	At reactor, Fukushima Daiichi NPP, Japan
5	Chen et al. [40], (2014)	STAR-CCM+ [56]	Study of flow characteristics within fuel assemblies under loss of cooling scenario	0.2 x 0.2 x 8	2.06 kW/m <sup>2</sup>	At-reactor, Maanshan NPP, Taiwan
6	Ahn et al. [42], (2016)	MELCOR [43]	Severe accident scenario: loss of cooling and coolant	12.2 x 4.57 x 8.53	9.8 MW	At reactor, OPR1000, Republic of Korea

No.	Author	Code used	Type of analysis	Size (m) length x width x depth	Heat load	Location
7	Chen et al. [44], (2016)	GOTHIC [57]	Loss of coolant due to leakage and mitigation measures using water spray	10.78 x 10.2 x 12.88	0.274 MW	At reactor, Mark III containment, Taiwan
8	Carlos et al. [45], (2014)	TRACE [58]	Loss of cooling and coolant scenario and licensing case	12.6 x 11.3 x 11.1	3.3 and 6.4 MW	At reactor, Maine Yankee NPP, USA
9	Ognerubov et al. [47], (2014)	RELAP5, RELAP/SCDAPSIM [59], ATHLET-CD [60] and ASTEC	Accident scenario: loss of heat removal after boiling	20 x 15 x 16.9	4.25 MW	At reactor, Ignalina NPP, Lithuania
10	Groudev et al. [48], (2013)	RELAP5/MOD3.2 [61]	Accident scenario: loss of cooling	347 m <sup>3</sup>	2.376 MW	At reactor, Kozloduy NPP, Bulgaria
11	Wu et al. [49], (2014)	MAAP5 [62]	loss of cooling scenario and mitigation measures	12.5 x 12.6 x 8.5	8.87 MW	At reactor, CPR1000, Taiwan
12	Wang et al. [50], (2013)	RELAP5 [63]	Accident scenario: loss of cooling scenario	12.5 x 12.6 x 8.5	8.87 MW	At reactor, CPR1000, Taiwan
13	Fu et al. [51], (2015)	RELAP5 [63] and Fluent CFD [17]	Accident mitigation using heat pipe technology	14.7 x 8.4 x 13.08	16 MW	At reactor, CAP1400 NPP, China

No.	Author	Code used	Type of analysis	Size (m) length x width x depth	Heat load	Location
14	Kaliatka et al. [52], (2013)	ATHLET-CD [60], ASTEC [64] and RELAP/SCDAPSIM [59]	Loss of coolant scenario, due to water leakage	20 x 15 x 16.9	4.25 MW	At reactor, Ignalina NPP, Lithuania
15	Kaliatka et al. [53], (2010)	RELAP5 [63], ATHLET-CD [60] and ASTEC [64]	Accident scenario: loss of heat removal and water	20 x 15 x 16.9	4.25 MW	At reactor, Ignalina NPP, Lithuania
16	Kuo et al. [10], (2011)	RELAP5 [63]	Accident scenario and mitigation measures using heat exchanger loops	12.6 x 8 x 12.5	3.77 MW	At reactor, Daya Bay NPP, Chania
17	Wang et al. [54], (2012)	TRACE [58] and Fluent CFD [17]	Loss of cooling scenario	12.17 x 7.87 x 11.61	—	At reactor, Chinshan NPP, Taiwan
18	Grgic et al. [55], (2000)	GOTHIC [65]	Rerack the fuel assemblies to increase pond capacity	16.53 x 7.92 x 11.5	6.52 MW	At reactor, Krsko NPP, Croatia



### 2.3 Evaporation from free water surface

Numerical modelling of evaporation from a large exposed surface has gained an increased interest owing to its relevance in many engineering and environmental applications. In the context of SNF ponds, the heat loss from the water surface is the major heat transfer component comparing to the other modes and hence requiring special attention for this research [66]. Another reason is that we have attempted to formulate a method by which the energy transfer component of the evaporated water based on a published literature.

Water loss into the ambient air due to evaporation can occur without the water reaching its boiling point. Under atmospheric conditions, water can evaporate when its temperature is equal to the ambient temperature, which may be well below the boiling temperature. Evaporation is the net mass loss from water surface as a result of phase change from a liquid to a vapour. According to the kinetic theory of evaporation, water vapour is in constant motion, moving back and forth from the free water surface. Evaporation takes place when the leaving molecules exceed those entering. This process is associated with a significant amount of energy that is required to break the hydrogen bonds between the molecules of water allowing particles to escape from the water surface. There are three drivers for the evaporation process and are listed below [67]:

- The supplied heat energy that increases the kinetic energy of the water molecules.
- Diffusion of water vapour from the free water surface into the surrounding humid air.
- Transport of water vapour within the layers of the atmosphere away from the water surface.

Diffusion occurs when the fluid phase changes from liquid to gaseous phase, which takes place at a very thin boundary layer just above the free water surface [68]. This thin boundary layer can be considered as air fully saturated with water vapour. As a result of the difference between the vapour densities of the air within the boundary layer and the surrounding air, the moisture transports from the regions of high concentrations to the lower concentrations in the form of vapour [69] following Fick's law. Figure 2.1 represents a description of the transport process within a water tank as well as the

evaporation mechanism. In general, evaporation rate can be affected by four main factors: the geometry of the exposed surface, water and air temperature, the movement of air above the water surface and the relative humidity of the ambient air [70, 71].

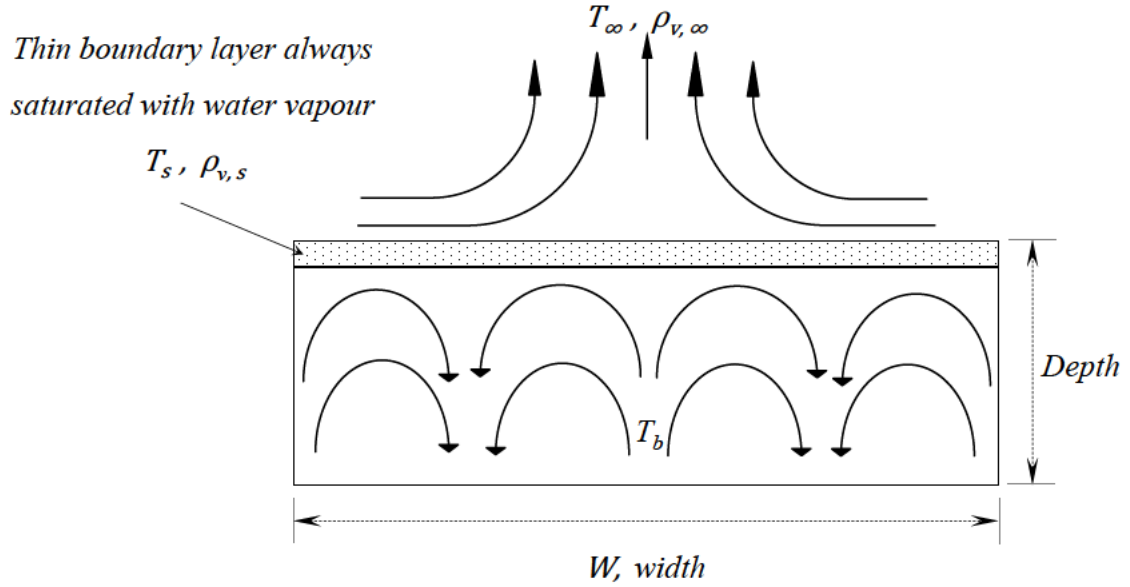


Figure 2.1: Description of the transport processes within a water tank and evaporation from the free water surface.

The study of evaporation can be classified into two broad categories according to the conditions of the volume of air above the water surface, whether still or in motion [72, 73]. If the air velocity is very low or zero, the evaporation occurs due to concentration gradient only. A large number of studies have been conducted on evaporation by taking into account the air velocity and the vapour pressures at the surface and the ambient air [74-81]. Many of these studies were conducted on evaporation from swimming pools where the water temperature is lower than the air temperature, which is required in such places. These studies yield to empirical equations that follow a generalised form as shown below:

$$\dot{m}'' = c(e_s - e_\infty) \quad (2.1)$$

where  $\dot{m}''$  is the water evaporation rate,  $c$  is a coefficient that is dependent on wind velocity, barometric pressure, and other variables,  $e_s$  is the vapour pressures within the film of air just above the water surface, and  $e_\infty$  is the vapour pressure in the ambient air.

However, the equations of the form given by Eq. (2.1) do not accurately predict the evaporation rate when the air velocity is very low or zero. Also, the empirical equations that do not consider the relative humidity of the surrounding air estimate the evaporation rate incorrectly [66].

Another approach which has been adopted by a relatively limited number of researchers is to use the Sherwood-Rayleigh power law,  $Sh \sim Ra^n$ , for predicting the evaporation rate for purely natural convection scenario [82-89]. However, some of these studies were not conducted for evaporation of water and others yield to power law exponents,  $n$ , almost the same as the turbulence heat transfer relation for heated horizontal flat plate facing upward. The parameters of  $Sh - Ra$  power law which were cited in the literature are summarised in Table 2.2. Two definitions of Rayleigh number were used in these studies as shown below:

$$Ra = Gr.Pr \quad (2.2)$$

$$Ra = Gr.Sc \quad (2.3)$$

where  $Gr$  is the Grashof number and can be defined as:

$$Gr = \frac{g\Delta\rho L^3}{\rho_{av}\nu^2} \quad (2.4)$$

here  $g$  is the gravitational acceleration,  $L$  is the characteristic length,  $\nu$  is the kinematic viscosity, and:

$$\Delta\rho = \rho_\infty - \rho_s \quad (2.5)$$

where  $\rho_\infty$  and  $\rho_s$  are the densities of the humid air at ambient and surface temperatures, respectively,  $\rho_{av}$  is the average density of the ambient and surface air, and  $Pr$  is the Prandtl number and can be defined as:

$$Pr = \frac{\nu}{\alpha} \quad (2.6)$$

where  $\alpha$  is the thermal diffusivity, and  $Sc$  is the Schmidt number which is expressed as:

$$Sc = \frac{\nu}{D} \quad (2.7)$$

where  $D$  is the mass diffusivity of water vapour in the air and can be evaluated by the following expression:

$$D = D_{298} \left( \frac{T}{298} \right)^{1.5} \quad (2.8)$$

The definition of  $Ra$  which includes the Schmidt number is more suitable for comparing the evaporation of different fluids as it takes into account the diffusivity behaviour of the fluid under consideration.

Jadat et al. [90] have studied the ability of similarity theory to predict the evaporation rate. In their study, they considered both regimes; natural and forced convection. They concluded that for the natural convection scenario, the similarity theory is capable of predicting the evaporation rate with an acceptable level of accuracy. On the other hand, the similarity theory underestimated the evaporation rate for the forced convection scenario.

Sharpley and Boelter [85] and Boelter et al. [84] conducted experimental work on evaporation using the same experimental facilities to study water evaporation from a one-foot diameter pan into the quiescent air, where the water temperature was higher than the air temperature. The outcome of Sharpley and Boelter [85] and Boelter et al. [84] studies were concluded in  $Sh - Ra$  relationship as follows:

$$[85] \quad Sh = 0.891 Ra^{0.213} \quad (2.9)$$

$$[84] \quad Sh = 0.054 Ra^{0.241} \quad (2.10)$$

where  $Sh$  is defined as:

$$Sh = \frac{h_e L}{D} \quad (2.11)$$

and  $h_e$  is the mass transfer coefficient.

Sparrow et al. [83] reported an experimental study on naturally driven evaporation from pans having diameters ranging between 8.89 and 30.68 cm. The test facility having a volume of 70 m<sup>3</sup> and was coated with cork. During the experiment, two scenarios were considered for the water temperature, “higher than” and “less than” the air temperature, which would affect the direction of the buoyancy-driven flow of air. The work of Sparrow et al. [83] yield to a relation as shown below:

$$Sh = 0.645 Ra^{0.205} \quad (2.12)$$

Bower et al. [82, 88, 89] conducted an experimental work on natural convection-driven evaporation to estimate the evaporation rate as well as the effect of various surfactant monolayers on the evaporation. These data were collected over a large number of runs using a series of water tanks having a square footprint having widths ranging from 15.2 cm to 60.9 cm and depths ranging from 5.1 cm to 35.5 cm. A schematic of the water tank is shown in Figure 2.1. The water surface temperature was measured using an infrared camera. The mass loss due to evaporation was evaluated by connecting the tank to a small beaker via a flexible syphon tube. The beaker was placed on a balance. When the water evaporates from the tank, flow of water runs through the syphon tube from the beaker to the tank to compensate the water loss as a result of evaporation. For the clean surface condition Bower et al. [89] found:

$$Sh = 0.144 Ra^{0.336} \quad (2.13)$$

It can be seen from the literature that most of the studies that adopted the  $Sh - Ra$  power law had led to correlations with exponents and coefficients almost similar to those for turbulence heat transfer from heated horizontal flat plate facing upward. In the cooling ponds, the motion of the air above the water surface is very low, and the water temperature is higher than the ambient air temperature. Therefore, the  $Sh - Ra$  relationship can be used in the current study to predict the evaporation rate in the cooling ponds.

Table 2.2: Comparison between previous studies for  $Sh - Ra$  power law parameters.

	$Sh = B.Ra^n$							
	$B$	$n$	$Sc$	$Ra$ range	$Ra$ definition	Geometry	Fluid	$L$
Bower et al. [82]	0.144	0.336	0.57	$10^6 < Ra < 6 \times 10^8$	$Gr.Pr$	Square	water in air	$W$
Sharpley and Boelter [85]	0.891	0.213	0.57	$1 \times 10^6 < Ra < 4.5 \times 10^7$	$Gr.Pr$	Circule	water in air	$d$
Boelter et al. [84]	0.054	0.241	0.57	$9.2 \times 10^6 < Ra < 4.6 \times 10^8$	$Gr.Pr$	Circule	water in air	$d$
Sparrow et al. [83]	0.645	0.205	0.57	$-6 \times 10^5 < Ra < -2 \times 10^4$	$Gr.Sc$	Circule	water in air	$d$
Goldstein et al. [87]	0.590	0.250	2.5	$2 \times 10^2 < Ra < 5 \times 10^3$	$Gr.Sc$	Various Shapes	naphthalene in air	$A/Per$
Lloyd and Moran [86]	0.169	0.327	2200	$8 \times 10^6 < Ra < 1.6 \times 10^9$	$Gr.Sc$	Various Shapes	$Cu^{2+}$ in acid	$A/Per$
Lloyd and Moran [86]	0.490	0.255	2200	$2 \times 10^4 < Ra < 8 \times 10^6$	$Gr.Sc$	Various Shapes	$Cu^{2+}$ in acid	$A/Per$

## 2.4 Studies on natural convection flow around vertical cylinders

In recent years, natural convection heat transfer around vertical cylinders has gained increased attention owing to its critical applications, especially, in the nuclear applications starting from the reactor core to the nuclear waste management. For the purpose of this research, we have focused on the waste management applications where the SNF needs to be submerged under water in cooling ponds for several years until they become less radioactive. The fuel is usually placed in a bundle of circular rods, almost the same as in the reactor core but the arrangements may differ. The heat released from the fuel assemblies is mainly transferred to the cooling water via natural convection heat transfer. Due to the inherent similarity, available literature on natural convection flow around vertical cylinders is reviewed.

Heat transfer by natural convection from a vertical cylinder can significantly differ from flat plate due to the effect of the transversal curvature in the cylinder. The effect of this curvature becomes more pronounced when the thickness of the thermal boundary layer ( $\delta_T$ ) is thicker than the diameter of the cylinder ( $d$ ). When the boundary layer thickness is much smaller than the cylinder diameters, the cylinder can be so-called “short” cylinder and the correlation for flat plate can be applied. On the other hand, when  $\delta_T$  is thicker than the diameter, we have so-called “thin” or “long” cylinder. According to Cebeci [91], the difference between the heat transfer coefficients for a laminar flow on a thin vertical cylinder and a vertical flat plate can exceed 5.5%. The development of the boundary layer over the lateral surface of the vertical cylinder is shown in Figure 2.2. For Prandtl number ( $Pr$ ) larger than one, the criterion of short cylinder limit is:

$$\frac{d}{H} > Ra_H^{-1/4} \quad (2.14)$$

where  $H$  is the cylinder height and  $Ra_H$  is the Rayleigh number based on the cylinder height,  $H$ . For isothermal surface condition, the Rayleigh number is defined as:



$$Ra_H = \frac{g\beta\Delta TH^3}{\alpha\nu} \quad (2.15)$$

When a uniform heat flux ( $q$ ) is applied at the lateral surface, the modified Rayleigh number is usually used to describe the natural convection heat transfer, which expressed as:

$$Ra_H^* = \frac{g\beta q H^4}{k\alpha\nu} \quad (2.16)$$

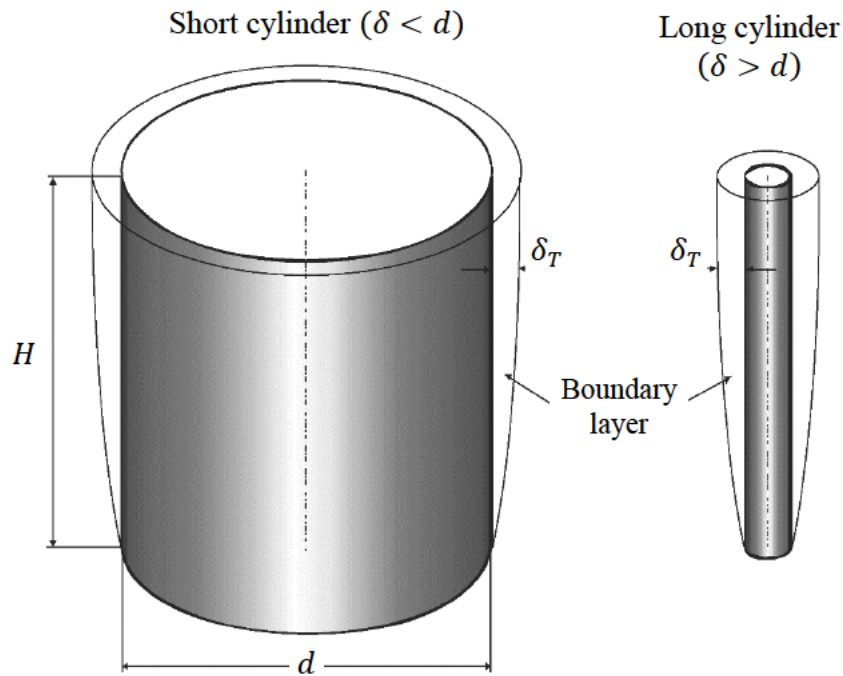


Figure 2.2: Natural convection boundary layer on the lateral surface of the vertical cylinder [92].

For free convection along vertical surfaces, the laminar boundary layer develops until it reaches a critical thickness and turns out to be unstable. This instability increases and large-scale vortices start to develop which collide and merge forming a turbulent flow. Hence, a transition region exists between the laminar and turbulent regions within the boundary layer. The location of this region can considerably differ in different experimental setups. However, it can be determined by estimating the critical similarity numbers (Grashof or Rayleigh numbers) via the plot of Nusselt number against Grashof

or Rayleigh numbers. Also, the onset of the transition can be determined experimentally by capturing the hydrodynamic or thermal boundary layers using visualisation techniques such as optic sensor and thermoanemometry technique. At the transition onset, the velocity field is disturbed causing an enhancement of the convective heat transfer coefficient somewhere downstream and becomes more evident for fluids having  $Pr > 1$ . However, considerable effort have been made by researchers to define the transition region more precisely using more sophisticated approaches and can be found in several references [93-97]. Using less precise but simpler similarity numbers, a critical Rayleigh number,  $Ra_{cr}$ , for flat plate of  $10^9$  was recommended by many authors [98, 99].

Experimental data for free convection heat transfer around vertical thin cylinder are widespread which can be due to several factors. For example, different experimental conditions and inaccuracy, which could be due to the location of the temperature sensors and heat loss via conduction to the cylinder support.

Natural convection from vertical cylinders was studied by a considerable number of researchers using experimental and theoretical approaches. A summary of these studies is shown in Table 2.3. Fujii et al. [100] experimentally investigated natural convection heat transfer from vertical cylinder submerged in water and oils. The ratio of height to diameter of the cylinder was  $H/d = 12.2$  where isothermal and uniform heat flux surface conditions were used during the experiments. They observed that the onset of transition occurs from the location where the vortex layer and instability appears. After that, the transition zone develops and finally becomes fully turbulent where the convective heat transfer coefficient rapidly increases due to the intensive mixing at the surface. However, they were unable to define the location of the transition region and the results were limited to qualitative determination only. The same findings were confirmed later by the investigation conducted Buchlin and Peelman [101] for higher ratio of  $H/d$  where uniform heat flux conditions was used. They also did not define the location of the transition onset.

Al-Arabi and Khamis [102] published experimental data for the transition boundary layer on a vertical cylinder placed in air with  $Pr = 0.71$ . They proposed correlations to describe the Nusselt number in the laminar and turbulent regions. In contrast with the previous

work, they were able to provide a criterion for the transition onset via critical Rayleigh number ( $Ra_{cr} = 2.7 \times 10^9$ ).

An interesting study on the heat transfer transition was conducted by Kimura et al. [103]. They experimentally investigated the heat transfer around a heated vertical cylinder submerged in a water tank. The cylinder with a height of 1.2 m was heated with uniform heat flux. The unique aspect of their work was that they studied the effect of the cylinder diameter on the heat transfer characteristics where the diameter varied from 10 to 165 mm corresponds to  $H/d$  ranging from 7.27 to 120. Flow visualisation technique was used to determine the transition onset, which it was assumed to begin with flow separation. The study showed that reducing the diameter results in delaying the onset of transition and the heat transfer coefficient was considerably enhanced. Also, the critical Rayleigh number for  $H/d < 60$  almost agrees with that for flat plate [104]. For  $H/d > 60$ , on the other hand, similar distribution was observed but the critical Rayleigh number was higher. Moreover, the experiment revealed that the modified critical Rayleigh number is not sensitive to the value of the heat flux ( $q$ ).

Arshad et al. [105] reported an experimental work of high Rayleigh number natural convection heat transfer from a single vertical cylinder having a diameter of 12.7 mm and  $H/d \approx 48$ . The cylinder was submerged in a large water tank where it was heated with a constant heat flux. Their results agreed with the data reported by Nagendra et al. [106] for the laminar region. Correlations based on the modified Rayleigh number were developed and compared with the experimental data for Fujii et al. [100] and were found to be in good agreement. The results showed that the temperature distribution on the cylinders surfaces is gradually increased in the axial direction along the laminar boundary layer. When the transition section began, the temperature starts to decrease enhancing the convective heat transfer coefficient. These observations also agree with the finding of Kimura et al. [103]. Arshad et al. [105] extended their work to investigate the heat transfer for a 3 x 3 array of thin vertical cylinders. They proposed empirical correlations for an assembly of cylinders in terms of Nusselt and Rayleigh numbers.

Kang et al. [107] experimentally investigated the curvature effect on the free convection from thick and thin vertical cylinder. The unique aspect of their work was that they studied the effect of the high Prandtl number fluids,  $Pr$  ranging from 2094 to 5878, on

the heat transfer characteristics. They showed that, in the laminar region, heat transfer from vertical cylinder and flat plate exhibit almost the same nature and the Nusselt number is a very weak function of Prandtl number. However, when the flow became turbulent, the dependency of Prandtl number start to appear where the Nusselt number decreased with increase of the Prandtl number. Also, they proposed correlations for thick cylinder for both laminar and turbulent flow.

The literature showed that the natural convection heat transfer from vertical cylinder has been extensively studied, experimentally and mathematically, for several decades. In the last few years, prediction of the transition region from laminar to turbulent on the surface of thin vertical cylinder has gained more attention due to its importance in nuclear applications. However, there seems to be limited numerical work on the turbulent free convection heat transfer from vertical cylinders, in particular, on the transition region and the effect of the curvature on the heat transfer characteristics.

Table 2.3: Selected literature on natural convection from vertical cylinder.

No.	Author	$H/d$	Surface condition	Fluid and $Pr$	$Ra$ range	Correlation	Remarks
1	Fujii et al. [100]	—	$q = Mx^n$	0.72 – 100	Laminar and $\frac{2x}{d} \leq 0.7Nu_{x,FP}$	$Nu_x = Nu_{x,FP} + 0.345 \frac{2x}{d}$	Based on numerical calculations
2	Nagendra et al. [106]	95 – 3050	$q = \text{cont}$	Water	$Ra_d \frac{H}{d} < 0.05$ $0.05 < Ra_d \frac{H}{d} < 10^4$ $Ra_d \frac{H}{d} < 10^4$	$Nu_d = 0.93 \left(Ra_d \frac{H}{d}\right)^{0.05}$ $Nu_d = 1.37 \left(Ra_d \frac{H}{d}\right)^{0.16}$ $Nu_d = 0.93 \left(Ra_d \frac{H}{d}\right)^{0.25}$	Agreed with experimental data reported by the same author for water [108]
3	Al-Arabi and Khamis [102]	300-2000	Isothermal	Air $Pr = 0.71$	Lam: $9.88 \times 10^7 \leq Ra_H \leq 2.7 \times 10^9$ Turb: $2.7 \times 10^9 \leq Ra_H \leq 2.95 \times 10^{10}$	$Nu_H = 2.9Ra_H^{0.25}/Gr_d^{0.5}$ $Nu_H = 0.47Ra_H^{0.33}/Gr_d^{0.5}$	Based on experimental data. Maximum deviation $\pm 8\%$
4	Cebeci [91]	—	Isothermal	$Pr = 0.72$ $Pr = 0.76$	Laminar: $Gr_x < 4 \times 10^9$	$\frac{Nu_H}{Nu_{H,FP}} = 1 + 0.3 \left[ \sqrt{32} Gr_H^{-0.25} \frac{H}{d} \right]^{0.909}$	Based on theoretical results
5	Chen et al. [109]	—	$T_w - T_\infty = ax^n$	$Pr = 0.1$ – 100	Laminar	$\ln \left[ \frac{Nu_H Gr_H}{4} \right] = f(Gr_H, H/d, Pr, n)$	Based on boundary layer analysis

No.	Author	$H/d$	Surface condition	Fluid and $Pr$	$Ra$ range	Correlation	Remarks
6	Kimura et al. [103]	7.27 – 120	$q = \text{cont}$	Water $Pr = 5.4$	$Gr_x < 3.7 \times 10^9$	Agreed with the proposed correlations by Fujii, and Uehara [110]	Based on experimental data
7	Popiel et al. [111]	1 – 60	Isothermal	Air $Pr = 0.71$	$10^8 - 1.1 \times 10^9$	$Nu_H = A Ra_H^n$ $A = 0.519 + \frac{0.03454H}{d} + 0.0008772(H/d)^2 + 8.855 \times 10^{-6}(H/d)^3$ $n = 0.25 - 0.00253H/d + 1.152 \times 10^{-5}(H/d)^2$	Based on experimental data
8	Arshad et al. [105]	48	$q = \text{cont}$	Water $Pr = 5.5$	$4.71 \times 10^7 \leq Ra_x^* \leq 1.91 \times 10^{13}$ $3.4 \times 10^{12} \leq \bar{Ra}_H^* \leq 2.41 \times 10^{13}$	$Nu_x = 0.682 Ra_x^{*0.19}$ $Nu_H = 0.893 \bar{Ra}_H^{*0.19}$	Based on experimental data. Agreed with Fujii et al. [100]
9	Kang et al. [107]	10 – 140	—	$Pr = 2094 - 5878$	$1.4 \times 10^9 \leq Ra_H \leq 3.2 \times 10^{13}$	$Pr = 2094, Nu_H = 0.26 Ra_H^{0.28} Pr^{0.0091}$ $Pr = 2183, Nu_H = 0.26 Ra_H^{0.28} Pr^{0.0090}$ $Pr = 2497, Nu_H = 0.25 Ra_H^{0.28} Pr^{0.0084}$ $Pr = 3058, Nu_H = 0.23 Ra_H^{0.28} Pr^{0.0076}$ $Pr = 4173, Nu_H = 0.21 Ra_H^{0.28} Pr^{0.0063}$ $Pr = 5878, Nu_H = 0.20 Ra_H^{0.28} Pr^{0.0055}$	Experiment conducted using limiting current technique. Only valid for turbulent flow on thick cylinder

## 2.5 Concluding remarks

The cited literature shows that the CFD approach is convenient for improving the design of the cooling ponds, as it offers an in-depth understanding of the heat transfer and fluid mixing. On the other hand, the best-estimate thermal-hydraulic codes such as TRACE are more suitable for analysing the safety issues of such ponds.

In general, most studies focused on the investigations of severe accident scenarios and the analysis of the consequences. However, relatively few studies have reported improving the pond design as well as accident mitigation options. On the other hand, none of the studies has investigated the thermal performance of the spent fuel cooling pond during its normal operating conditions to understand the effect of each of the cooling systems, which can be the first line of defence in accident prevention.

It is worth noting that most of the spent fuel cooling ponds that have been reported in the cited studies are relatively small in sizes. However, due to the continued increase in the spent fuel production, some countries have constructed centralised ponds to keep up with the incoming spent fuel until a more permanent solution is found [112, 113]. To the best of the author knowledge, centralised, large-scale ponds have not been reported before in the open literature. This may be attributable to challenges encountered during modelling and analysis of such systems or due to the commercial sensitive nature of the work as well as security reasons.

This raises the significance of investigating such large-scale ponds and analysing their behaviour to provide more understanding of their thermal performance. This will allow for better operation and offers mitigation options in accident scenarios. In order to achieve that, two fundamental phenomena related to the modelling of the pond were discussed in the literature.

First is the evaporation from the free water surface. The literature showed that most of the studies that adopted the  $Sh - Ra$  power law, had led to correlations with exponents close to  $1/3$  which is similar to the natural convection heat transfer from horizontal flat plate. For the purpose of the current study, we are interested in the situations where the surrounding air is quiescent, and the water temperature is higher than the ambient air

temperature. Therefore, the  $Sh - Ra$  relationship can be used in the current study to predict the evaporation rate in the cooling ponds.

The second phenomenon is the natural convection heat transfer around vertical cylinder. The literature showed that such a phenomenon has been extensively studied, experimentally and mathematically, for several decades. In the last few years, prediction of the transition region from laminar to turbulent on the surface of thin vertical cylinder has gained more attention due to its importance in nuclear applications. However, there seems to be limited numerical work on the turbulent free convection heat transfer from vertical cylinders, in particular, on the transition region and the effect of the curvature on the heat transfer characteristics.



## Chapter 3 Methodology of CFD Modelling and Data Analysis

### 3.1 Introduction

In this chapter, the main governing equations of the CFD approach are presented. The statistical methods of Taguchi and ANOVA, which are used to perform the sensitivity study are also discussed.

### 3.2 CFD methodology

CFD is the field that uses computers to simulate flow related problems involving many physical situations such as fluid flow, heat transfer, chemical reactions combustion etc. This field has been developing for more than 30 years and is now well-established. The general methodology can be found in most of the fluid dynamics textbooks [16, 114-117]. During the last decade, user-friendly commercial software packages have been developed thanks to the availability of more powerful computers. As a result, CFD is widely used in many industrial applications of aerodynamics, combustion, nuclear industry, and turbomachinery etc. There are several available commercial and open-source codes that adopt the CFD approach, for instance, ANSYS Fluent, STAR-CCM+, COMSOL, and OpenFOAM.

In ANSYS Fluent CFD, the finite volume approach is used to formulate the governing differential equations. The governing equations of the fluid flow represent three conservation laws of physics as follow:

- Mass conservation
- Momentum conservation
- Energy conservation

In addition to documenting fundamental equations, we have elaborated on certain topics such as eddy viscosity models, implementation of natural convection and porous medium approach in the context of ANSYS Fluent because of their relevance to the present investigation.

### 3.2.1 Continuity equation

The continuity equation is derived from applying the mass conservation principle on a control volume and can be expressed as [17]:

$$\frac{\partial \rho}{\partial t} + \nabla \cdot (\rho \vec{v}) = S_m \quad (3.1)$$

where  $\rho$  is the fluid density,  $\vec{v}$  is the velocity and  $S_m$  is the mass source term. Equation (3.1) is valid for compressible as well as incompressible flows. For incompressible flow, the first term becomes zero,  $\frac{\partial \rho}{\partial t} = 0$ .

### 3.2.2 Momentum conservation equation

The momentum equation is obtained from applying Newton's second law on an infinitesimal control volume and can be described by [17]:

$$\frac{\partial}{\partial t}(\rho \vec{v}) + \nabla \cdot (\rho \vec{v} \vec{v}) = -\nabla p + \nabla \cdot (\bar{\tau}) + \rho \vec{g} + \vec{F} \quad (3.2)$$

where  $p$  is the static pressure,  $\rho \vec{g}$  and  $\vec{F}$  are the gravitational body force and external body force respectively.  $\vec{F}$  also includes other model-dependent source terms such as user-defined and porous media sources.  $\bar{\tau}$  is the stress tensor and is expressed as:

$$\bar{\tau} = \mu \left[ (\nabla \vec{v} + \nabla \vec{v}^T) - \frac{2}{3} \nabla \cdot \vec{v} I \right] \quad (3.3)$$

where  $\mu$  is the molecular viscosity,  $I$  is the unit tensor, and the second term on the right hand side is the effect of volume dilation.

### 3.2.3 Turbulence modelling

The unsteady random motion in three-dimensional is called turbulence and observed at moderate to high Reynold number. One characteristic of the turbulent flow is velocity fluctuations, which have a blend of transport quantities of momentum, energy and species concentration creating fluctuations in the transport equations. These fluctuations are characterised by high frequencies and a wide range of length and time scale. In principle, turbulence is described via the Navier-Stokes equations. There are various types of turbulence modelling such as Eddy Viscosity Models (EVM), Large Eddy Simulation (LES) and Direct Numerical Simulation (DNS) [16]. The most economical approach for turbulence calculations in complex industrial flows is the EVM. On the other hand, DNS is the most accurate approach but it is the most expensive.

For the purpose of this study, the choices were limited to specific models of the widely used EVMs since these models have less computational demands than the other two approaches, DNS and LES [118]. One shortcoming of the EVMs is that these models are insensitive to streamline curvature and system rotation, which play an important role in several turbulent flows of practical interest. ANSYS Fluent has the capability to model the turbulence behaviour of the flow using various turbulent and some of them will be discussed later.

#### 3.2.3.1 *k- $\epsilon$ Model*

This model is generally applicable for many applications but in several situations, it provides low accuracy. Despite this disadvantage, the *k- $\epsilon$*  model still used by wide range of industries and researchers due to the low computational time, robustness, and reasonable accuracy. In the *k- $\epsilon$*  model, the turbulent length and time scale is determined by solving two separate transport equations, kinetic energy (*k*) and dissipation rate ( $\epsilon$ ). The transport equation for kinetic energy is computed from the exact equation (*k*) whereas the transport equation for its dissipation rate is attained by using physical reasoning [17]. The transport equations for the standard *k- $\epsilon$*  model can be written as:

$$\frac{\partial}{\partial t}(\rho k) + \frac{\partial}{\partial x_i}(\rho k u_i) = \frac{\partial}{\partial x_j} \left\{ \left( \mu + \frac{\mu_t}{\sigma_k} \right) \frac{\partial k}{\partial x_j} \right\} + G_k + G_b - \rho \varepsilon - Y_M + S_k \quad (3.4)$$

and

$$\frac{\partial}{\partial t}(\rho \varepsilon) + \frac{\partial}{\partial x_i}(\rho \varepsilon u_i) = \frac{\partial}{\partial x_j} \left\{ \left( \mu + \frac{\mu_t}{\sigma_\varepsilon} \right) \frac{\partial \varepsilon}{\partial x_j} \right\} + C_{1\varepsilon} \frac{\varepsilon}{k} (G_k + C_{3\varepsilon} G_b) - C_{2\varepsilon} \rho \frac{\varepsilon^2}{k} + S_\varepsilon \quad (3.5)$$

where  $G_k$  is the generation of turbulent kinetic energy due to the mean velocity gradients,  $G_b$  is the kinetic energy generation due to buoyancy,  $Y_M$  is the contribution of the fluctuating dilatation in compressible turbulence to the overall dissipation rate;  $C_{1\varepsilon}$ ,  $C_{2\varepsilon}$ , and  $C_{3\varepsilon}$  are constants; and  $\sigma_k$  and  $\sigma_\varepsilon$  are the turbulent Prandtl numbers for  $k$  and  $\varepsilon$  respectively;  $S_k$  and  $S_\varepsilon$  are user-defined source terms.

### 3.2.3.2 Standard and SST $k$ - $\omega$ models

In ANSYS Fluent, the standard  $k$ - $\omega$  is based on the  $k$ - $\omega$  model for Wilcox [119] that which integrates modifications for compressibility, low-Reynolds number effects, and shear flow spreading. One of the weak points of the Wilcox model is the sensitivity of the solutions to values for kinetic energy ( $k$ ) and specific dissipation rate ( $\omega$ ) outside the shear layer. This model is an empirical model based on model transport equations for the turbulence  $k$  and  $\omega$ . The transport equations for the standard  $k$ - $\omega$  model are expressed as:

$$\frac{\partial}{\partial t}(\rho k) + \frac{\partial}{\partial x_i}(\rho k u_i) = \frac{\partial}{\partial x_j} \left\{ \Gamma_k \frac{\partial k}{\partial x_j} \right\} + G_k - Y_k + S_k \quad (3.6)$$

and

$$\frac{\partial}{\partial t}(\rho \omega) + \frac{\partial}{\partial x_i}(\rho \omega u_i) = \frac{\partial}{\partial x_j} \left\{ \Gamma_\omega \frac{\partial \omega}{\partial x_j} \right\} + G_\omega - Y_\omega + S_\omega \quad (3.7)$$

Menter [120] developed the Sear-Stress Transport (SST)  $k$ - $\omega$  model by successfully combining the accurate and robust formulation of the  $k$ - $\omega$  model in the near-wall regions with the freestream independence of the  $k$ - $\varepsilon$  model in the regions far from the wall.

### 3.2.3.3 Low-Reynolds-number $k$ - $\epsilon$ models

The flow near the boundary in natural convection heat transfer plays a vital role in establishing the temperature field in the computational domain [121]. Sufficient number of cells near to the heat transfer surface is required to resolve the boundary layer, except when the wall function is used. When the surface is approached, viscous effects become more significant where for  $y^+ < 5$  the viscous diffusion is greatly higher than the turbulent diffusion. In this case, the high Reynolds number ( $Re$ )  $k$ - $\epsilon$  turbulence model can deliver low accuracy. On the other hand, the low- $Re$   $k$ - $\epsilon$  models, which are variations of high- $Re$   $k$ - $\epsilon$ , can be used as it integrates the transport equations all the way down the wall.

### 3.2.3.4 Transition-SST model

In the transition SST model, the transport equations of the intermittency and the transition onset criteria in terms of momentum-thickness Reynolds number are coupled with SST  $k$ - $\omega$  transport equations. This model has the capability to capture the transition onset locations. The mesh requirement of the transition model is related to the dimensionless wall normal distance  $y^+$  value as the accuracy of this turbulence model to predict the transition onset is highly sensitive to  $y^+$  value. A test case was conducted on flat plate illustrated in Figure 3.1. It shows that by increasing  $y^+$  above 8, the location of transition onset starts to shift to upstream. When the value increases to 25, the majority of the boundary layer is turbulent. In contrast, when  $y^+$  has values below 0.001 the location of transition seems to move downstream [17].

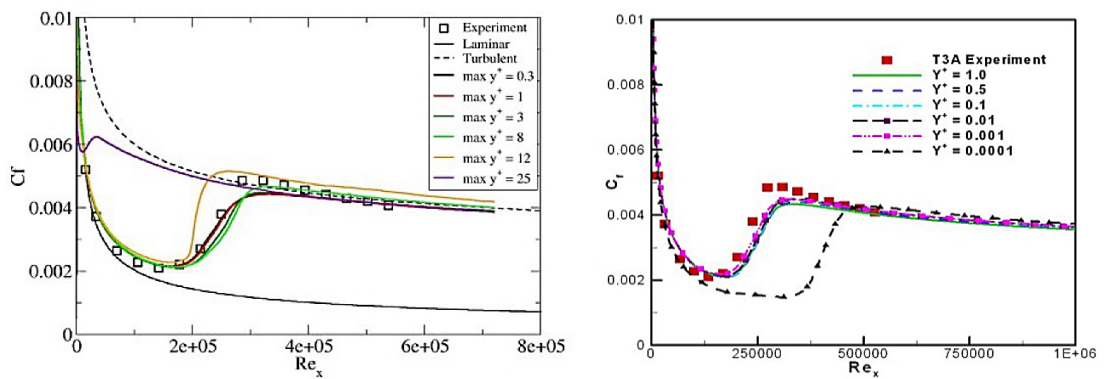


Figure 3.1. Effect of  $y^+$  value on transition onset [17].

### 3.2.4 Energy conservation equation

The first law of thermodynamics can be applied on a control volume to derive the energy equation. In Fluent, the energy conservation equation is expressed as [17]:

$$\frac{\partial}{\partial t}(\rho E) + \nabla \cdot (\vec{u}(\rho E + p)) = -\nabla \cdot \left[ k_{eff} \nabla T - \sum_j h_j \vec{J}_j + (\vec{\tau}_{eff} \cdot \vec{u}) \right] + S_h \quad (3.8)$$

where  $k_{eff}$  is the effective thermal conductivity that contains turbulent thermal conductivity defined by the selected turbulence model,  $\vec{J}_j$  is the species  $j$  diffusion flux and  $S_h$  includes the heat of chemical reaction, and any other user-defined volumetric heat sources. In Eq. (3.8),  $E$  is defined as:

$$E = h - \frac{p}{\rho} - \frac{u^2}{2} \quad (3.9)$$

where sensible enthalpy is defined for ideal gases as:

$$h = \sum_j Y_j h_j \quad (3.10)$$

and for incompressible flow as:

$$h_j = \int_{T_{ref}}^T C_{p,j} dT \quad (3.11)$$

where  $T_{ref}$  is reference temperature and is equal to 298.15 K in the pressure-based solver.

### 3.2.5 Natural convection

In ANSYS Fluent, there are two methods to model natural convection. The first approach is the precise model where the fluid density is defined as a function of temperature. The second approach is the use of Boussinesq model where density is treated as a constant value in all of the equations, except for the buoyancy term in the momentum equation [17]:

$$(\rho - \rho_o)g \approx -\rho_o\beta(T - T_o)g \quad (3.12)$$

where  $\rho_o$  is the flow density which is constant,  $\beta$  is the thermal expansion coefficient and  $T_o$  is the operating temperature. Boussinesq approximation ( $\rho = \rho_o(1 - \beta T_o)$ ) is used to eliminate  $\rho$  from the buoyancy term. The Boussinesq approximation is only valid for small temperature and density variations.

### 3.2.6 Modelling porous media

The porous media is included in the standard momentum equation through additional source term that appears in the  $\vec{F}$  term. This source term consists of two quantities. The first quantity is the viscous loss term, Darcy, which is represented in Eq. (3.13) by the first term on the right-hand side. The second quantity is the inertia loss term that is described in Eq.(3.13) by the second term on the right-hand side:

$$S_i = - \left[ \sum_{j=1}^3 \mathcal{D}_{ij} \mu v_i + \sum_{j=1}^3 \mathcal{C}_{ij} \frac{1}{2} \rho |v| v_i \right] \quad (3.13)$$

where  $S_i$  is the porous media source term that appears in the  $\vec{F}$  term in the momentum equation,  $v_i$  is the velocity in the  $i$ th directions ( $x, y$  or  $z$ ),  $|v|$  is the velocity magnitude, and  $\mathcal{D}$  and  $\mathcal{C}$  are prescribed matrices. In the porous zone, the momentum sink contributes to the pressure gradient resulting in pressure drop that is proportional to the fluid velocity. However, for homogeneous media the source term can be written as:

$$S_i = -\left(\frac{\mu}{\Omega} v_i + C_2 \frac{1}{2} \rho |v| v_i\right) \quad (3.14)$$

where  $\Omega$  is the permeability and  $C_2$  is the inertial resistance factor.

When the flow regime through the porous media is laminar, the constant  $C_2$  can be assumed to be zero. The pressure drop is calculated in each of the direction coordinates as follows:

$$\Delta p_x = \sum_{j=1}^3 \frac{\mu}{\Omega_{xj}} v_i \Delta n_x \quad (3.15)$$

$$\Delta p_y = \sum_{j=1}^3 \frac{\mu}{\Omega_{yj}} v_i \Delta n_y \quad (3.16)$$

$$\Delta p_z = \sum_{j=1}^3 \frac{\mu}{\Omega_{zj}} v_i \Delta n_z \quad (3.17)$$

where  $\Delta n_x$ ,  $\Delta n_y$ , and  $\Delta n_z$  are the thicknesses of the porous medium in the  $x$ ,  $y$ , and  $z$  directions respectively.

In terms of heat transfer through the porous media, the standard energy equation is rearranged in the porous media zone to modify the conduction flux and transient terms only.

$$\begin{aligned} & \frac{\partial}{\partial t} (\gamma \rho_f E_f + (1 - \xi) \rho_s E_s) + \nabla \cdot (V (\rho_f E_f + p)) \\ & = \nabla \cdot \left[ k_{eff} \nabla T - \left( \sum_i h_i j_i \right) + (\bar{\tau} \vec{V}) \right] + S_f^h \end{aligned} \quad (3.18)$$

where  $E_f$  is the fluid total energy;  $E_s$  is the solid region total energy,  $\xi$  is the medium porosity, and  $S_f^h$  is the enthalpy source term of the fluid.



In ANSYS Fluent, The effective thermal conductivity,  $k_{eff}$ , of the porous medium is calculated based on the volume average of the fluid and the solid conductivities:

$$k_{eff} = \xi k_f + (1 - \xi)k_s \quad (3.19)$$

where  $k_f$  is the thermal conductivity of the fluid, which includes the turbulent contribution  $k_t$ , and  $k_s$  is the thermal conductivity of the solid medium.

### 3.3 Data analysis

In this research, Taguchi design approach will be used to perform a sensitivity study. The results of this study will be further analysed using analysis of variance method (ANOVA) to examine the influence of the input parameter of the analytical model on the overall performance of the cooling pond. The Taguchi and ANOVA methods are being adopted in a wide range of engineering applications such as in manufacturing engineering and heat transfer problems. Examples for the use of Taguchi and ANOVA methods in the manufacturing engineering studies are given in the following references [122, 123], while examples in the heat transfer field can be found in the following references [124, 125].

#### 3.3.1 Taguchi method

The full factorial design of experiment would include all the possible combinations for a given group of parameters. This results in a large number of experiments to be performed, especially, in industrial applications where a significant number of factors are involved. In order to reduce the experimental run to an affordable level, a small number of the possible configurations are chosen which is known as a partial fraction experiment. However, there are no general rules for its application. Taguchi created a distinct set of general design guidelines for fractional factorial experiments that applicable for many applications [126]. Taguchi used a set of arrays called orthogonal arrays (OA) to ease the process of experimental design to study a large number of variables with the minimum number of experiments. The general steps for Taguchi method are shown in Figure 3.2. Taguchi method offers more efficient design of experiment than many other statistical

approaches. The degree of freedom approach is used in Taguchi method to determine the minimum experimental runs that are required to be conducted and can be calculated from:

$$N_{Taguchi} = 1 + \sum_{i=1}^{NV} (L_i - 1) \quad (3.20)$$

here  $NV$  is the number of independent variables and  $L_i$  is the number of levels of each of the independent variables.

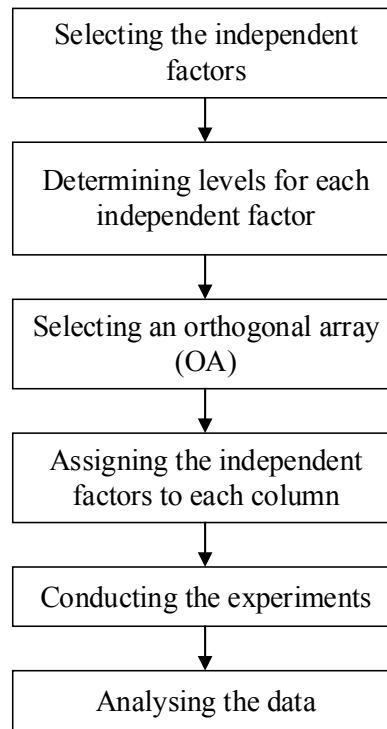


Figure 3.2: Steps for Taguchi method.

### 3.3.2 Analysis of variance (ANOVA)

Each of the experimental runs represents a combination of different levels of the independent variables. For this reason, it is necessary to separate the individual effect of these variables, which can be achieved by the widely used statistical method ANOVA.

The ANOVA is a hypothesis test to compare the means of more than two populations. The null hypothesis,  $H_0$ , is assumed which means that the difference between specified populations is insignificant and any observed difference is due to an experimental or

sampling error. F-tests are used to inspect a pre-specified set of standard effects such as main effects and interactions [127]. In another word, the statistical significance in the ANOVA is tested by comparing the F-values, which is defined as:

$$F\text{-value} = \frac{\text{variance between groups}}{\text{variance within groups}} \quad (3.21)$$

The F-value can be further used to calculate the probability value, P-value, which confirms or rejects the null hypothesis. For 95% confidence region, if the P-value is lower than 5%, the null hypothesis and the results said to be statistical significance.

### 3.3.3 Minitab software

Minitab is a complete statistical software package that was developed by researchers at the Pennsylvania State University in 1972. In this research, the Minitab software [128] will be used to perform the sensitivity study using Taguchi method as well as to analyse the obtained data by the ANOVA approach.

## Chapter 4 Heat Loss from Water Surface Undergoing Free Evaporation

### 4.1 Introduction

This chapter focuses on establishing a numerical methodology for modelling heat loss from a water surface undergoing free evaporation using single-phase flow. From a computational point of view, modelling of heat loss and evaporation from a large water body such as spent fuel cooling ponds requires a computational model involving liquid water and moist air. This can be computationally demanding and not always necessary when only the heat transfer is the main quantity.

This chapter presents an alternative to using a multiphase approach by exploring the suitability of applying an overall heat transfer coefficient on the top surface based on evaporation data and theoretical solution. In this study, the total heat flux from the free water surface was analytically evaluated considering three heat transfer mechanisms: evaporation, convection, and radiation. From the total heat flux, an expression for the overall heat transfer coefficient as a function of the water surface temperature was extracted. This expression was introduced to the CFD software via a UDF and then implemented to simulate cooling process for a water tank. The obtained results from this simulation were validated against experimental data available in literature.

### 4.2 Analytical modelling of heat and mass transfer from water surface

The total heat flux ( $q_t$ ) from the water surface to the ambient air is made up of three components, namely the evaporative heat flux ( $q_e$ ), the convective heat flux ( $q_c$ ), and the radiative heat flux ( $q_r$ ) as shown below:

$$q_t = q_e + q_c + q_r \quad (4.1)$$

Each of these components can be analytically modelled in a separate manner and then the total heat flux can be evaluated. After that, an expression for the overall heat transfer coefficient at the top surface can be obtained.

#### 4.2.1 Evaporation heat loss

To model the evaporation heat loss from the top surface, the dimensionless relationship  $Sh - Ra$  is adapted. From the definition of Rayleigh number, the characteristic length is raised to the power of 3, therefore, by employing the exponent  $n = 1/3$  in the power law relation the effect of the characteristic length will diminish generating an expression that is independent of the geometry of the surface area. Hence, this will facilitate the use of the expression during the numerical modelling process. The power law relation  $Sh - Ra$  can be written as:

$$Sh = 0.15 Ra^{1/3} \quad (4.2)$$

and the mass transfer coefficient can be calculated from the following equation:

$$h_e = 0.15 \left( \frac{g \Delta \rho L^3}{\rho_{av} \alpha v} \right)^{1/3} \left( \frac{D}{L} \right) \quad (4.3)$$

The evaporation mass flux from the free water surface ( $\dot{m}''$ ) is obtained from the following equation:

$$\dot{m}'' = h_e (\rho_{v,s} - \rho_{v,\infty}) \quad (4.4)$$

here,  $\rho_{v,s}$  is the vapour density at the surface which is at saturation conditions, and  $\rho_{v,\infty}$  is the ambient vapour density. Finally, the heat flux due to evaporation can be calculated as follows:

$$q_e = \dot{m}'' h_{fg} \quad (4.5)$$

where  $h_{fg}$  is the latent heat of vaporisation and can be evaluated from:

$$h_{fg} = 2501 - 2.361(T - 273) \quad (4.6)$$

The evaporation rate was computed at several surface temperatures and the results are compared against the experimental data for Bower et al. [89] as shown in Figure 4.1. The comparison was based on a tank having a square footprint of side length of 15.2 cm and depth of 5.1 cm where the ambient air was at  $T_\infty = 25^\circ\text{C}$  and 57% relative humidity. The deviation between the values of the calculated and experimental data is within  $\pm 30 \text{ mg/m}^2\text{s}$ .

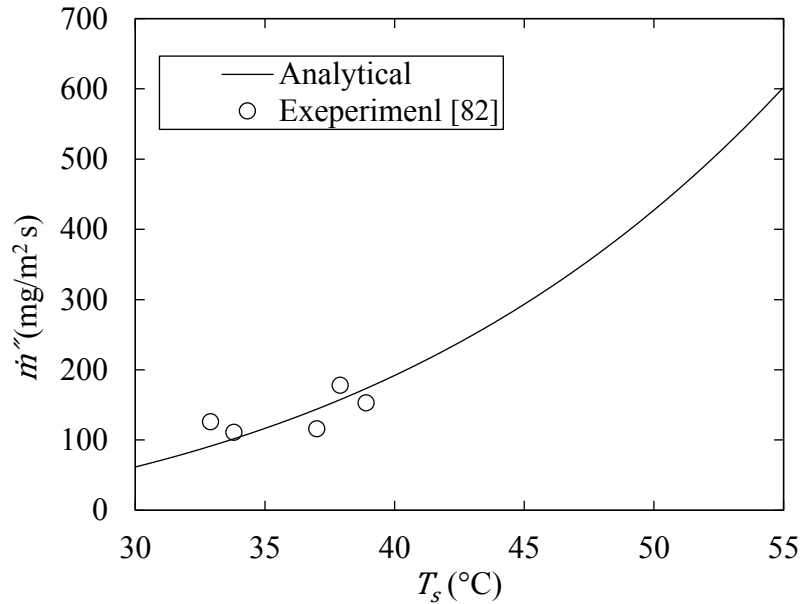


Figure 4.1: Comparison of calculated evaporation rate and experimental data for Bower et al. [82].

The evaporation rate exhibits a nonlinear behaviour with water temperature, however, over a small range of temperature the evaporation rate can be considered as a linear function of the surface temperature. When the exponent of the power law  $n$  is equal to  $1/3$ , the relation for  $h_e$  in Eq. (4.3) can be reduced to:

$$h_e \approx \left( \frac{\Delta\rho}{\rho_{av}} \right)^{1/3} \quad (4.7)$$

The quantities  $\Delta\rho/\rho_{av}$  in Eq. (4.7) and  $\Delta\rho_v$  in Eq. (4.4) are plotted against the evaporation rate,  $\dot{m}''$ , as shown in Figure 4.2. It can be seen from this figure that  $\dot{m}''$  increases almost linearly with  $\Delta\rho_v$  and the nonlinearity seen in  $\dot{m}''$  in Figure 4.2 is mostly due to the contribution of the term  $\Delta\rho/\rho_{av}$ .

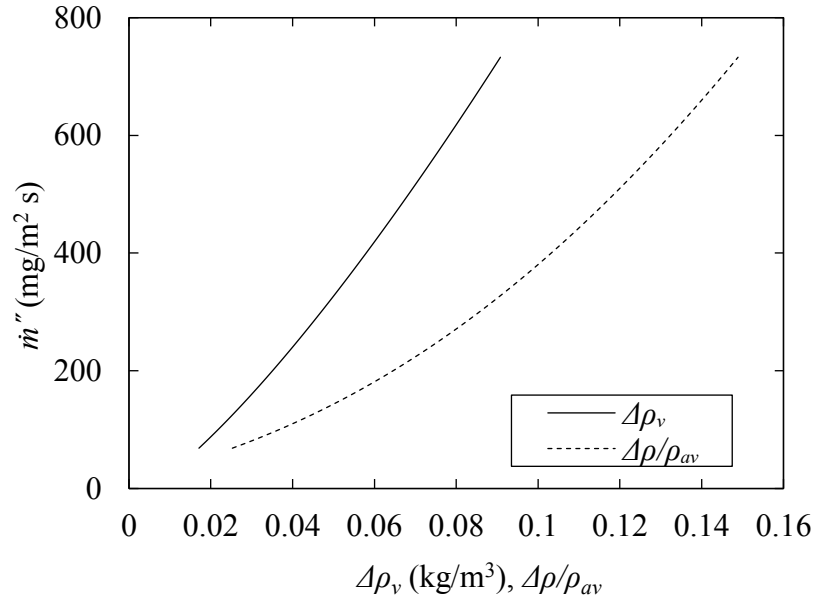


Figure 4.2: Plot of  $\dot{m}''$  versus  $\Delta\rho_v$  and  $\Delta\rho/\rho_{av}$  over range of surface temperature.

The errors seen in the prediction of evaporation rate,  $\dot{m}''$ , are due to the combination of the errors associated with measurements uncertainty and the contribution of the assumption of that the ambient air temperature and  $RH$  are remain constant throughout the calculations. The evaporation rate is a sensitive function of the surface temperature and the relative humidity as shown in Figure 4.3. Small errors in  $T_s$  readings can cause a measurable error in  $\dot{m}''$  calculations. Also, the experimental uncertainty in measuring the  $\dot{m}''$  is almost  $\pm 10\%$ . Regarding the assumptions, the transport of water vapour to the air due to evaporation can affect the humidity level in the ambient air and as mentioned before  $RH$  can considerably affect the  $\dot{m}''$  calculations.

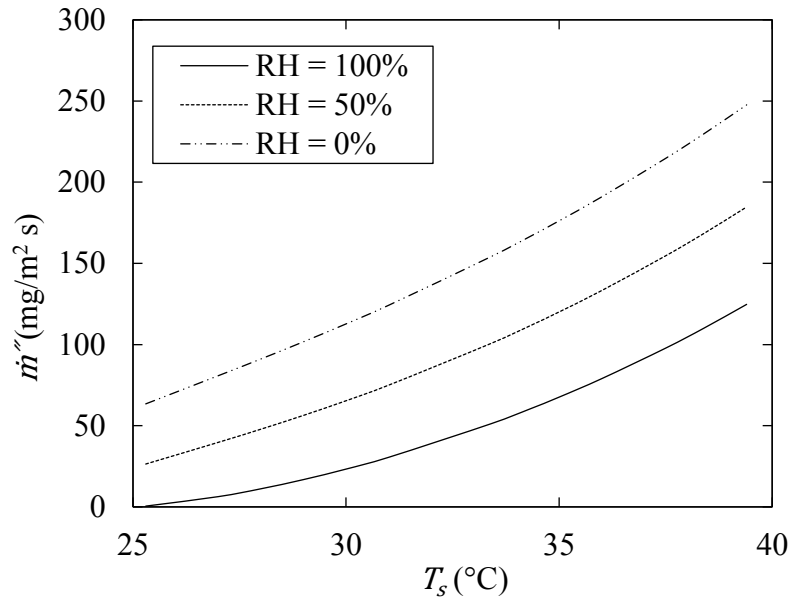


Figure 4.3: Effect of relative humidity and water surface temperature on the evaporation rate.

#### 4.2.2 Convection and radiation heat loss

The heat loss from the water top surface by means of natural convection and radiation may be less significant than that by evaporation. However, it cannot be ignored as the water bulk and surface temperatures are very sensitive to the boundary condition at the top surface. The heat loss by convection from the free water surface to the atmosphere can be treated as a heated horizontal plate facing upward and the correlation in Eq. (4.8) can be used to evaluate the convective heat transfer as follow:

$$Nu = 0.15 Ra^{1/3} \quad (4.8)$$

where  $Nu$  is the Nusselt number, defined as:

$$Nu = \frac{h_c L}{k} \quad (4.9)$$

where  $h_c$  is the convective heat transfer coefficient. The convective heat flux can be calculated from the following equation:



$$q_c = h_c(T_s - T_\infty) \quad (4.10)$$

The radiation heat flux can be found from:

$$q_r = \varepsilon \sigma (T_s^4 - T_\infty^4) \quad (4.11)$$

here  $\varepsilon$  is the emissivity and  $\sigma$  is the Stefan Boltzmann constant.

### 4.2.3 Top surface heat transfer coefficient

After evaluating the total heat loss from the water surface  $q_t$  as defined in Eq. (4.1), the overall heat transfer coefficient ( $h_{overall}$ ) can be evaluated from the following:

$$h_{overall} = \frac{q_t}{(T_s - T_\infty)} \quad (4.12)$$

The overall heat transfer coefficient was calculated at several water surface temperatures and a relation between the overall heat transfer coefficient and the surface temperature is plotted as shown in Figure 4.4.

From the relation shown in Figure 4.4, the equation of the best-fit curve can be obtained expressing the overall heat transfer coefficient as a function of the surface temperature. For this purpose, nonlinear regression method was used to generate a relationship for expressing  $h_{overall}$  as a function of water surface temperature. Gaussian function is implemented to describe the curve of  $h_{overall}$  as shown in Eq. (4.13), where  $T_s$  in Kelvin. To evaluate the discrepancy between the analytical values for  $h_{overall}$  and the values obtained from Eq. (4.13) the maximum and minimum errors were computed, which were found to be 0.0001 and 0.09 W/m<sup>2</sup>K respectively. Also, root-mean-square error (rmse) was found to be 0.0146 W/m<sup>2</sup> K. Hence, the new expression (Eq. (4.13)) describes well the curve for  $h_{overall}$  as shown in Figure 4.4.

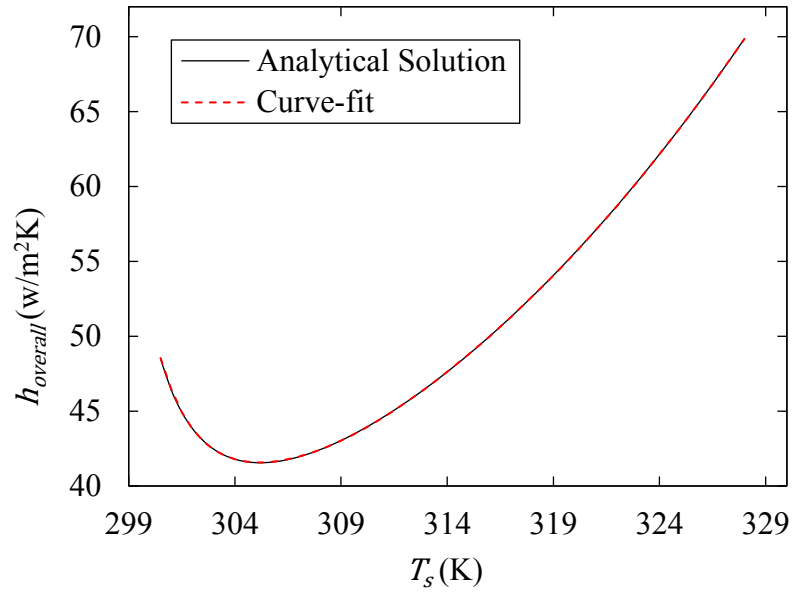


Figure 4.4: Overall heat transfer coefficient at a range of water surface temperature and its curve-fit from Eq. (4.13).

$$\begin{aligned}
 h_{overall} = & 100.54 \exp\left(-\left(\frac{T_s - 350}{27.81}\right)^2\right) \\
 & + 30.16 \exp\left(-\left(\frac{T_s - 308.21}{24.94}\right)^2\right) + 405 \\
 & \times 10^{12} \exp\left(-\left(\frac{T_s - 196.775}{18.4779}\right)^2\right) \\
 & + 11.19 \exp\left(-\left(\frac{T_s - 295.67}{9.27}\right)^2\right)
 \end{aligned} \tag{4.13}$$

Generally, the overall heat transfer coefficient,  $h_{overall}$ , increases as the surface temperature increase, except in the regions where the surface temperature is close to the ambient air temperature, it exhibits inverse behaviour. This is due to the behaviour of the flow regime; at lower temperature difference the heat and mass are being transported via laminar flow regime resulting in reducing  $h_{overall}$ , as the temperature difference increases  $h_{overall}$  declines. On the other side, while the surface temperature increases the  $Ra$  number increases, for heat and mass transfer, until it reaches a critical value where the flow starts to change to turbulent. Consequently, the overall heat transfer coefficient

increases. With further increase in  $T_s$ , the turbulence intensity is more likely to increase and hence enhances the heat transfer from the free water surface.

The advantage of the developing an expression for the heat transfer coefficient as a function of the water temperature is that during the numerical simulation  $h_{overall}$  depends only on the surface temperature and not on any other parameter. Whereas the water surface temperature is determined via the buoyancy force, which sets up a convection current.

### 4.3 Numerical modelling and validation

In order to validate the analytical treatment of the heat loss from the water surface, a cooling process of a warm water tank is numerically modelled. This also allows examining the applicability of applying an overall heat transfer coefficient at the water surface during the numerical simulation as a function of the water surface temperature as described Eq. (4.13).

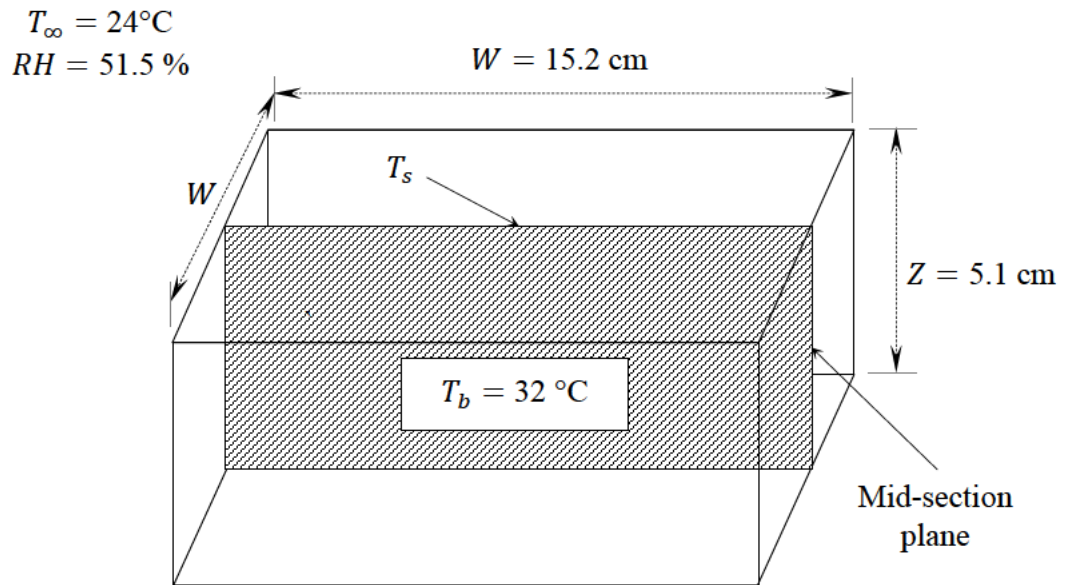


Figure 4.5: Schematic of the water tank used in the experiment conducted by Bower et al. [82].

The experiment performed by Bower et al. [82] is selected for the validation purpose. This experiment involves a cooling process of a water tank having a square footprint of the width of 15.2 cm and depth of 5.1 cm as shown in Figure 4.5. The tank contains a warm water having a bulk temperature of 32°C which is allowed to cool down in ambient air over a period of 60 minutes. The ambient air is at a temperature of 24°C and 51.5 % relative humidity. The commercial CFD package of ANSYS Fluent 16.0 was used to perform the transient calculations. Only one-quarter of the tank was considered as the computational domain through applying symmetry boundary conditions to reduce the computational expenses.  $k-\varepsilon$  turbulence model was used to add the turbulence effect. All the side and bottom walls of the tank were considered to be adiabatic as the tank was insulated. No-slip boundary condition was implemented at the walls of the tank except the water top surface which was characterised with zero shear stress. A convective boundary condition was applied at the top surface with heat transfer coefficient specified by the developed expression for  $h_{overall}$  Eq. (4.13). This expression is introduced to the software through a UDF. All water thermodynamic properties were considered to be temperature dependent and can be described in a polynomial form as:

$$\varphi = a_0 + a_1T + a_2T^2 + a_3T^3 \quad (4.14)$$

where  $\varphi$  represents all of the physical properties of water ( $\rho$ ,  $C_p$ ,  $k$ ,  $\mu$ ), and  $a_1$ ,  $a_2$ ,  $a_3$  and  $a_4$  are thermodynamics constant and their values are summarised in Table 4.1.

Table 4.1: Thermodynamic constants for physical properties of water [105].

Property	Thermodynamics constant			
	$a_0$	$a_1$	$a_2$	$a_3$
Density ( $\rho$ )	223.127	6.7678	-1.8538 x 10 <sup>-2</sup>	1.522 x 10 <sup>-5</sup>
Specific heat ( $C_p$ )	-5.084 x 10 <sup>-1</sup>	6 x 10 <sup>-3</sup>	-7.565 x 10 <sup>-6</sup>	-
Thermal conductivity ( $k$ )	-5.084 x 10 <sup>-1</sup>	6 x 10 <sup>-3</sup>	-7.565 x 10 <sup>-6</sup>	-
Dynamic viscosity ( $\mu$ )	6.3225 x 10 <sup>-2</sup>	-5.1485 x 10 <sup>-4</sup>	1.415 x 10 <sup>-6</sup>	-1.306 x 10 <sup>-9</sup>

The simulation results were validated against the experimental data reported by Bower et al. [82] in terms of the decline of water surface and bulk temperatures ( $T_s$  and  $T_b$  respectively) over a 60 minutes period during the cooling process as shown in Figure 4.6. Since the variation in the water temperature is very small as evidenced by Figure 4.7, less than  $0.4^\circ\text{C}$  for bulk and surface temperatures, the results of the water surface temperature and bulk temperature were collected as area average and volume average temperatures respectively.

Excellent agreement is seen for the water bulk temperature and slight over-prediction was observed for the surface temperature. This discrepancy can be due to the computational uncertainty in addition to, as discussed before, the errors associated with the experimental measurements and the assumptions were made during the analytical modelling of  $\dot{m}''$ . However, we are more interested in predicting the bulk temperature for applications such as cooling ponds.

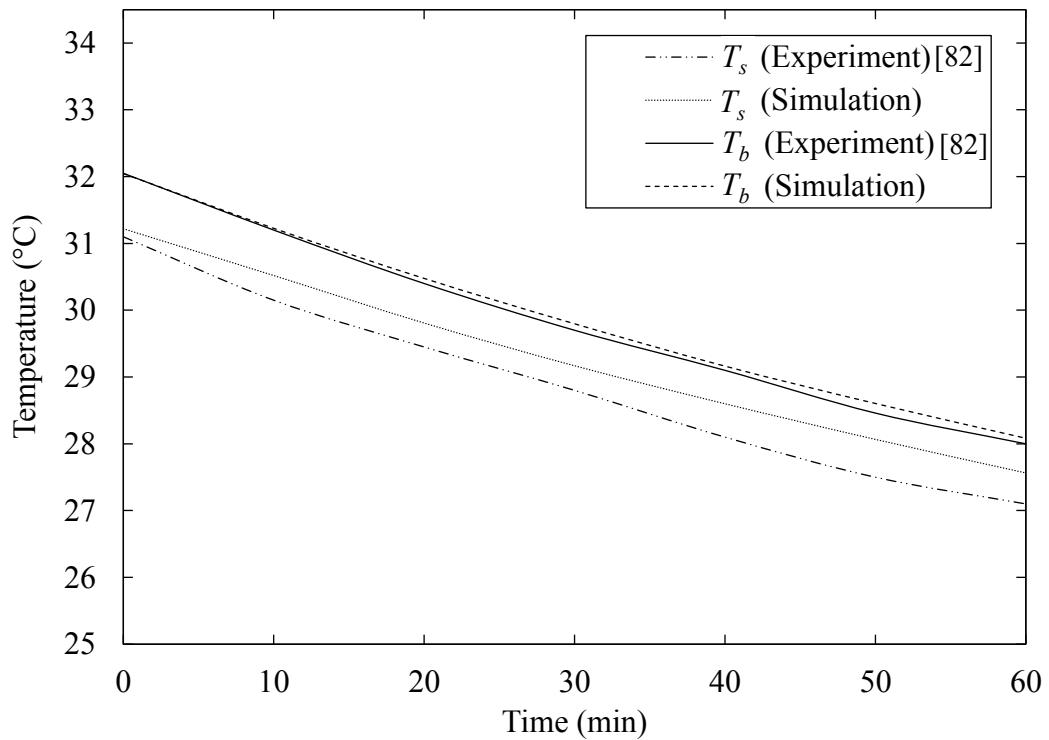


Figure 4.6: Numerical results and experimental data reported by Bower et al. [82] during the cooling process of the water tank.

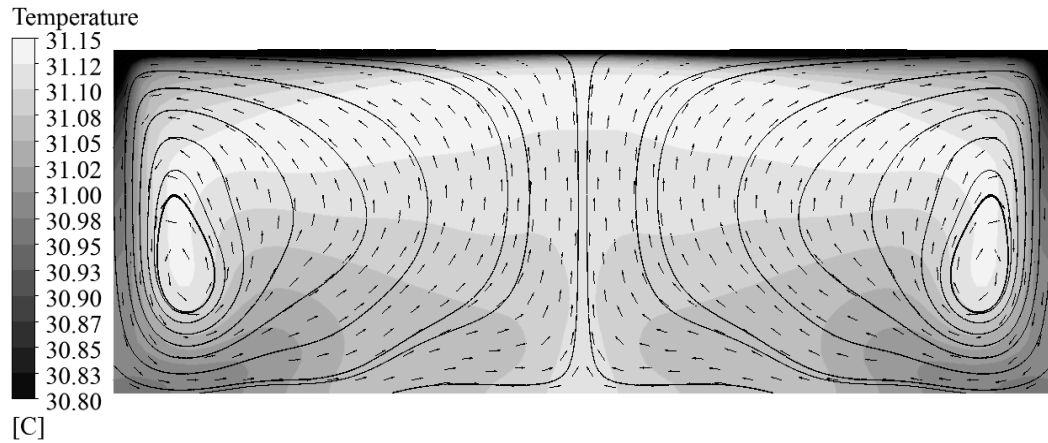


Figure 4.7: Temperature distribution and streamlines are shown on mid-section plane ( $t=600$  sec).

Figure 4.7 shows the temperature profiles as well as flow streamlines on the mid-section plane shown in Figure 4.5. The temperature contours display plumes of temperature gradients within the water layers. Since the top surface is directly exposed to the ambient temperature, the water surface cools down and become less than the bulk temperature. This temperature difference causes unstable temperature gradient within the water layers resulting in initiating the natural convection current.

As the temperature difference between the surface and the ambient increases, the intensity of the convection force increases transporting the warmer water to the top surface acting as an energy supplier to the surface layer, which is required to break the hydrogen bonds between the molecules of water allowing for evaporation to take place. This energy is dissipated through the water surface via the three heat transfer components as described in Eq. (4.1).

The distribution of the heat flux from the top water surface is presented in Figure 4.8. As expected, the free water surface is characterised by non-uniform distribution of heat flux as well as surface temperature. Despite the small variation in the surface temperature, which is about  $0.4^{\circ}\text{C}$ , a measurable variation in the heat flux distribution along the top surface was observed. The highest values of the heat loss were noted at the centre. This is due to the buoyancy driven flow is more active at the core of the tank than the sides, which supplies the centre region of the surface with a constant flow of warm water.

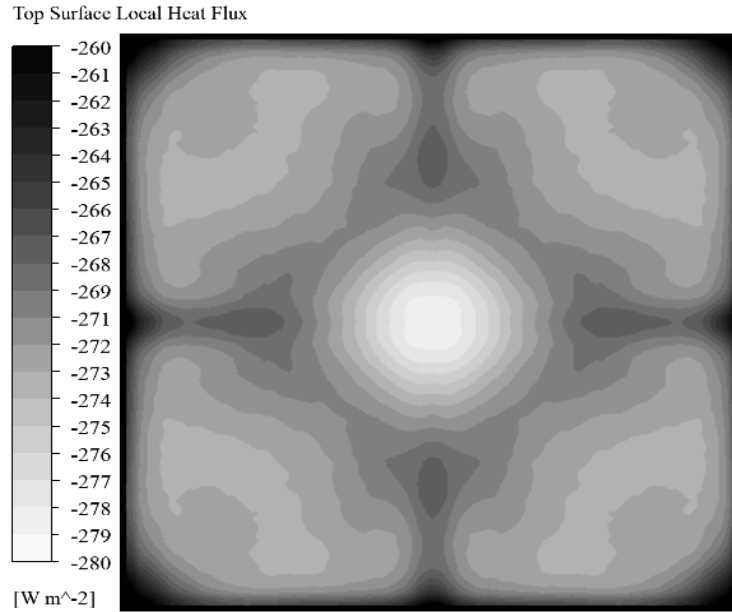


Figure 4.8: Distribution of localised heat loss from the free water surface ( $t=600$  sec).

Figure 4.9 shows a quantitative comparison between heat transfer components over a range of surface temperature. It is clear that the major heat loss is due to the evaporative component, particularly at lower surface temperatures. The proportion of radiation and convection heat fluxes is relatively small compared to the total heat flux. It is also obvious from Figure 4.9 that the total heat flux is directly proportional to the temperature difference, provided that the ambient temperature remains constant. The reason for this is that the convective and radiative heat fluxes are an explicit function of temperature difference as expressed in Eq. (4.10) and Eq. (4.11) respectively. Also, the evaporative heat flux is a function of the air and vapour densities at the interface and the ambient air as described in Eq. (4.3) and Eq. (4.4). Since the air density is temperature dependent, the evaporation heat flux is also a function of the temperature difference.

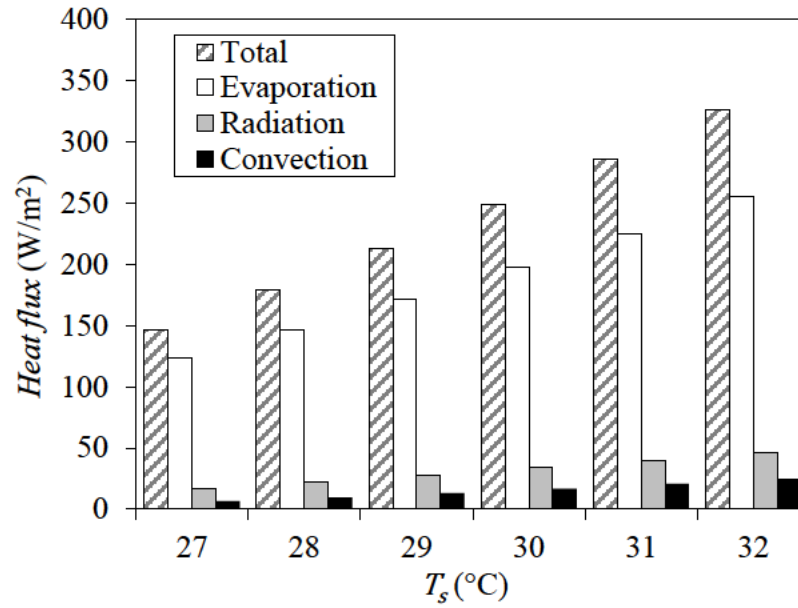


Figure 4.9: Proportions of the heat transfer components over a range of surface temperature.

#### 4.4 Considerations for high water temperatures

When the problem under considerations involves high values of water temperature, the evaporation rate can be significantly large to be modelled directly via the analogy between heat and mass convection as described in this chapter. Since this analogy is only valid for low mass flux where the flow of the evaporated water does not affect the velocity of the air above the water surface.

The definition of evaporation rate through concentration difference, Eq. (4.4), is not applicable for high water temperature up to the saturation, as it does not take into account the disruption caused to the stationary air by the upward flow motion (advection) at the air-water interface. Instead, Stefan's law is more suitable in these situations, since the effect of the upward flow motion was included in its fundamental derivation. The evaporation rate,  $\dot{m}_e$ , can be expressed via Stefan's law as follows [129, 130]:

$$\dot{m}_e = h_e \log \left( \frac{P - P_{v,s}}{P - P_{v,\infty}} \right) A_s \quad (4.15)$$

where  $A_s$  is the exposed water surface area to the ambient air.



In order to confirm the applicability of using Stefan's law as a substitute of concentration difference definition, Eq. (4.15) is used to model heat loss due to evaporation from a large-size cooling pond. The pond is having a total volume of 21905 m<sup>3</sup> and the exposed surface area to the ambient air is 3615 m<sup>2</sup>. A constant heat load of 300 MW is supplied to the water, which is enough to bring the water to boiling from 20 °C. The mass transfer coefficient,  $h_e$ , is calculated in the same manner as described in Eq. (4.3). The ambient air is considered to be dry and held at constant temperature of 20 °C and atmospheric pressure. The expected evaporation rate at the boiling due to supplied heat of 300 MW is 132.4 kg/s which was calculated directly from:

$$\dot{m}_e = \frac{\dot{Q}}{h_{fg}} \quad (4.16)$$

where  $\dot{Q}$  is the supplied heat to the water.

The evaporation rate from the pond water is being calculated by using concentration difference and Stefan's law definitions as shown in Figure 4.10. Both definitions predict almost the same value of evaporation rate for water temperature ranges from 20 °C up to approximately 74 °C. However, from this point up to the saturation temperature, which is 100 °C, a huge deviation is observed between both definitions. At saturation, the concentration difference definition is largely under-predicted the evaporation rate by almost 74 % from the expected value of 132.4 kg/s. On the other hand, Stefan's law provides a good estimation of the evaporation rate as shown in Figure 4.10. It can be seen that the water temperature is very close to saturation with a value of 99.6 °C. This implies that Stefan's law is more applicable when the problem involves a temperature approaches the saturation.

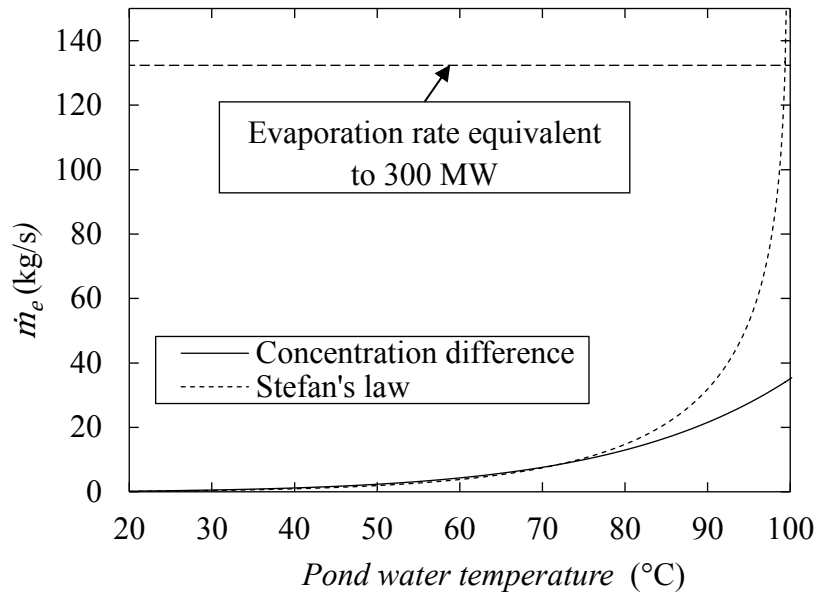


Figure 4.10: Comparison of evaporation rates predicted using Stefan's law and concentration difference definitions.

#### 4.5 Summary

Treatment of the boundary conditions at the free water surface was achieved by analytically modelling the heat transfer components and developing an expression for the overall heat transfer coefficient,  $h_{overall}$ , as a function of the surface temperature. The evaporative component was estimated via  $Sh - Ra$  power law considering the exponent  $n = 1/3$  to diminish the dependence on characteristic length. The developed expression of  $h_{overall}$  was used to model the cooling processes of a warm water tank numerically where  $h_{overall}$  was applied at the free water surface to take into account the heat loss at the surface. The results of this simulation were in agreement with the experimental data. In addition, it was found from the analytical solution that the heat loss due to the evaporation component represents the major portion of the total heat loss over the given range of temperature, this portion is ranging between 78% - 84%.

The advantage of the proposed modelling methodology is that it allows simulation of the heat loss from water surface due to evaporation without the need to use the multiphase models with reasonable accuracy.

In this chapter, the ambient conditions,  $RH$  and  $T_{\infty}$ , were assumed constant which were almost true as the quantity of the evaporated water was relatively small to change these conditions. This is not true for the situations in the SNF cooling ponds where the evaporation can significantly affect the relative humidity and the ambient temperature. However, improvement can be achieved by taking into account the variation in  $RH$  and  $T_{\infty}$  due to the transport of water vapour from the water body to the ambient air that will be discussed in the next chapter. In addition, water temperature in the cooling ponds can reach the saturation temperature and hence the evaporation rate is more appropriate to be expressed via the definition of Stefan's law where advection is considered.

## Chapter 5 Analytical Modelling of SNF Cooling Pond

### 5.1 Introduction

In this chapter, the suitability of using well-mixed approach for developing an analytical model for a large-scale SNF cooling pond is explored. The well-mixed approach is widely used in ventilation applications to predict the concentration of a specific gas or vapour in the room [2]. This model treats the room as a large box, which is perfectly mixed so that the concentration of the gas or vapour is uniform.

An analytical model based on well-mixed hypothesis was developed for the cooling pond at the Sellafield site using Microsoft Excel spreadsheet. This model was validated against reliable data reported in the literature for the Maine Yankee spent fuel cooling pond [45]. In addition, the reliability of the spreadsheet model predictions was examined for a large-scale spent fuel cooling pond by comparing its outcomes with collected data from the actual cooling pond at the Sellafield site.

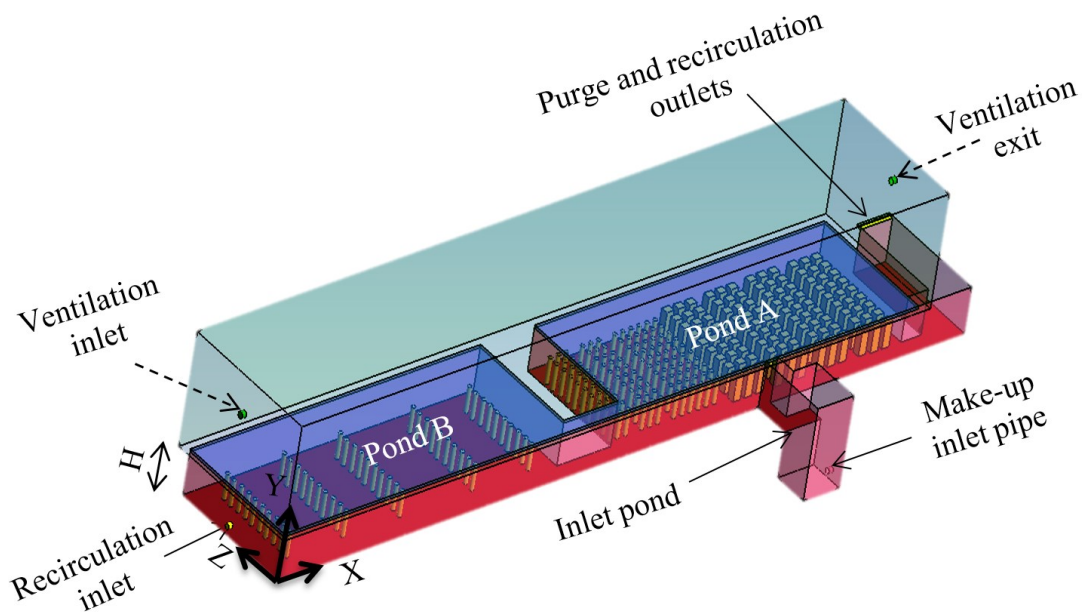


Figure 5.1: Schematic diagram of Sellafield SNF cooling ponds.

## 5.2 Sellafield spent fuel cooling ponds

Figure 5.1 shows a schematic diagram of Sellafield cooling ponds in a three-dimensional view. The ponds are characterised by large dimensions of 160m x 25m x 8m and the water surface area is about 3615 m<sup>2</sup>. The whole installation consists of three different ponds. Pond A and Pond B store the spent fuel while the inlet pond supplies make-up. Decay heat removal takes place via three mechanisms: ventilation, make-up water and water recirculation as illustrated in Figure 5.2. When the decay heat is released from the fuel rods, the water temperature starts to increase as does the heat transfer from the water surface to the ambient air. The heat transfer from the water surface takes place via three heat transfer modes: evaporation, convection, and radiation. The ventilation system is used to replace the warm air within the building with relatively cooler air. The major heat loss from the water surface is due to the evaporative component; however, this is associated with the loss of pond water, which may lead to a significant drop in the water level in the long term. For this reason, make-up water can be supplied to the pond to prevent the potential risk of uncovering the fuel assemblies. Furthermore, make-up water can be used for purging the pond water as it has been demineralised before reaching the pond. The temperature of the make-up water is largely determined by the outside temperature, as it is supplied via external pipework from a water treatment plant some distance away from the site.

Recirculation can be used on occasions when cooling by ventilation and make-up water is not sufficient to control the pond temperature. Cooling via recirculation is achieved by feeding some of the pond water through a cooling tower which then re-enters the pond a few degrees cooler.

██

██

██

██

██

██

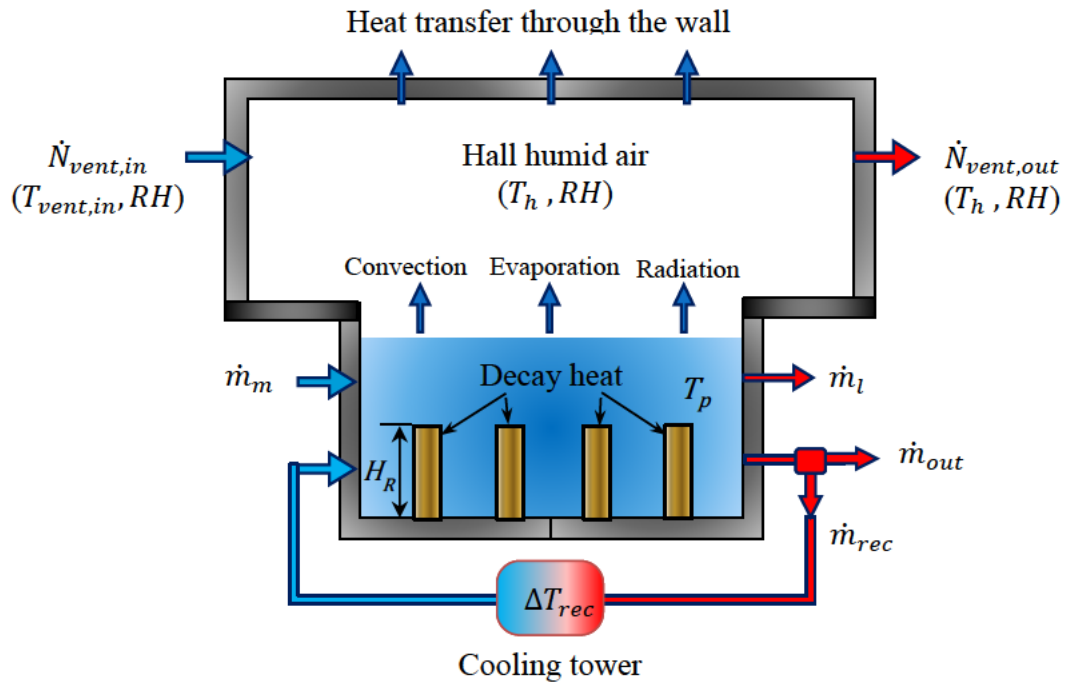


Figure 5.2: Description of the processes taking place within the pond installation.

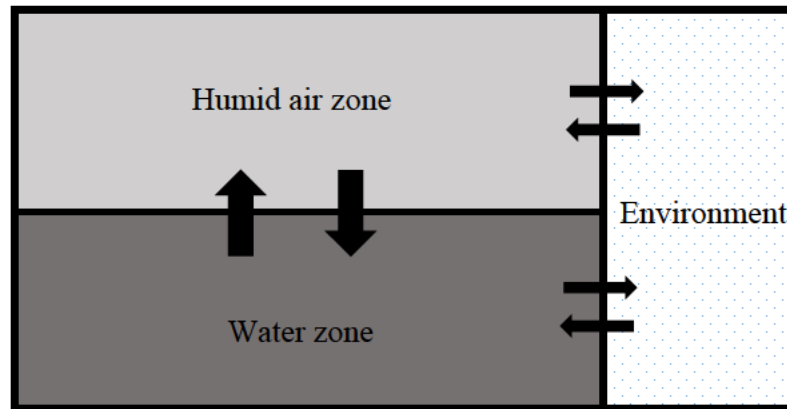


Figure 5.3: Zones used in the spreadsheet model.

### 5.3 Spreadsheet model

While developing the spreadsheet model for the cooling ponds, the whole pond installation is divided into two zones: the humid air zone and water zone as shown in Figure 5.3. These zones can be described as a source and a sink, where the water zone acts as the source of water vapour and heat energy and humid air zone acts as the sink.

Energy and mass transfer with the environment, the third zone, is also integral part of the model

### 5.3.1 Modelling assumptions

The well-mixed approach is adopted in both zones. Since the fuel assemblies are located at the bottom of the pond, the water temperature for the bulk of the pond can be assumed to be uniformly distributed due to buoyancy-induced convection. In a similar manner, the temperature of the humid air zone can be treated a single value due to the large volume and the flow process of evaporation. Experimental data from the site also support the above assumption. However, the validity of this assumption will be scrutinised in Chapter 6 by performing CFD simulation on the water body.

### 5.3.2 Modelling methodology

The proposed spreadsheet model is based on solving conservation of mass and energy equations for the water body and humid air zone above the water surface. The model treats each zone as a single control volume and takes into account heat and mass transfer as well as interaction at the air-water interface. The environment provides boundary conditions such as outside temperature and relative humidity in order to solve the ODEs involved water and humid air zones. The forward time marching approach is adopted to solve a system of differential equations of mass and energy using Euler's forward method as a discretization scheme [131]. This is an explicit method where the solution of the current time step depends on information from the previous step. The general form of Euler's method is shown in Eq. (5.1). The advantage of this method is that it does not require significant computing time or power and allows the calculations to be performed using Microsoft Excel spreadsheet [132]. In addition, the model is developed also using Matlab software [133].

$$y^{n+1} = y^n + f(t^n, y^n)\Delta t \quad (5.1)$$

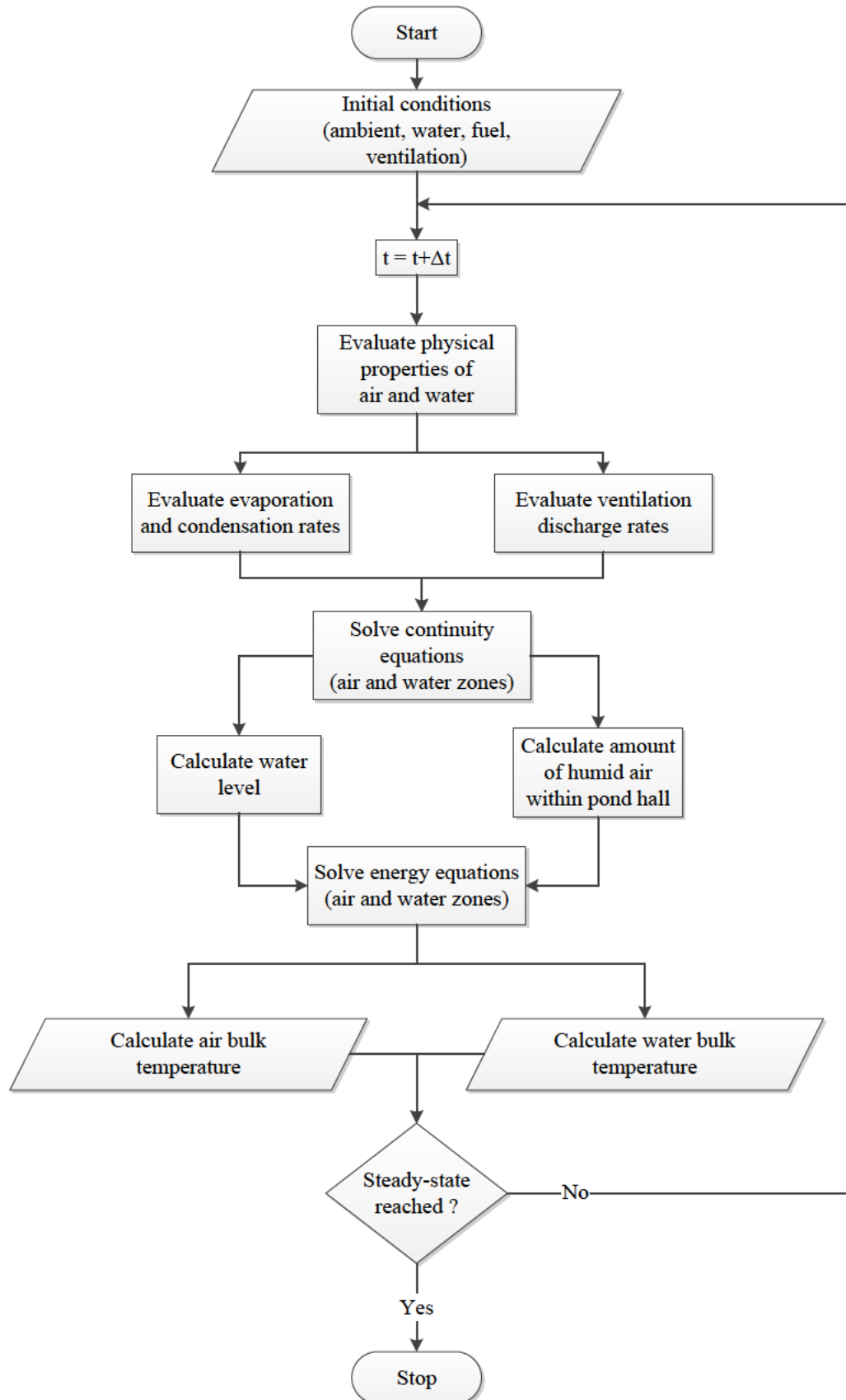


Figure 5.4: Flowchart representation of the spreadsheet model.



A diagrammatic representation of the spreadsheet model is illustrated in Figure 5.4. At the beginning, initial values are given to start the solution. The physical properties of air and water are evaluated at each time step. After that, the mass fluxes across the pond structure, evaporation and condensation rates, are estimated along with the ventilation discharge rate. At this point, two mass balance equations are solved in order to calculate the amounts of air and water, which are needed to solve the energy equation in each zone. Finally, air and water temperatures are obtained for this time step. The new temperature will be used to recalculate the physical properties of air and water for the next time step. This is an iterative process that will continue until the steady state is reached.

### 5.3.3 Mass balance of water zone

The water in the pond is evaluated at each time step, considering any change due to the supply of make-up water ( $\dot{m}_m$ ) and loss of water due to evaporation ( $\dot{m}_e$ ), leakage ( $\dot{m}_l$ ), and water outflow ( $\dot{m}_{out}$ ). Therefore, the mass balance equation for pond water can be written as following:

$$m_p^{n+1} = m_p^n + (\dot{m}_m - \dot{m}_{out} - \dot{m}_e - \dot{m}_l)^n \Delta t \quad (5.2)$$

where  $m_p$  is the total mass of water within the pond,  $\Delta t$  is the time step and  $n$  is the number of iteration.

The following equation describes how the water outflow from the pond is controlled. When the water loss due to evaporation and leakage is greater than the supplied make-up water, no water outflow will be permitted. Similarly, in situations when the water level ( $H_p$ ) is lower than its designed value ( $H_D$ ), no water outflow is allowed until the water level reaches this value. The following relationship explains how the outflow of water can be mathematically expressed:

$$\dot{m}_{out} = \begin{cases} 0 & \text{if } (\dot{m}_e + \dot{m}_l) \geq \dot{m}_m \\ \dot{m}_m - \dot{m}_e - \dot{m}_l & \text{if } (\dot{m}_e + \dot{m}_l) < \dot{m}_m \\ 0 & \text{if } H_p \leq H_D \\ \left[ \frac{\rho_w A_p (H_p - H_D)}{\Delta t} \right] + (\dot{m}_m - \dot{m}_e - \dot{m}_l) & \text{if } H_p > H_D \end{cases} \quad (5.3)$$

where  $\rho_w$  is the water density and  $A_p$  is the water surface area of the pond. The evaporation rate before the pond water starts to boil can be estimated using Stefan's law [129]. The following equations show how the evaporation rate can be estimated before and during boiling.

$$\dot{m}_{ev} = \begin{cases} h_{ev} \log \left( \frac{P_t - P_{v,s}}{P_t - P_{v,\infty}} \right) A_p & \text{if } T_p < T_{sat} \\ \dot{Q}_d / h_{fg} & \text{if } T_p \geq T_{sat} \end{cases} \quad (5.4)$$

where,  $P_{v,s}$  is the saturated vapour pressure at surface temperature, and  $P_{v,\infty}$  is the vapour pressure at the hall temperature,  $P_t$  is the total pressure of humid air inside the hall,  $h_{fg}$  is the latent heat of vaporization for water,  $\dot{Q}_d$  is the released decay heat from the fuel assemblies,  $T_p$  is the pond water temperature,  $T_{sat}$  is water saturation temperature and  $h_{ev}$  is the evaporative mass transfer coefficient which can be calculated using the analogy between heat and mass transfer using Sherwood–Rayleigh power law,  $Sh - Ra$ , as shown below [129]:

$$Sh = \begin{cases} 0.54 Ra^{1/4} & \text{if } 10^4 \leq Ra \leq 10^7 \\ 0.15 Ra^{1/3} & \text{if } 10^7 \leq Ra \leq 10^{11} \end{cases} \quad (5.5)$$

### 5.3.4 Pond water elevation

The pond water level is calculated by knowing the water volume and the surface area of the pond water. When the water level drops to a value less than the rack height ( $H_R$ ) shown in Figure 5.2, the surface area of the water will be limited to the surface area of

water between the rack assemblies ( $A_R$ ). The water level at every time step is updated according to the mass of water available in the pond, as shown in the following equation:

$$H_p = \begin{cases} \left[ \left( \frac{m_p}{\rho_w} - A_r H_r \right) / A_p \right] + H_r & \text{if } H_p \geq H_r \\ \left( \frac{m_p}{\rho_w} \right) / A_r & \text{if } H_p < H_r \end{cases} \quad (5.6)$$

### 5.3.5 Mass balance of humid air zone

Humid air is considered as a mixture of dry air and water vapour. Both dry air and water vapour at low partial pressure can be treated as a perfect gas. When dealing with humid air, it is more convenient that the mass of the humid air to be expressed in mole basis for the dry air and vapour separately.

In order to evaluate the amount of dry air ( $N_a$ ) and vapour ( $N_v$ ) inside the pond hall, the mass balance equation across the hall is applied as shown in Equations (5.7) and (5.8). This mass balance takes into account the ventilation inlet ( $\dot{N}_{vent,in}$ ) and discharge ( $\dot{N}_{vent,out}$ ) flow rates as well as evaporation and condensation ( $\dot{m}_{con}$ ) rates.

$$N_a^{n+1} = N_a^n + (y_{vent,in}^a \dot{N}_{vent,in} - y_h^a \dot{N}_{vent,out})^n \Delta t \quad (5.7)$$

$$N_v^{n+1} = N_v^n + \left( \dot{N}_{vent,in} - y_h^v \dot{N}_{vent,out} - \frac{\dot{m}_e}{M_v} + \frac{\dot{m}_{con}}{M_v} \right)^n \Delta t \quad (5.8)$$

where  $y_h^a$  and  $y_h^v$  are the molar fraction of dry air and water vapour, respectively, which can be found from:

$$y_h^a = \frac{N_a}{N_h} \quad (5.9)$$

$$y_h^v = \frac{N_v}{N_h} \quad (5.10)$$

$$N_h = N_a + N_v \quad (5.11)$$

Here  $N_h$  is the total molar mass of the humid air inside the pond hall. The flow rate of the ventilation inlet is an initial input condition where the differential pressures drive the ventilation discharge and can be computed from:

$$\dot{N}_{vent,out} = \rho_\infty M_v A_{duct} \sqrt{\frac{2(P_t - P_{atm})}{\rho_\infty}} \quad (5.12)$$

where  $\rho_\infty$  is the density of the humid air inside the pond hall,  $M_v$  is the molecular weight of water vapour,  $A_{duct}$  is the cross-sectional area of the ventilation discharge duct,  $P_{atm}$  is the outside atmospheric pressure  $P_t$  is the total pressure of humid air inside the pond hall and can be evaluated as follow:

$$P_t = \left( \frac{T_h R_o}{V_h} \right) N_h \quad (5.13)$$

The estimation of the condensation rate is similar to the calculation of the evaporation rate:

$$\dot{m}_{con} = h_{con} (\rho_{v,\infty} - \rho_{v,wall}) A_h \quad (5.14)$$

where,  $\rho_{v,wall}$  is the saturated vapour density at wall temperature,  $A_h$  is surface area of the inner walls of the pond hall and  $h_{con}$  is the condensation mass transfer coefficient which can be calculated from:

$$Sh = 0.10 Ra^{1/3} \quad (5.15)$$

### 5.3.6 Energy balance of water zone

The energy contained in the water body is integrated over time taking into account the heat released from the fuel, the heat flux from the water surface and the energy associated with the water inlets and outlets:

$$T_p^{n+1} = T_p^n + (\dot{Q}_d + \dot{m}_m C_w T_m - \dot{m}_{out} C_w T_p - \dot{m}_e C_w T_p - \dot{m}_{rec} C_w \Delta T_{rec} - \dot{Q}_s)^n \frac{\Delta t}{m_p C_w} \quad (5.16)$$

where  $C_w$  is the specific heat of water,  $T_m$  is the temperature of the make-up water,  $\dot{m}_{rec}$  is the recirculation flow rate,  $\Delta T_{rec}$  is the temperature drop in the cooling tower which is controlled by the wet bulb temperature of the outdoor air ( $T_{wb}$ ) and the cooling tower efficiency. The efficiency of the cooling tower is a measure of how much is the ideal cooling is actually achieved in the cooling tower, which can be expressed as [134]:

$$\zeta = \frac{\Delta T_{rec}}{T_p - T_{wb}} \quad (5.17)$$

and  $\dot{Q}_s$  is the total heat transfer at the air-water interface which can be estimated as shown below:

$$\dot{Q}_s = \dot{Q}_e + \dot{Q}_r + \dot{Q}_c \quad (5.18)$$

where  $\dot{Q}_e$  is the evaporative heat transfer,  $\dot{Q}_r$  is the radiative heat transfer, and  $\dot{Q}_c$  is the convective heat transfer. These three heat transfer modes can be evaluated from the following expressions:

$$\dot{Q}_e = \dot{m}_e h_{fg} \quad (5.19)$$

$$\dot{Q}_r = A_p \varepsilon \sigma (T_p^4 - T_h^4) \quad (5.20)$$

$$\dot{Q}_c = A_p h_c (T_p - T_h) \quad (5.21)$$

Here  $\varepsilon$  is emissivity,  $\sigma$  is the Stefan Boltzmann constant,  $T_{wall}$  is the wall inner surface temperature of the hall,  $h_c$  is the convection heat transfer coefficient at the water surface which may be evaluated by using the Nusselt– Rayleigh power law,  $Nu - Ra$  , as shown below:

$$Nu = \begin{cases} 0.54 Ra^{1/4} & \text{if } 10^4 \leq Ra \leq 10^7 \\ 0.15 Ra^{1/3} & \text{if } 10^7 \leq Ra \leq 10^{11} \end{cases} \quad (5.22)$$

### 5.3.7 Energy balance of humid air zone

The heat loss from the water surface is gained by the ventilated air, which results in an increase in air temperature. In order to calculate the air temperature inside the pond hall, the energy balance is performed across the hall as shown below:

$$T_h^{n+1} = T_h^n + \left[ \dot{m}_e h_v(T_p) + \dot{Q}_c - \dot{Q}_{wall} - \dot{m}_{con} h_{fg} + \dot{Q}_{vent,in} - \dot{Q}_{vent,out} \right]^n \frac{\Delta t}{[N_a M_a C_{p,a} + N_v M_v C_{p,v}]} \quad (5.23)$$

where  $h_v(T)$  is the specific enthalpy of water vapour at a given temperature and can be calculated using the shown below [135]. However, this relationship is valid only for low values of pressure.

$$h_v(T) = 2500 + 1.82 (T - 273) \quad (5.24)$$

In order to obtain the heat energy associated with the incoming ventilated humid air ( $\dot{Q}_{vent,in}$ ) and the discharged humid air by ventilation ( $\dot{Q}_{vent,out}$ ), the following relationships are used:

$$\dot{Q}_{vent,in} = y_{vent,in}^a \dot{N}_{vent,in} C_{p,a} T_{vent,in} + y_{vent,in}^v \dot{N}_{vent,in} h_v(T_{vent,in}) \quad (5.25)$$

$$\dot{Q}_{vent,out} = y_h^a \dot{N}_{vent,out} C_{p,a} T_h + y_h^v \dot{N}_{vent,out} h_v(T_h) \quad (5.26)$$

Here,  $y_{vent,in}^a$  and  $y_{vent,in}^v$  are the molar fractions of the ventilation inlet dry air and vapour respectively,  $C_{p,a}$  is the specific heat of the dry air, and  $T_{vent,in}$  is the ventilation inlet temperature which is assumed to be the same as the outside temperature. The heat transfer through the walls of the pond hall ( $\dot{Q}_{wall}$ ) is computed according to:

In order to determine  $T_{wall}$ , an energy balance is performed across the walls of the pond hall where the wall thickness ( $x$ ) is divided to uniform increments of  $dx$ . The energy equations for the interior and surface layers can be written as follow:

$$T_i^{n+1} = T_i^n + \frac{k}{dx C_{wall} \rho_{wall}} \left( \frac{T_{i-1} - T_i}{dx} - \frac{T_i - T_{i+1}}{dx} \right)^n \Delta t \quad (5.27)$$

$$T_i^{n+1} = T_i^n + \frac{k}{dx C_{wall} \rho_{wall}} \left( \frac{T_{wall} - T_i}{dx/2} - \frac{T_i - T_{i+1}}{dx} \right)^n \Delta t \quad (5.28)$$

where  $i$  is the index of the wall layers,  $C_{wall}$  is the specific heat of the walls material,  $\rho_{wall}$  is the density of the walls material, and  $k$  is the thermal conductivity of the walls material. The inner surface temperature can be calculated considering the heat balance across this surface as shown below:

$$\dot{Q}_r + (T_h - T_{wall}) A_h h_{in} = \frac{T_{wall} - T_i}{dx/2} A_h k \quad (5.29)$$

where  $h_{in}$  is the convective heat transfer coefficient for the inner surface of the pond hall. Finally, the solution is considered to be at steady state when the relative difference between the current iteration and the previous iteration is less than 0.01%. The steady-state criterion is expressed as shown below:

$$\text{Steady-state criterion} = \frac{|T_p^{n+1} - T_p^n|}{T_p^n} \times 100 \quad (5.30)$$

However, in some cases the criterion for the steady-state condition cannot be achieved; for instance, when the pond is suffering from loss of cooling. In this case, the temperature of the pond water will continue to increase until the saturation is reached. During this time, the water level may drop until the pond dries out unless sufficient make-up water is provided to compensate for the evaporated water.

The heat loss from the pond water to the concrete wall is not considered in this study as it makes only a very small contribution to the total heat loss from the pond's structure. This is because the ponds are surrounded at the sides and floor by a very thick layer of concrete.

As mentioned before, the calculations were performed using the explicit Euler's method, which is known to be conditionally stable, therefore, a stability analysis is required [136]. Investigation of the numerical behaviour of the model shows that the stability of is more dominated by the stability of the differential equations rather than the used method. The highest instability was observed in the mass balance equation for the airside. This is due to the pressure fluctuation, which is mostly controlled by the ventilation discharge. Therefore, a stability analysis is conducted on the mass balance equation for the humid air zone and is given in Appendix A. However, from the analysis, the stable time step can be expressed as:

$$\Delta t \leq \frac{2}{\emptyset} \quad (5.31)$$

where  $\emptyset$  is equivalent to:

$$\emptyset = \frac{A_{duct} R_o T_h}{2V_h} \sqrt{\frac{2\rho_\infty}{\left(\frac{T_h R_o}{V_h}\right) N_h^n - P_{atm}}} \quad (5.32)$$



Note that  $\Delta t$  changes as  $N_h^n$  changes. Thus, the stable step size changes as the solution advances. However, keeping the time step within the criterion shown in Eq. (5.31) not only ensures stability, but it also ensures that the results are not very sensitive to the time step. According to this criterion, the used time step in all the cases presented in this study is 5 sec.

## 5.4 Spreadsheet model validation

The spreadsheet thermal model of the cooling pond is validated against available data for two different cooling ponds as shown below:

1. Maine Yankee spent fuel pool, Wiscasset, USA [45]
2. Sellafield cooling pond, UK

### 5.4.1 Validation with Maine Yankee pool data

The Maine Yankee spent fuel pool is a relatively small cooling pond located at the reactor site, with dimensions of 12.6 m long, 11.3 m wide and 11.1 m deep. Carlos et al. [45] used TRACE best estimate code to analyse the response of the cooling pond in different scenarios. During their calculations, no heat loss was considered at the free water surface except when the water has reached its saturation temperature (100 °C) with the initiation of boiling. However, this assumption does not have a significant effect on the results, as the proportion of heat loss from the water surface before boiling is not significant compared to the heat loss to the supplied water. This is owing to the small surface area at the air-water interface.

The spreadsheet model is used to perform calculations on the Maine Yankee spent fuel pool, Wiscasset, USA [45] and the results obtained are compared against the published data for this pool. These calculations are developed for three cases: (a) steady-state, (b) licensing, and (c) accident scenarios.

In the paper reported by Carlos et al. [45], the temperature data were available for the steady-state case in the form of actual temperature measurements collected from the Maine Yankee spent fuel pool. For the licensing case, the temperature data were

calculated by GFLOW software [57], while the TRACE best estimate code was used for the pool temperature under the accident scenarios.

#### 5.4.1.1 *Steady-state and licensing cases*

The input parameters used in the calculations of the steady-state and licensing cases are summarised in Table 5.1. In the same table, the outcomes from the validation exercise using the present spreadsheet model are presented. The heat load in the licensing case corresponds to the maximum expected heat generation from the fuel elements.

The results predicted by the spreadsheet model are in good agreement with the available data for the Maine Yankee spent fuel pool as can be seen in Table 5.1. However, the spreadsheet model underestimates the pond water temperature by 3 % and 2.6 % for steady-state and licensing cases respectively. When all of the heat transfer modes from the water surface are deactivated in the spreadsheet calculations, except for boiling, the underestimation errors of the water temperature decreased to 1.9 % and 0.9 % for the steady-state and licensing cases respectively. This implies that the heat loss from the water surface before boiling is relatively less significant, as mentioned before.

Table 5.1. Input data and comparison between values predicted by the spreadsheet model and data for the Maine Yankee pool [45].

Parameters / Case		Steady State Case	Licensing Case
Heat load (MW)		3.3	6.4
Make-up water flow rate (kg/s)		98	97.6
Make-up water temperature (°C)		26.1	51.7
Water bulk temperature (°C)	Maine Yankee pool	36.7 (measured)	68 (GFLOW)
	Present spreadsheet model	35.6	66.2
	errors	- 3 %	- 2.6 %

#### 5.4.1.2 *Accident case*

The outcomes from the licensing case were used as the input data for the accident scenario except for the initial water level which is considered to have a value of 4.56 m as measured from the bottom of the pond. In the TRACE simulation for the accident case, it was

assumed that the pumps which supply the pond with the cooling and make-up water, have stopped functioning and the only heat loss mechanism available is the heat loss to the surroundings by means of boiling. Therefore, in the spreadsheet calculations, the heat transfer modes from the water surface were deactivated and the only heat transfer permitted is due to boiling.

Figures 5.5 and 5.6 show comparisons between the results predicted by the spreadsheet model and the TRACE data for the accident scenario in terms of water temperature and drop of pond water level respectively. In Figure 5.5, for up to one hour the same linear trend is observed but a clear shift of 1.8 °C is recorded, the reason for which is not obvious from the original paper [45].

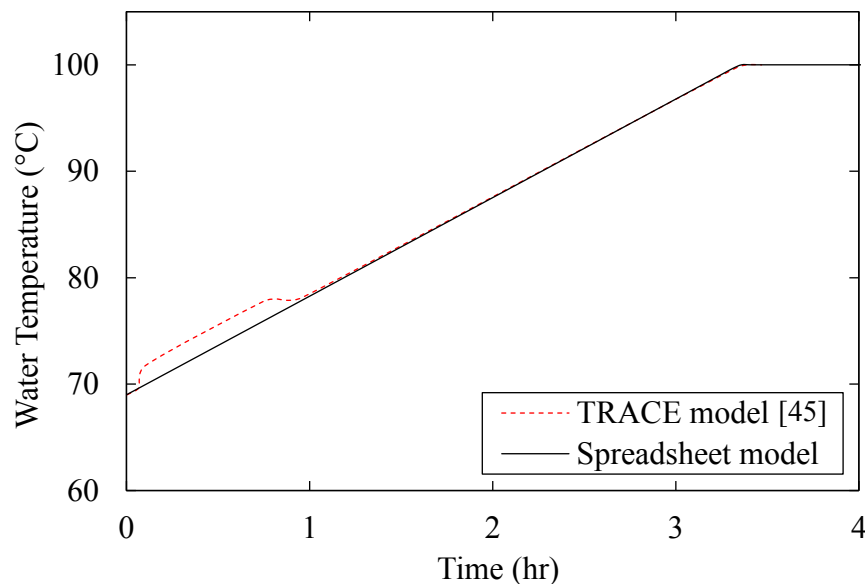


Figure 5.5. Water temperatures that obtained by the spreadsheet model and Maine Yankee pool [45] under the accident case.

Figure 5.6 shows a sudden drop in water level over a very short time (something similar to purging) but the reason for such behaviour was also not explained. These behaviours may be due to assumptions made which are unknown to us. In general, good agreement can be observed between the spreadsheet model and the TRACE best estimate code.

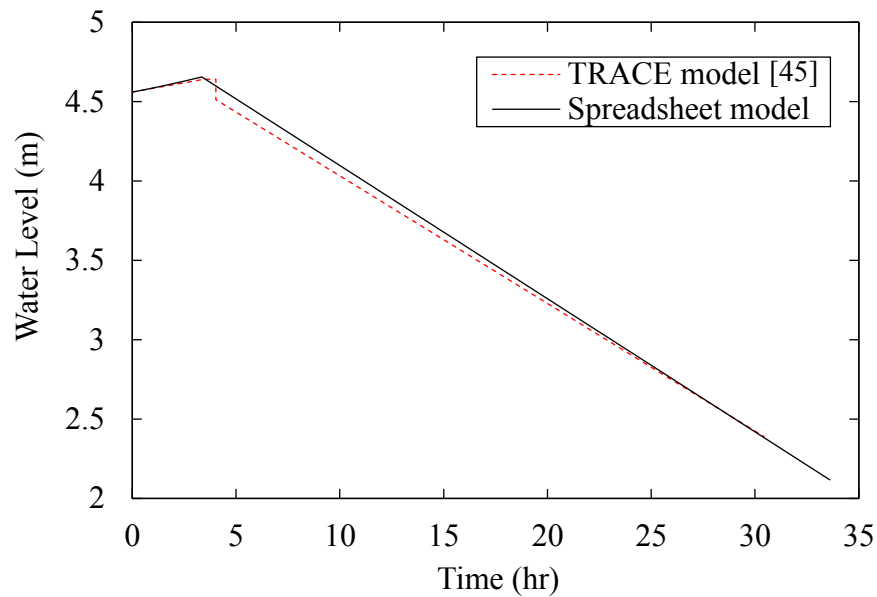


Figure 5.6. Water level that obtained by the spreadsheet model and Maine Yankee pool [45] under the accident case.

#### 5.4.2 Validation with Sellafield cooling pond data

The validation exercise is further extended to consider a large-scale cooling pond to examine the effect of pond size on the spreadsheet model's prediction. The cooling ponds at the Sellafield site have 727 fuel assemblies, whereas only 120 of the fuel assemblies are active and generate heat. The fuel assemblies are arranged within the cooling ponds in three groups depending on the age of the spent fuel, where the total heat released is 340 kW as shown in Table 5.2.

Table 5.2. Breakdown of the heat generated from the fuel assemblies.

Group	1	2	3	Total
Number of fuel assemblies	50	25	45	120
Heat load (kW)	0.9	1.9	5.5	340

The validation is performed for three different operational configurations and the input parameters used during these calculations are summarised in Table 5.3. Comparisons between the measured data and the results predicted by the spreadsheet model are

presented in tabular form as shown in Table 5.4. It can be seen from the comparisons that the spreadsheet model has predicted the water temperature as well as the hall air temperature within a good level of accuracy. However, the spreadsheet model has slightly overestimated the water temperature. The maximum observed error in the predictions of water temperature is 3.56 %, where the maximum recorded error in the hall air temperature is - 4.55 %.

Table 5.3. Input parameters used in validation with the Sellafield spent fuel cooling ponds data.

Parameters	Case 1	Case 2	Case 3
Heat load (kW)	340	340	340
Outside environment temperature (°C)	11	14	19
Recirculation flow rate (kg/s)	105.5	47.5	4.05
Temperature drop in cooling tower (°C)	0	0	1
Make-up rate (kg/s)	3.47	3.62	3.84
Make-up temperature (°C)	11	14	19
Ventilation inlet rate (m <sup>3</sup> /s)	12	12	12

The percentage contribution of each heat removal mode to the total heat loss is shown in Figure 5.7 for the three validation cases. These contributions are evaluated when the steady state is reached. From the results shown in this figure, it is very clear that the heat loss from the water surface is significant as it represents about 50% of the total heat loss from the ponds. However, under different configurations, these ratios can vary significantly. For an instant, when the make-up water or recirculation flow rates are high, this will lead to much higher contributions of these heat removal modes over the surface heat loss.

Table 5.4. Comparison between measured and predicted results for Sellafield pond.

	Water Temperature (°C)			Hall Air Temperature (°C)		
	Measured	Predicted	Error (%)	Measured	Predicted	Error (%)
Case 1	20.6	21.3	3.39 %	18.2	17.5	- 3.85 %
Case 2	23.2	23.9	3.01 %	19.8	18.9	- 4.55 %
Case 3	25.3	26.2	3.56 %	21.7	21.1	-2.76 %

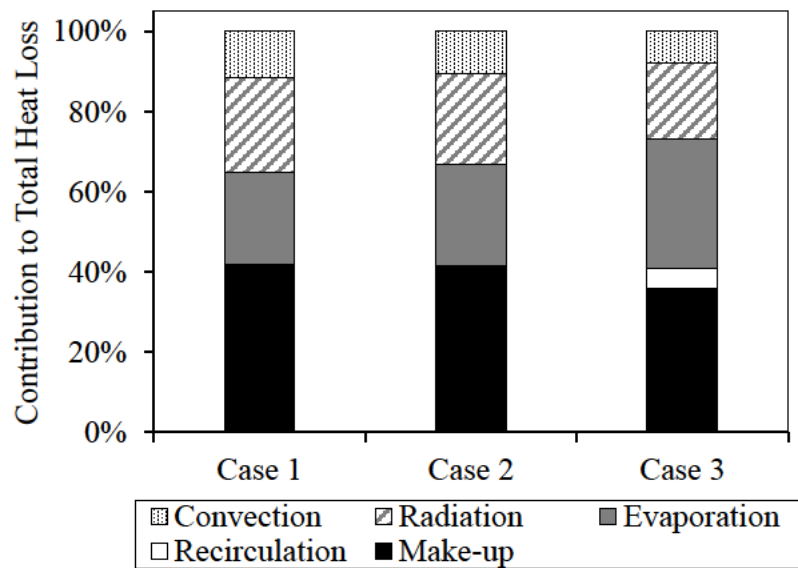


Figure 5.7: Contribution percentage of different heat removal modes for validation case 1, case 2, and case 3.

### 5.5 Graphical user interface (GUI) of the spreadsheet model

Microsoft Excel is used to develop the spreadsheet model of SNF cooling ponds at the Sellafield site. A GUI was developed for the spreadsheet model to ease the use of the model. A snapshot of the GUI is shown in Figure 5.8. The GUI allows the user to insert the operational configurations as well as the initial values. In addition, for more practicality, the GUI allows the user to specify the time period that the calculations are required to be performed over it.

The results are displayed within the GUI both numerically and graphically. The numerical results give the values of the computed output parameters at the end of the specified

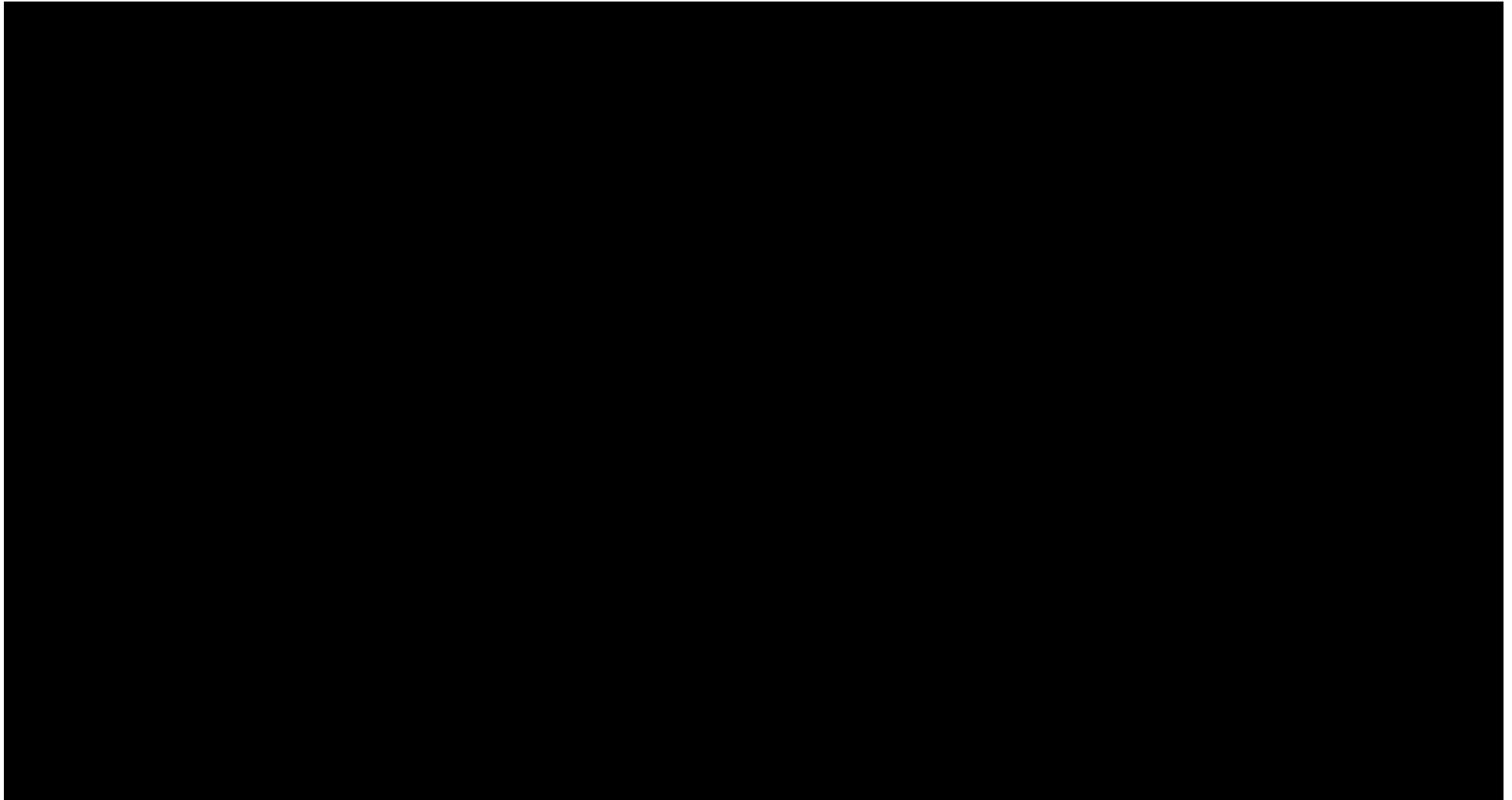
duration. The graphical results, on the other hand, are displayed in form of plot for the computed output parameters over the specified period.

Moreover, the GUI allows the user to control some of the heat transfer models by enable or disable them. These models are mainly at the water surface and walls of the pond hall. The models available at the water surface are evaporation, convection, and radiation. The heat transfer models available for walls of the pond halls are condensation on the walls, conduction and convection.

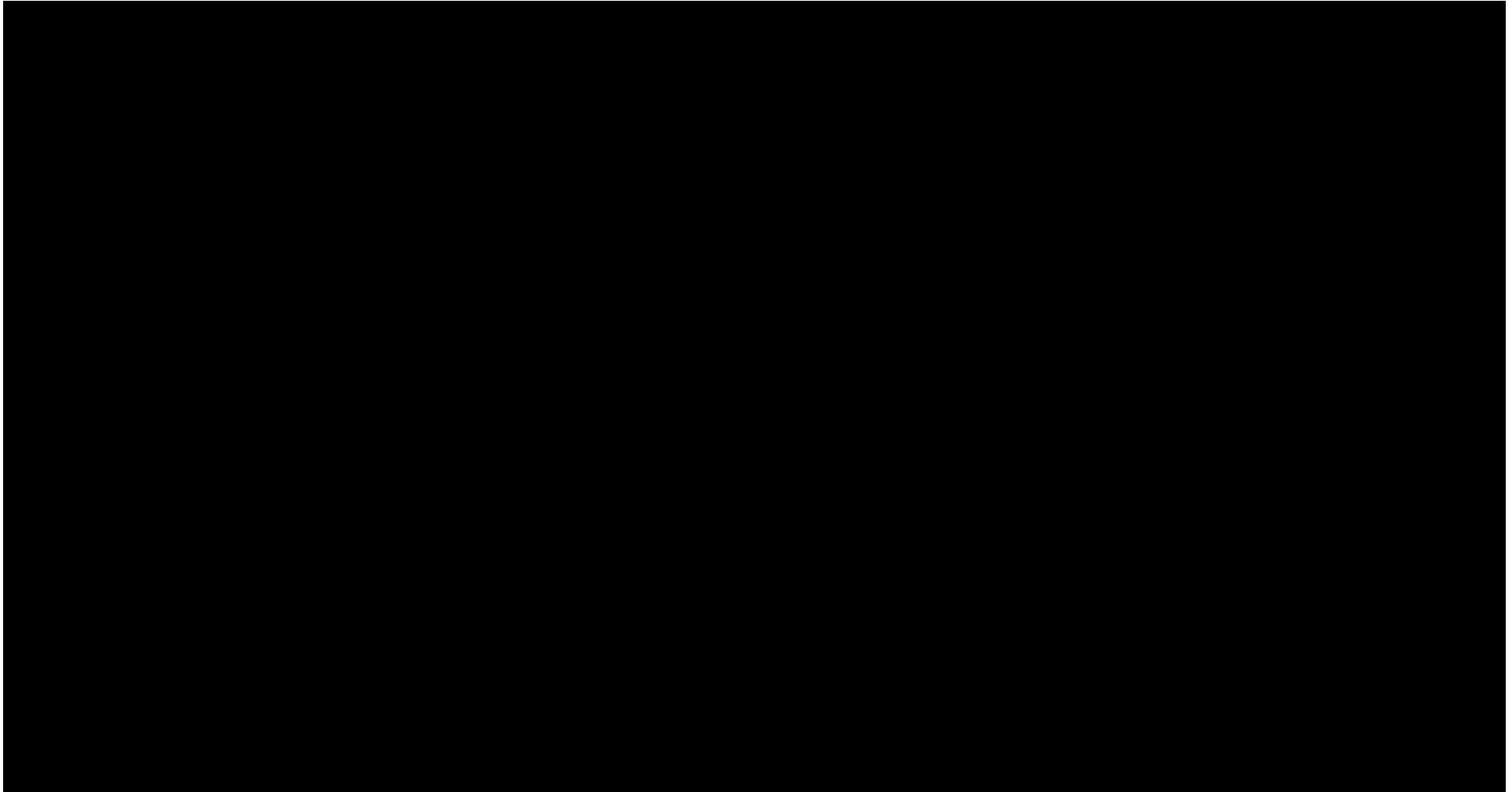
The reported output parameters are as follows:

- Temperature of the pond water (numerically and graphically)
- Pond water level (numerically and graphically)
- Temperature of the indoor air (numerically and graphically)
- Relative humidity of the indoor air (numerically)
- Evaporation rate at the steady-state (numerically)
- Flow rate of the water leaving the pond (numerically)
- If the cooling tower efficiency is used, the temperature drop in the cooling tower will be reported (graphically)
- If the steady-state creation is met it will be reported numerically

One of the advantages of using Microsoft Excel is that it allows reversed calculations to be conducted in order to predict some parameters according to a given limitations. For example, the value of heat load can be estimated according to the desired value of final water temperature. This can be achieved via the Goal Seek function which is available in Microsoft Excel. Moreover, the spreadsheet model is replicated with several Excel files and are connected together in series, which means that the outcomes from the first spreadsheet file will be the initial values for the next file and so on. The example shown in Figure 5.8 represents a loss of cooling case where the pond water starts to boil and its level is falling down. In order to examine the pond behaviour after recovering the cooling systems, another spreadsheet file is employed taking its initial values from the previous file as shown in Figure 5.9.







## **5.6 Summary**

In this chapter, a spreadsheet model of the cooling pond was developed based on the well-mixed hypothesis. This model takes into account majority of the heat transfer processes within the pond installation. The ventilation system was also included in this model. The reliability of the proposed model was validated against data reported in the literature for the Maine Yankee cooling pond as well as some measurements collected for the Sellafield site. It was confirmed from the validation exercises that the spreadsheet thermal model is able to predict the thermal behaviour of the cooling ponds within an acceptable level of accuracy under different operational scenarios and with various pond sizes. Also, the proportions of the heat removal components were quantified under three operating conditions for the Sellafield cooling pond.

The developed model is able to provide quick answers for “what-if” scenarios, which is required at the decision-making stage to aid the organisation in the operation of their cooling ponds more efficiently. In addition, the spreadsheet model will be used, in Chapter 8, to analyse the thermal performance of the spent fuel cooling ponds under normal operating conditions as well as accident scenarios using an appropriate statistical method.

# Chapter 6 Numerical Modelling of Sellafield SNF Cooling Pond

## 6.1 Introduction

As shown in the previous chapter that the analytical model is very a useful tool to provide an approximation of the main processes taking place within the pond structure. However, the analytical model was based on the well-mixed hypothesis, which assumes that the energies within pond installation have a homogenous distribution and hence cannot provide localised information about temperature and flow within the pond. For these reasons, a CFD model is required in order to get useful insights into the flow field and the fluid mixing within the SNF cooling pond. In addition, CFD can help to examine the validity of the well-mixed approach which is used in the present application. However, generation of a CFD model for the whole pond can be computationally demanding. This is due to the large size which is further complicated by physical phenomena such as evaporation and localised areas of turbulent motion.

In this chapter, a CFD model for the water body of the cooling pond was developed, where the analytical model was used to define the boundary condition at the free water surface. This model was validated against temperature data that were collected from the actual pond. This model was used to establish the temperature distribution across the water as well as to examine the effect of the fuel location and recirculation flow rate on the temperature distribution.

## 6.2 Modelling methodology

The modelling procedure can be split into three main steps: creating the geometry of the pond, generating an efficient mesh for the computational domain, and choosing the appropriate physical models and boundary conditions to mimic the existing physics. Each of the mentioned steps is described below.

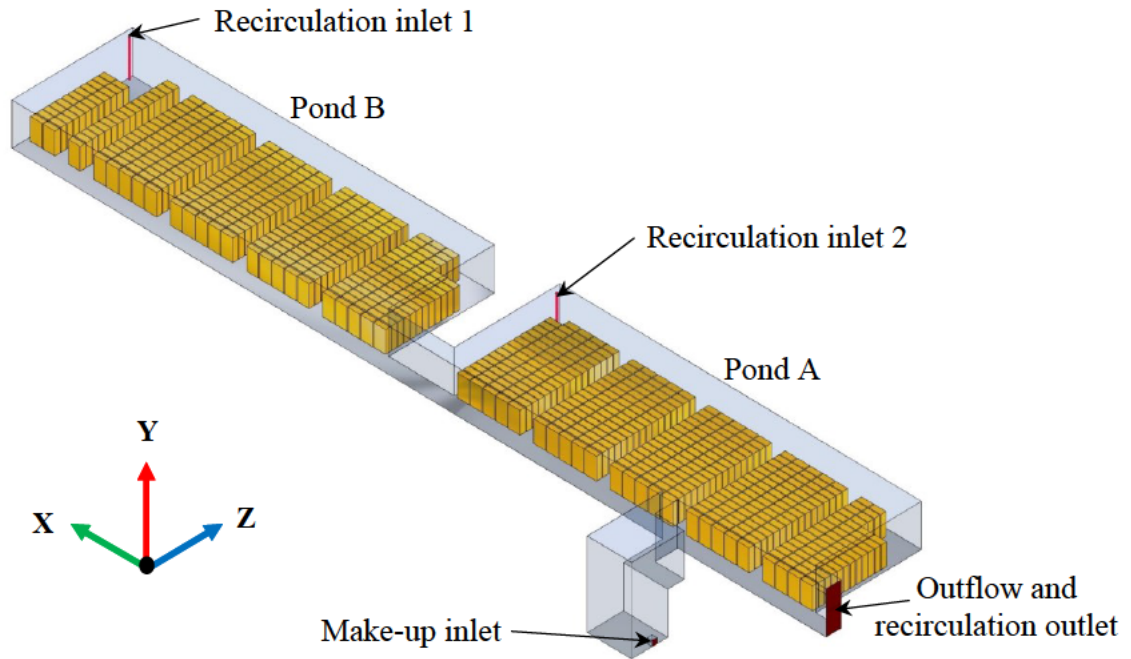


Figure 6.1: 3-D view of the computational domain for the Sellafield cooling pond.

### 6.2.1 Geometry of the pond

Three-dimensional geometry of the pond under investigation is shown in Figure 6.1. The main dimensions of the cooling pond are collected from technical drawings for the actual cooling pond, which was provided by Sellafield Ltd, as shown in Figure 6.2 and more detailed drawing is given in Appendix B. However, some assumptions and approximations were made to simplify the actual geometry. These simplifications are a very important step as it can affect the future computational expenses. These simplifications are listed below:

- Only the water body is considered in the CFD computational domain without considering the concrete wall as the proportion of the heat loss through these walls is insignificant.
- All the fuel assemblies are approximated by rectangular cuboid.
- The fuel rack assembly is assumed to be a porous medium to take into account the pressure drop within the assembly.

- Small curves are approximated to sharp edges to reduce the number of cells while generating the computational grid.
- Only two recirculation inlets are considered in the computational domain.



### 6.2.2 Generation of the computational grid

The number of cells within the computational grid is a very crucial factor that directly affects the calculation time. Great care was taken while generating the mesh to reduce the computational expenses without compromising the solution accuracy. However, the actual pond involved large dimensions and a large number of small gaps between the fuel assemblies rendering the meshing to be even more difficult. The computational domain was discretized by non-uniform structured hexahedral cells. The mesh is refined in places near to the walls, the inlets and around the fuel zones to capture the sharp gradients in these regions. An expansion ratio of 1.5 was used in the entire domain while a ratio of 1.2 was used at the fuel assemblies.

In order to examine the sensitivity of the mesh density, three different computational grids were generated with a different number of cells (1, 2.1 and 5 million). The computational grid with 2.1 million elements was found sufficient to capture the main flow gradient and a close-up view is shown in Figure 6.3.

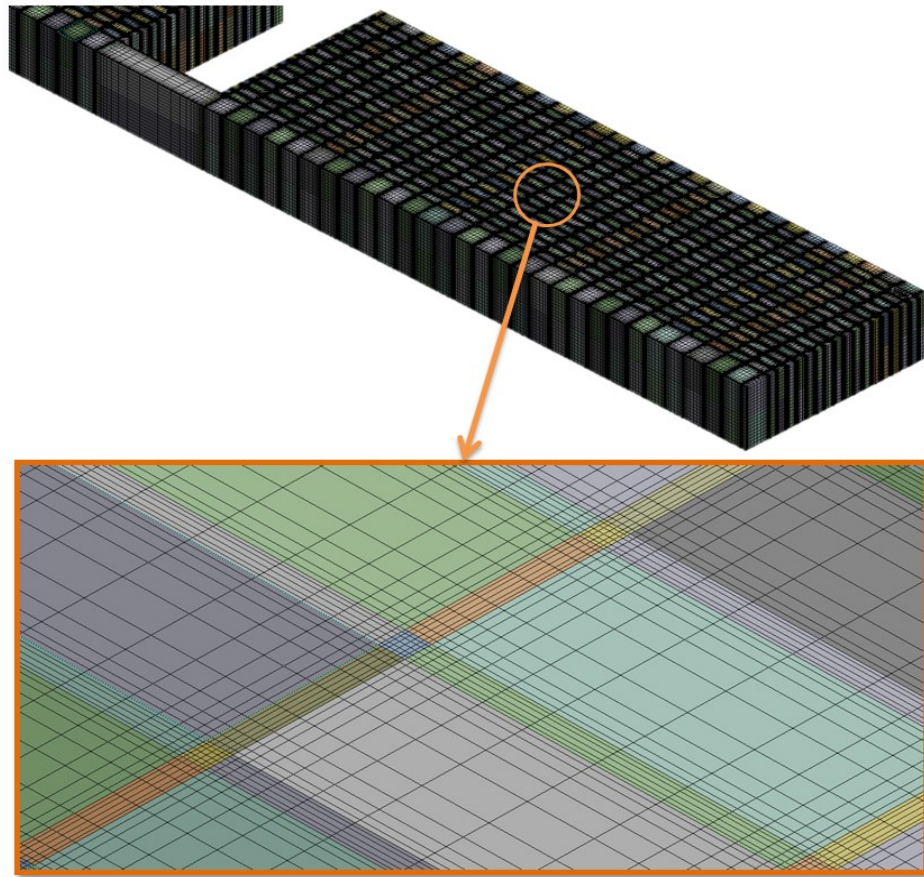


Figure 6.3: A close-up view of the mesh structure for the actual cooling pond.

### 6.2.3 Numerical model and boundary conditions

- The make-up water inlet is specified as a mass flow inlet boundary condition, which is supplied at a temperature similar to the outside environment.
- Outflow boundary condition was set at the outlet.
- A recirculation boundary condition with temperature drop is used to define the recirculation inlets and outlets.
- An adiabatic condition with no-slip wall was used on the pond floor and sidewalls.
- The water surface can be assumed as wall boundary condition with zero shear stress. This assumption neglects the wavy motion of the water surface; however, it is still a good approximation.



The heat loss from the free water surface is modelled in the same manner as described in Chapter 4. However, the effect of the ventilation system and the evaporated water on the volume of the humid air above the water surface were not considered. This issue was treated analytically in Chapter 5 by including the ventilation system. In the current chapter, the spreadsheet model is coupled with the CFD model. This coupling can be achieved by introducing the solution for the humid air zone from the spreadsheet model to the CFD model via a correlation for the overall heat transfer coefficient,  $h_{overall}$ , that can be applied at the water surface as shown in Figure 6.4. The used UDF is given in Appendix C.

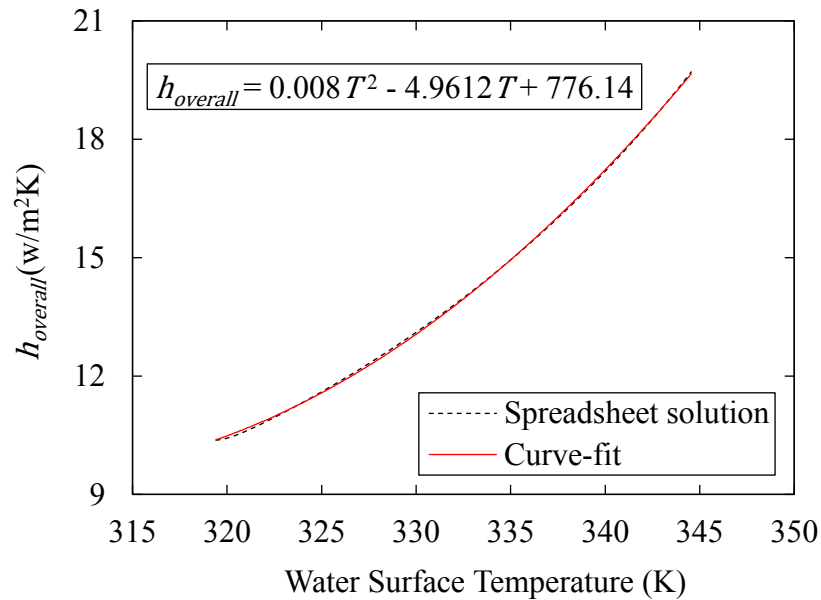


Figure 6.4: Overall heat transfer coefficient of the water surface as a function of the surface temperature.

The fuel assemblies are approximated to be porous medium zones where the decay heat is introduced as a volumetric energy source term. A source term as shown in Eq. (6.1) is added to the momentum equation Eq. (3.2) that included in the  $\vec{F}$  term in order to include the porosity.

$$S_i = -\left(\frac{\mu}{\Omega} v_i + C_2 \frac{1}{2} \rho |v| v_i\right) \quad (6.1)$$

where  $S_i$  is the porous media source term,  $v_i$  is the velocity in the  $i$ th directions ( $x$ ,  $y$  or  $z$ ),  $|v|$  is the velocity magnitude,  $\Omega$  is the permeability of the rack assembly and  $C_2$  is the inertial resistance factor of the rack assembly and can be calculated from:

$$\Omega = \frac{A_{act}}{A_R} \left( \frac{d_h^2}{32} \right) \quad (6.2)$$

where  $A_{act}$  is the actual flow area,  $A_R$  the rack cross sectional area and  $d_h$  is the hydraulic diameter of the rack assembly and calculated as:

$$d_h = \frac{4A_{act}}{\text{wetted perimeter of the cross section}} \quad (6.3)$$

The inertia resistance factor can be expressed as:

$$C_2 = \frac{\sum K_l}{\text{flow length}} \quad (6.4)$$

where  $K_l$  is the contraction and expansion loss coefficient which has a value of 1.

Buoyancy forces were also considered in the calculation by including the gravity force in the momentum equation as well as selecting the appropriate water properties as described before in Table 4.1.

The flow regime within the cooling pond is more likely to be laminar. However, in some regions near to the fuel assemblies, the Rayleigh number could be high enough ( $\sim 10^{15}$ ) to produce turbulent flow. In addition, the regions near to the make-up water supply and the recirculation inlets could also experience a turbulent generation especially when the maximum recirculation flow rate is used. In order to include the turbulent effects, the  $k$ - $\epsilon$  turbulence model was incorporated.

Pressure-velocity coupling is achieved using PRESTO algorithm with second-order upwind spatial discretization. The solution is considered numerically converged when the residuals are typically three orders of magnitude compared to the values at the start.

Several time step sizes were used to examine its effect on the water temperature. The temperature at the outlet was selected as the monitoring parameter as shown in Table 6.1. It was found that using time step lower than 3 sec has led to satisfactory results.

Table 6.1: Comparison between different time step sizes.

Time step (sec)	Outlet temperature (°C)
0.5	72.92
1.5	72.98
3	73.01
5	74.32
10	78.29

Series of transient CFD simulations were conducted for different operational configurations using the commercial CFD package of ANSYS Fluent 16.0. All of the simulations were conducted on i7- 3770 CPU with 3.40 GHz 8 cores machine and the typical run time for different grid sizes is illustrated in Table 6.2. In the following sections, the operational configurations used in the simulations might vary. For this reason, the configuration of each simulation will be given subsequently in each section.

Table 6.2: comparison between different mesh sizes.

Mesh density (cell)	Computational time (day)	Number of iterations	Outlet temperature (°C)
1 M	3	80,000	75
2.1 M	5.5	105,000	73
5 M	8	147,000	72.9

### 6.3 Model validation and verification

In order to examine the reliability of the used modelling methodology, a validation exercise was conducted. The validation procedure involved two stages: the first stage is to compare the water temperature obtained from the CFD model with the measured

temperature. The cases used to validate the spreadsheet model in Chapter 5 are also used to verify the CFD model of the cooling pond. This would validate the numerical model at the steady state conditions. In the second stage of the validation exercise, however, the transient behaviour of the numerical model is scrutinised by comparing the rate of change in the temperature with the spreadsheet model over a period of time. The configurations used in this calculations are listed in Table 6.3.

Table 6.3: Parameters used in the transient calculations of the validation exercise.

Parameter	Value
Heat load (MW)	10
Outside environment temperature (°C)	15
Recirculation flow rate (kg/s)	57.9
Temperature drop in cooling tower (°C)	10
Make-up rate (kg/s)	13.9
Make-up temperature (°C)	15
Ventilation inlet rate (m <sup>3</sup> /s)	12

Figure 6.5 shows the comparisons between the measured water temperature and the CFD results. It can be clearly seen from the figure that the CFD results agreed well with the measurements. In addition, the temperature predicted by the CFD is always larger than the spreadsheet and measured temperatures, except in case 1. This could be due to the high recirculation flow rate, which increases the motion of the bulk flow and in turn enhances the heat transfer at the water surface.

A comparison of water temperature evolution between CFD and spreadsheet predictions is shown in Figure 6.6. Up to day 8, an excellent agreement can be observed between both approaches. After that, the results start to deviate by a maximum of 0.5 °C higher for the CFD predictions. The reason is that in the CFD model the buoyancy effect causes stratification of the water temperature resulting in a relatively lower temperature at the surface than the bulk fluid. In the spreadsheet model, on the other hand, the buoyancy force is not included and the water temperature is assumed uniform across the pond structure. However, the results are still within a good level of accuracy. This also confirms the validity of the well-mixed approach that was used in producing the spreadsheet model.

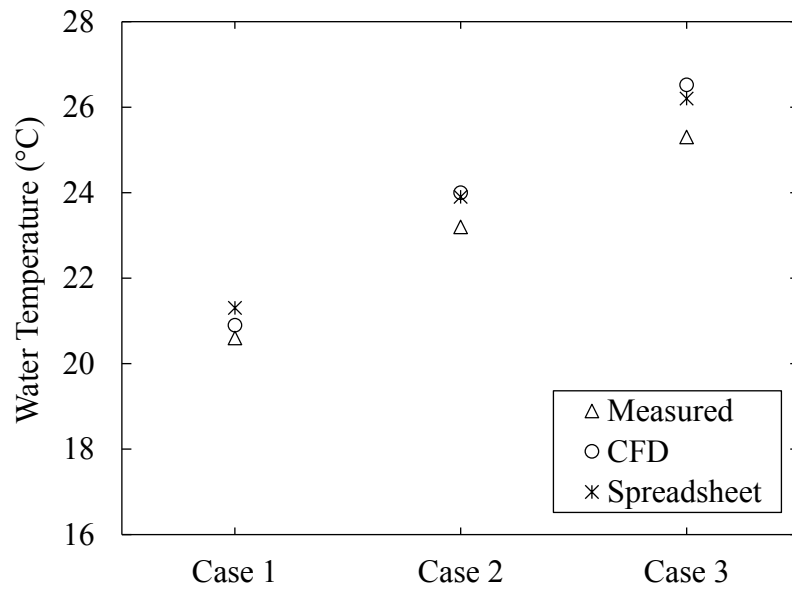


Figure 6.5: Volume average pond water temperature at steady state.

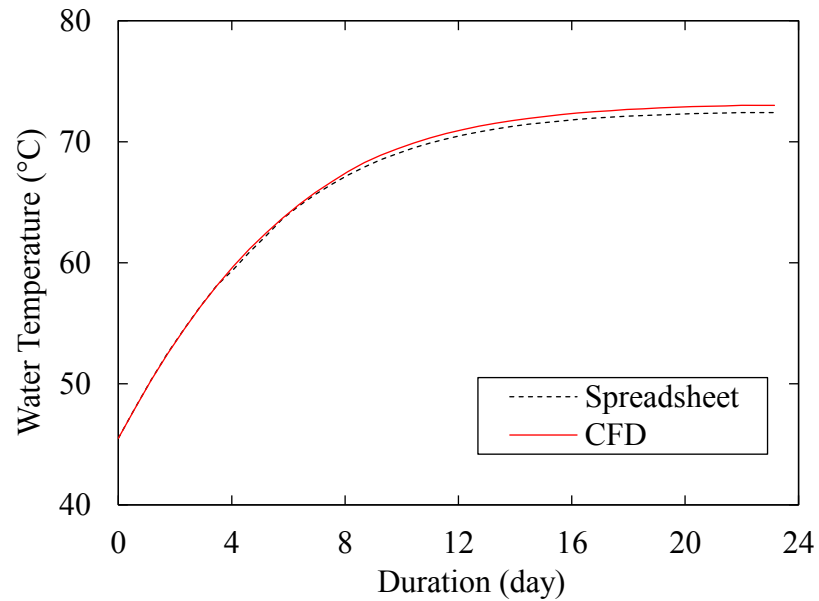


Figure 6.6: Increase of average pond water temperature.

#### 6.4 CFD results and discussion

In this section, the input parameters used in the simulations are the same as in those used in the validation section. The outcomes of these simulations are presented in terms of flow field and temperature profiles. Also, the results are displayed on selected planes at different locations and directions as shown in Figure 6.7.

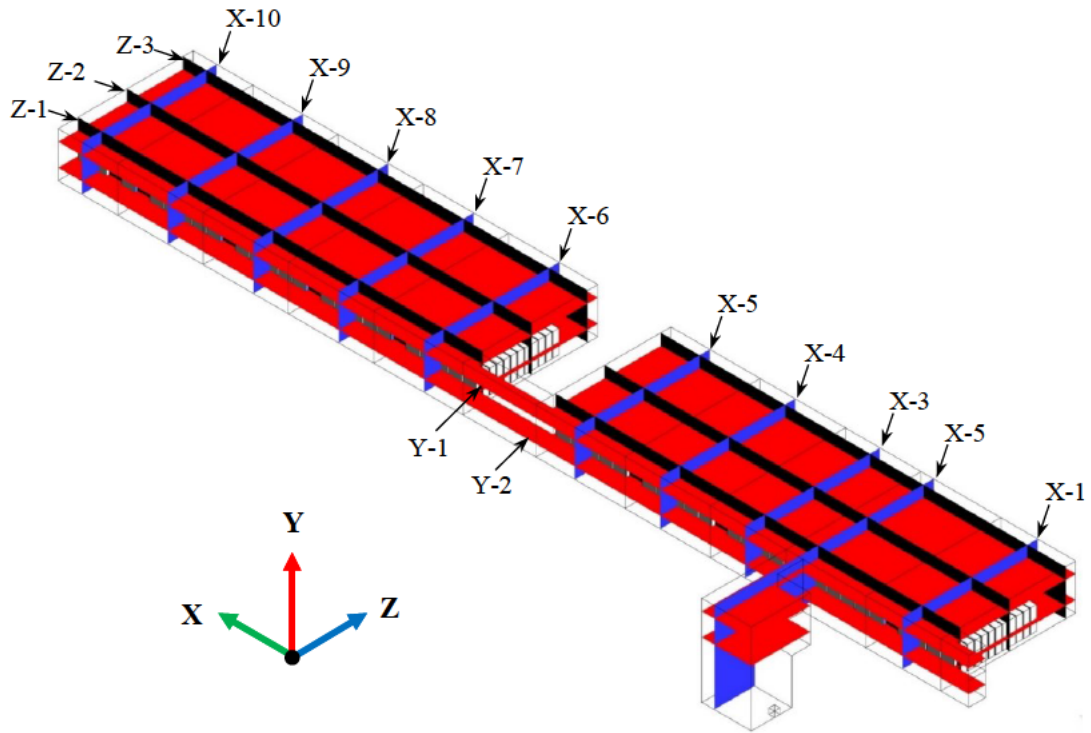


Figure 6.7: Breakdown of planes used to display CFD results.

#### 6.4.1 Flow field and streamlines

Three-dimensional streamlines are shown in Figure 6.8. It can be clearly seen that the velocity magnitudes tend to be very low ranging between 0 m/s to about 0.01 m/s. This observation could be because of low decay heat released from the fuel assemblies. The streamlines clearly show the helical motion of water rising in the inlet pond. Moreover, high velocities can be observed in the inlet pond especially near to the surface. It is also evident that some regions within the cooling pond (in particular Pond B) have rather stagnating regions, which may be due to the location of the recirculation inlet.

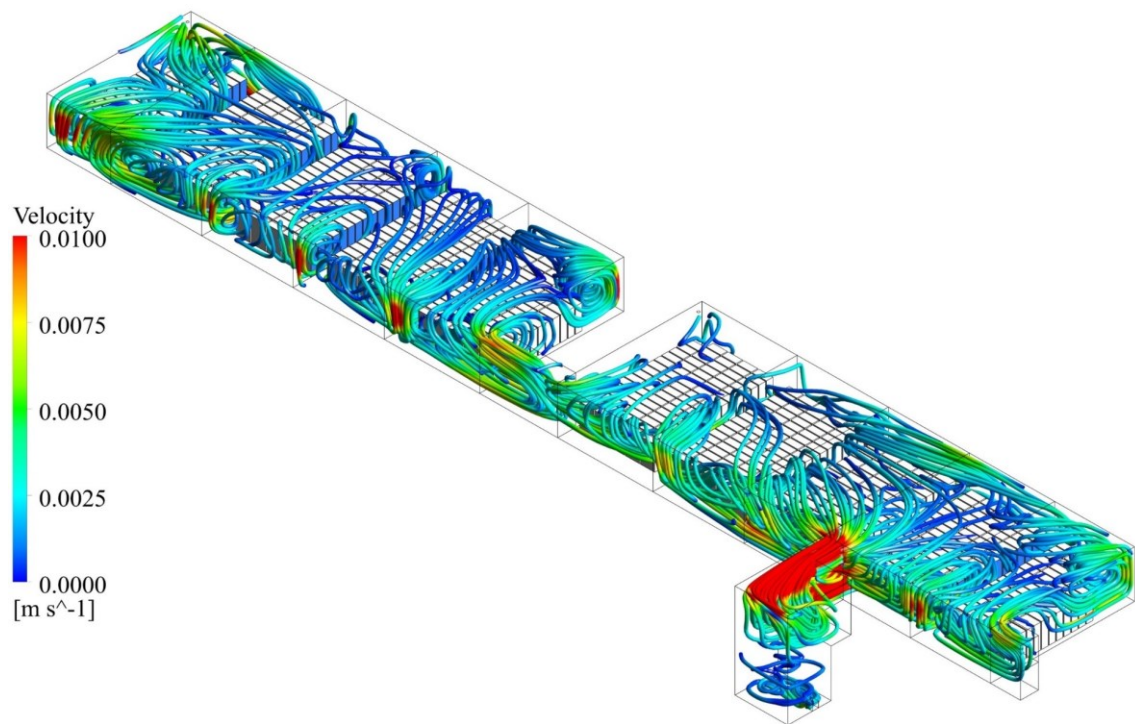


Figure 6.8: Streamlines coloured by velocity magnitudes.

Figures 6.9 and 6.10 show the velocity magnitudes and vector fields on various chosen planes. It might be useful to note that the vectors shown in the velocity results are just indicative of the flow direction only and they are highly exaggerated in size for better visualisation. Figure 6.9 indicates that the flow is more active in the regions near to the water surface and in the channels surrounding each group of the fuel assemblies. Furthermore, relatively high velocities can be seen in the channel section between Pond A and Pond B and the regions in proximity to walls surrounding the cooling pond. On the other hand, the flow in the zones between the fuel assemblies is very weak and in some locations is almost stagnant. Between the fuel assemblies, vertical motion due to the buoyancy force can be observed as shown in Figure 6.10.

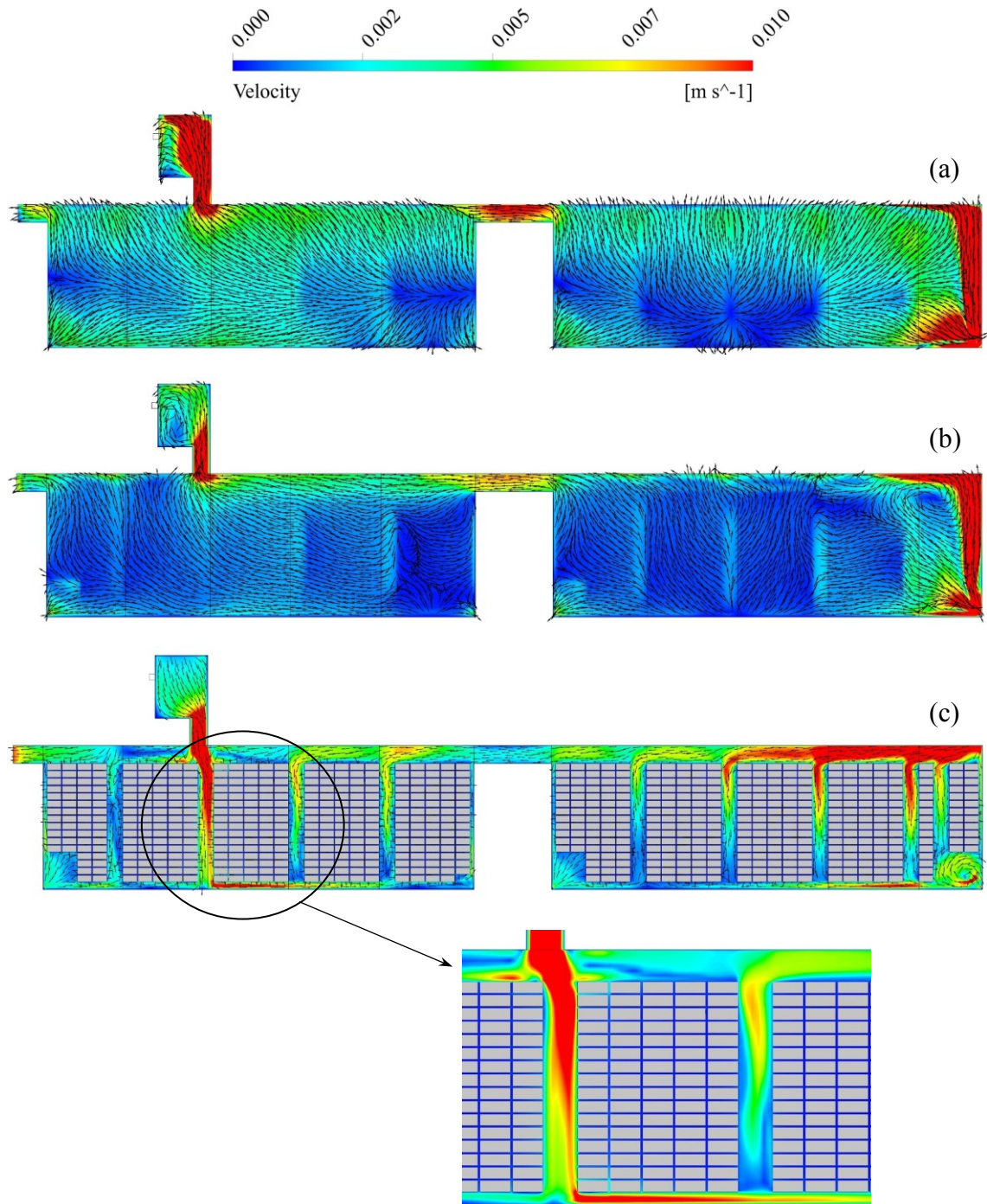


Figure 6.9: Velocity contours on chosen planes (a) at the water top surface, (b) on Y-1 plane and (c) on Y-2 plane.



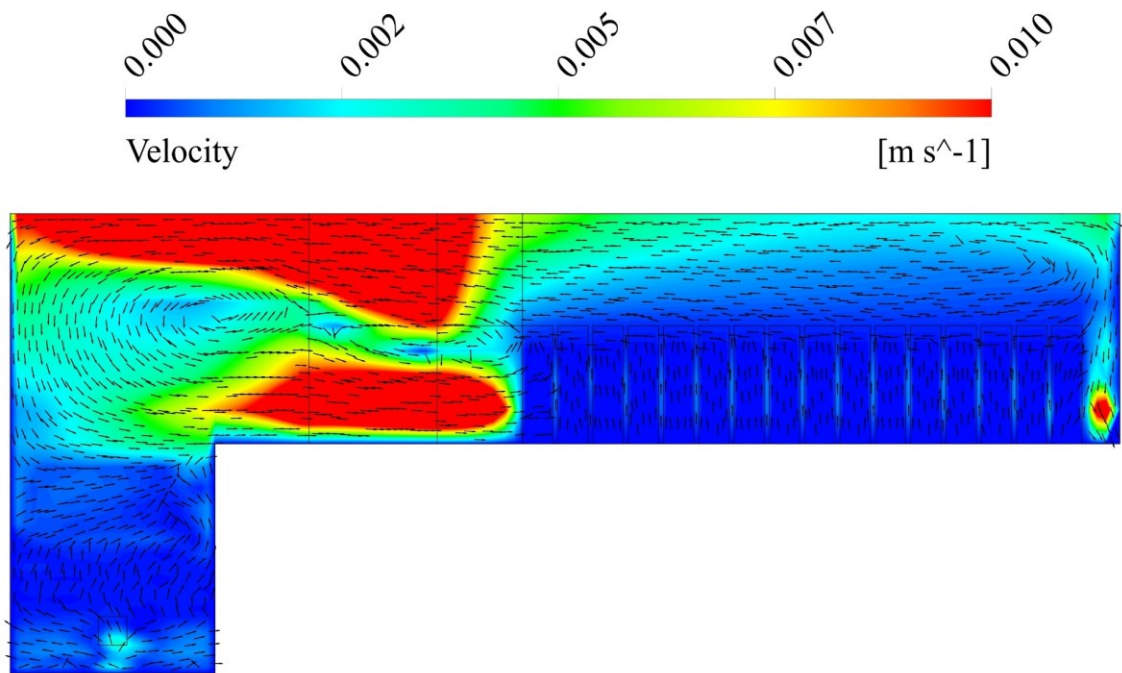


Figure 6.10: Velocity contours on X-2 plane at the inlet pond.

#### 6.4.2 Temperature profiles

Detailed temperature profiles were obtained on several planes and are presented in Figures 6.11 to 6.13. The temperature distribution in the horizontal direction is almost uniform across the cooling pond with less than  $0.3\text{ }^{\circ}\text{C}$  variation, except in some locations near to the make-up water inlet and recirculation inlet due to the effect of proximity to these locations. In the vertical direction, temperature stratification is not significant as evidenced in Figure 6.12. The average temperature of the pond water is approximately  $20.5\text{ }^{\circ}\text{C}$  whereas the water temperature at the free surface is slightly lower than the bulk, about  $20.23\text{ }^{\circ}\text{C}$ . This observation is in line with other work on evaporation such as Bower et al. [82]. This is due to the direct contact with the ambient air. A careful look at Figure 6.13 shows low temperature in the inlet pond. It is also visible that there is a very small vertical temperature gradient between the fuel rods.

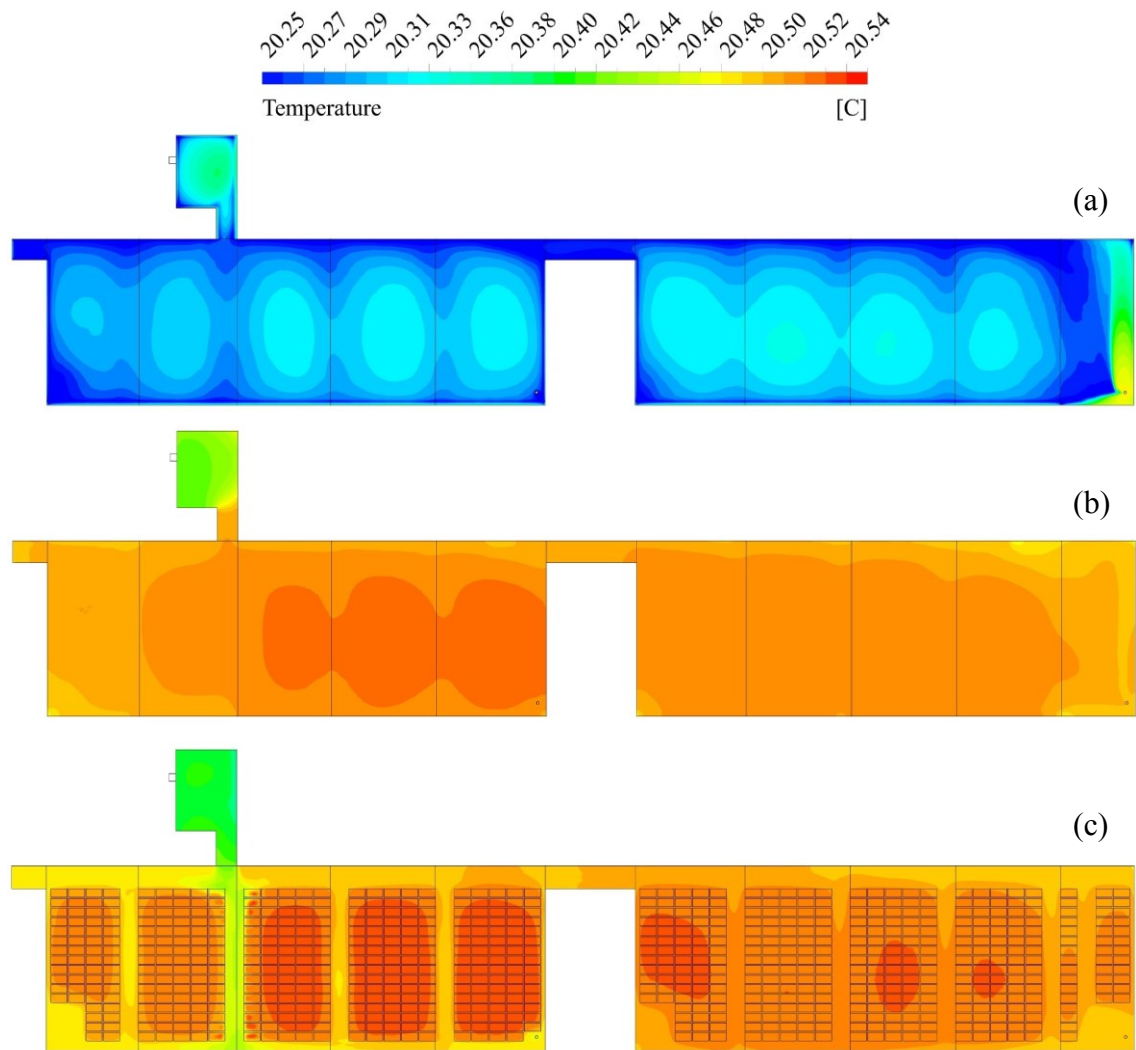


Figure 6.11: Temperature profiles on chosen planes (a) at the water top surface, (b) on Y-1 plane and (c) on Y-2 plane.

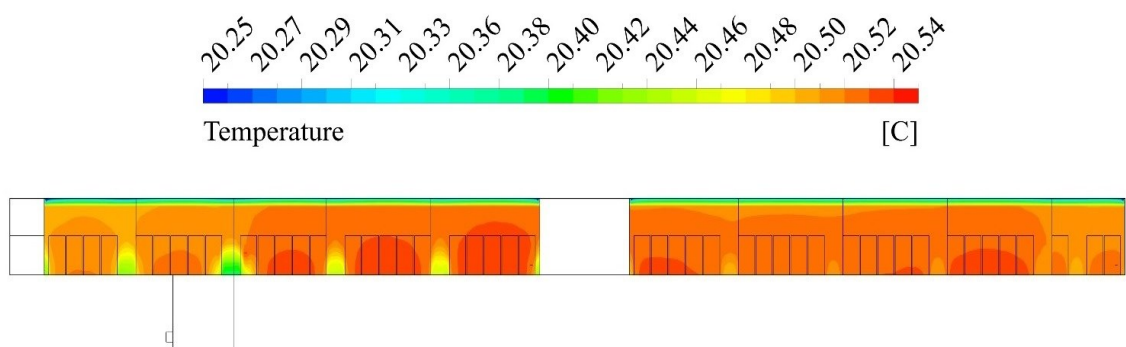


Figure 6.12: Temperature profiles on Z-2 plane.

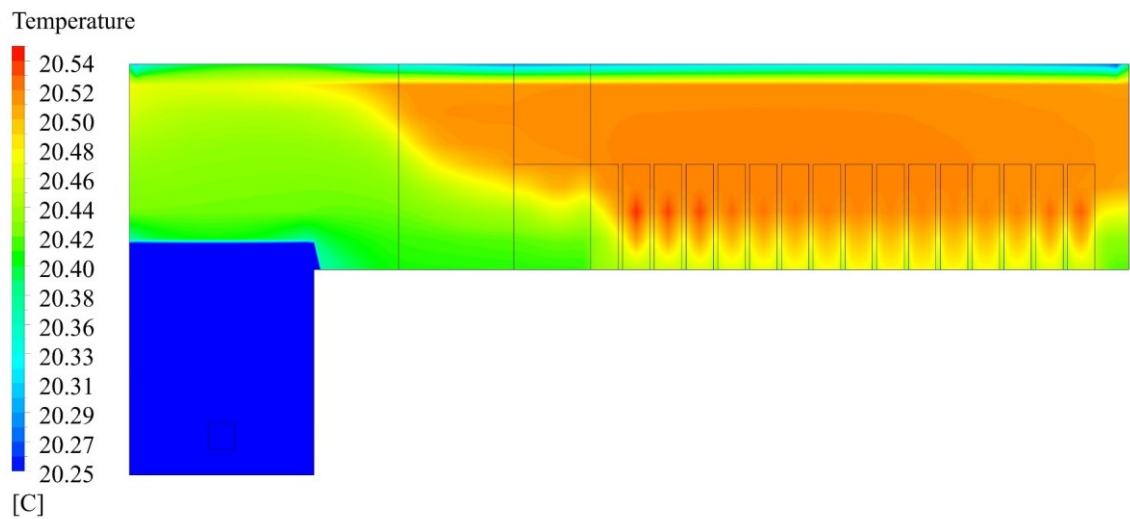


Figure 6.13: Temperature profiles on X-2 plane at the inlet pond.

Figure 6.14 shows the distribution of the heat loss from the free water surface. It is clear that the heat loss is not equal across the water surface. Above the fuel assemblies, the heat loss is higher than any other location within Ponds A and B. This is corresponding to the non-uniform distribution of the water surface temperature as a result of the concentration of the heat load in these regions.

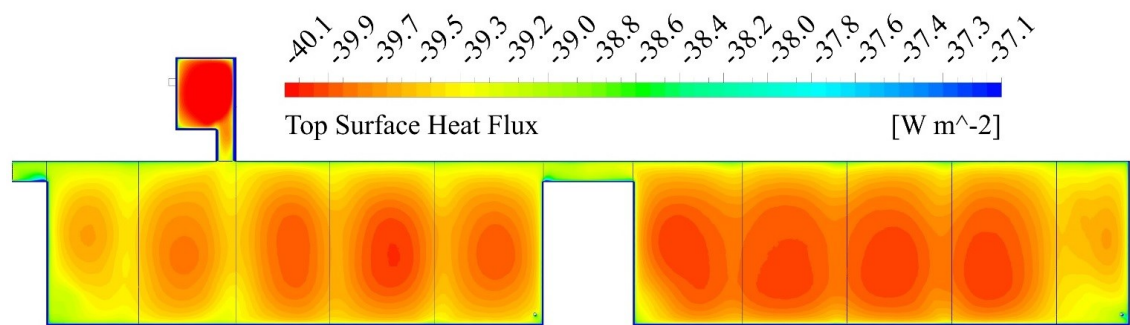


Figure 6.14: Heat loss from the water top surface.

## 6.5 Effect of recirculation and heat load distribution

[REDACTED]

[REDACTED]

[REDACTED]

[REDACTED]

In the previous sections, the heat load was assumed uniformly distributed over the available fuel assemblies across the entire cooling pond. However, concentrating of the heat load in one pond can have an impact on the distribution of water temperature. In addition, recirculation may also have an effect on the uniformity of the water temperature.

When the pond was loaded with low heat load, the temperature variation was insignificant as shown in Figure 6.11, except regions near to the inlet pond. However, large temperature variations are most likely to occur when the pond is loaded with the maximum heat load. In addition, if the make-up water is supplied at a high rate, this would lead to higher variation.

In order to assess the influence of the above mentioned factors on the uniformity of the water temperature, series of simulations are conducted under different configurations. The test cases are highlighted in Table 6.4. With the purpose to achieve measurable temperature variation, the pond is loaded with a heat load of 10 MW to provide a high intensity of temperature localisation. Also, the make-up water used in this analysis is supplied at rates of 57.5 and 115 kg/sec with no temperature drop, which are much higher than the maximum allowable rate in the actual pond. Moreover, three different layouts of heat load distribution are considered during this analysis. The first layout is when the heat load is uniformly distributed over all the available fuel assemblies in Pond A and B. The second and third layout is when the heat load is concentrated in Pond A and Pond B respectively. During the simulations, no temperature drop in the cooling tower was considered.

Table 6.4: Parameters used in the study of the effect of recirculation and heat load distribution on the uniformity of water temperature for a heat load of 10 MW.

Run	Make-up rate (kg/s)	Pond	Recirculation (kg/sec)
1	57.5	Both	Off
2	57.5	Both	115
3	57.5	Both	230
4	57.5	A	Off
5	57.5	A	115
6	57.5	A	230
7	57.5	B	Off
8	57.5	B	115
9	57.5	B	230
10	115	Both	Off
11	115	Both	115
12	115	Both	230
13	115	A	Off
14	115	A	115
15	115	A	230
16	115	B	Off
17	115	B	115
18	115	B	230

A total of 18 simulations were conducted for the test cases as shown in Table 6.4. The cooling pond was divided into 11 section as shown in Figure 6.15. The results of these simulations are obtained in terms of volume average temperature in each section. Each section contains a group of fuel assemblies, which can be seen in Figure 6.2.

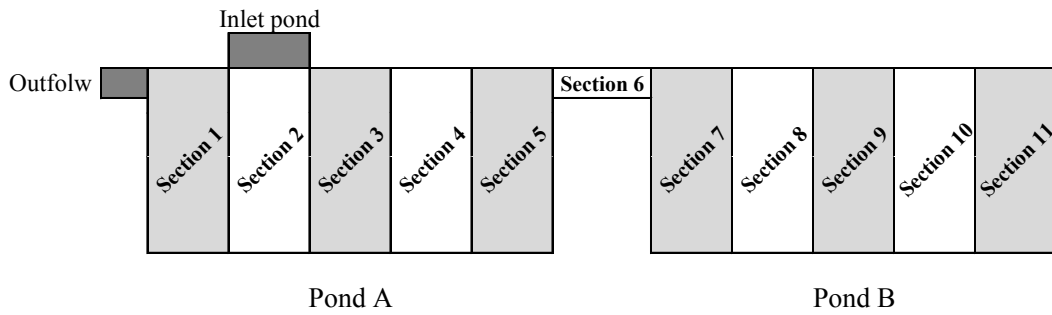


Figure 6.15: Breakdown of pond sections.

Distribution of water temperature for the test cases with make-up water rate of 57.5 kg/s is shown in Figure 6.16 while the cases with make-up water of 115 kg/sec are shown Figure 6.17. However, the results in these figures represent only the volume average temperature and not the localised values. In addition, these results are only limited to the 11 sections shown in Figure 6.15 and do not include the inlet pond region.

It can be seen in both figures that that maximum uniformity of water temperature is achieved when the heat load is uniformly distributed over the fuel assemblies in both ponds as illustrated in Figures 6.16 (a) and 6.17 (a). In this layout, however, the average temperature of Pond B is slightly higher than Pond A where the maximum recorded variation is less than 0.5 °C. When the fuel is located in Pond A only as shown in Figures 6.16 (b) and 6.17 (b), higher average temperatures are observed in Pond A with same maximum variations as in the previous layout. In both layouts, the channel connecting both ponds (section 6) always has an average temperature lower than both ponds because there is no fuel stored in this region.

The last layout considered in this analysis is when all of the fuel assemblies are located in Pond B only as presented in Figures 6.16 (c) and 6.17 (c). In this layout, the highest temperature variations were recorded, amongst all the layouts, with a maximum variation of just less than 0.9 °C. Usually, in three layouts, section 1 has the lowest average temperature in Pond A while in Pond B section 11 is always the lowest. This is attributable to the less number of fuel assemblies located in these sections and the proximity of section 1 to the inlet pond where the make-up water is supplied.

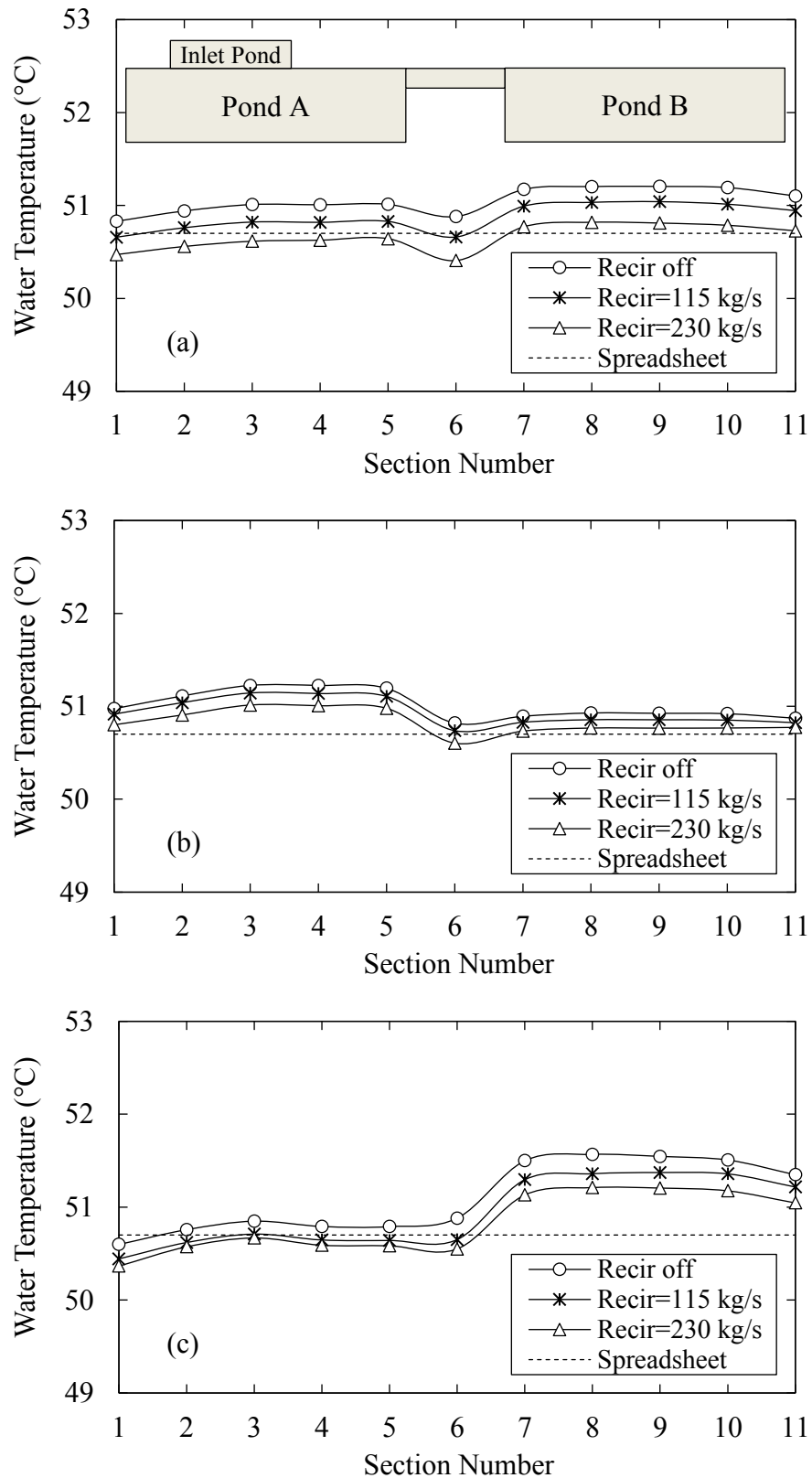


Figure 6.16: CFD temperature distribution for make-up flow rate of 57.5 kg/s under different recirculation and fuel locations: (a) both ponds, (b) Pond A, and (c) Pond B.

The effect of the recirculation can be also seen in Figures 6.16 and 6.17. Turning on the recirculation without temperature drop in the cooling tower can reduce the average temperature in the considered layout. However, this reduction is relatively small which is around 0.5 °C. This is because of the enhanced flow activity at the water surface due to the recirculation. In terms of water temperature uniformity, the introduction of recirculation does not seem to enhance the temperature uniformity except in the last layout where the heat load is concentrated in Pond B.

Generally, from the results shown in Figures 6.16 and 6.17, it can be concluded that the variation between the average temperatures in the presented sections is not very significant but this may be limited to the considered configurations. Furthermore, the recirculation without temperature drop in the cooling tower does not have a significant impact on the water average temperature. Also, the same figures reveal that the predictions of the spreadsheet model represent a good approximation of the water average temperature and confirm the validity of using the well-mixed approach.



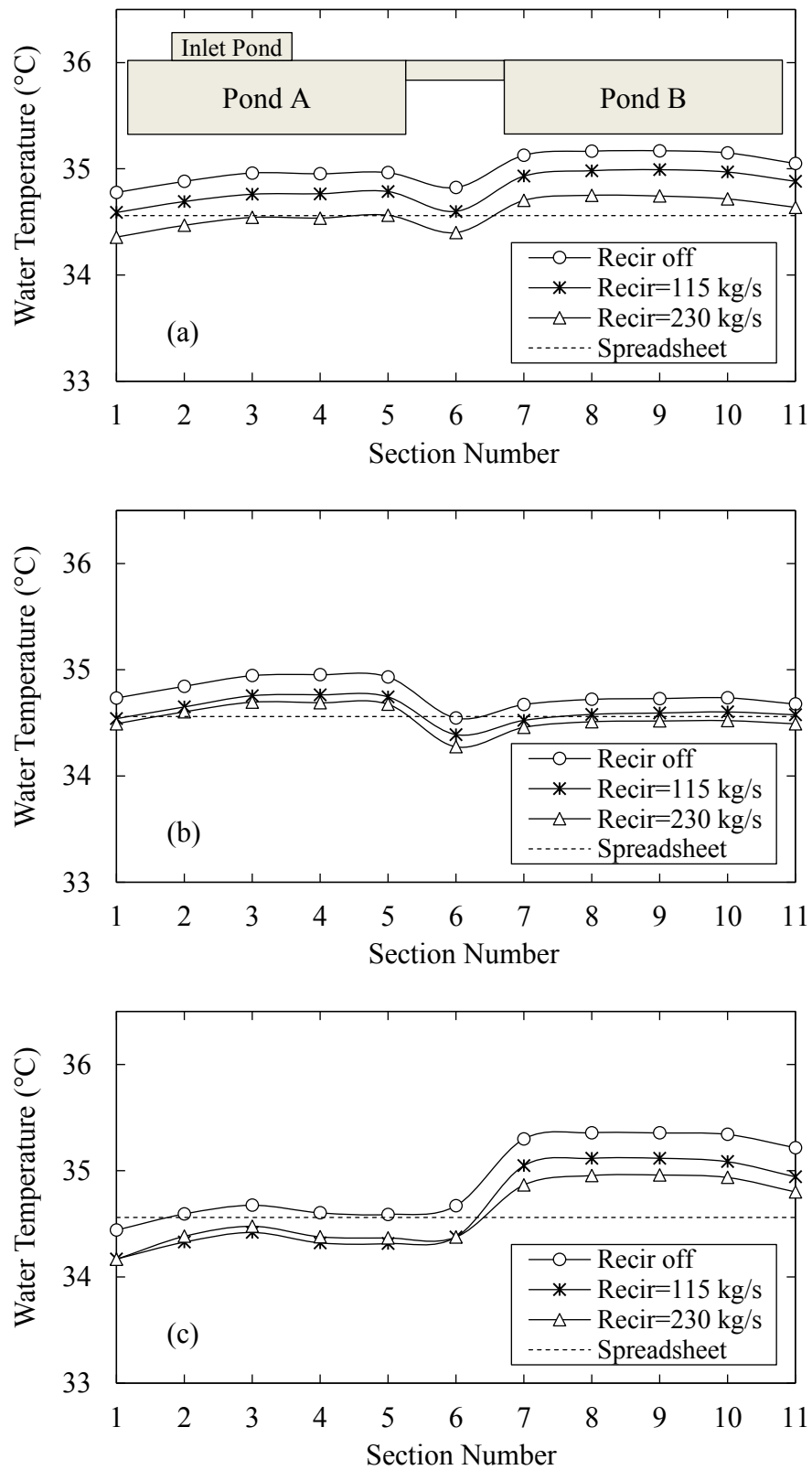


Figure 6.17: CFD temperature distribution for make-up flow rate of 115 kg/s under different recirculation and fuel locations: (a) both ponds, (b) Pond A, and (c) Pond B.

The maximum localised temperature within Ponds A and B are obtained and summarised in Tables 6.5 and 6.6 for the 18 test cases. In the same tables, the volume average temperatures for the cooling pond including the inlet pond are shown. In the first two layouts, for all recirculation conditions, the peak temperature is found in Pond A, where the difference between peak and average values is around 3 °C. When the heat load is concentrated in Pond B, the peak temperature is recorded in the same pond where the difference between peak and average values is slightly higher than the other layouts.

The global value of the minimum temperature, for the test cases with make-up flow rate of 57.5 kg/s, is about 27.6 °C. While in the cases with make-up flow rate of 115 kg/s the value of the minimum temperature is about 41.8 °C. However, these values do not vary much between the considered test cases. In addition, these values were mostly found in section 2 due to the proximity from the inlet pond.

Table 6.5: Summary of water temperature for test cases with a make-up flow rate of 57.5 kg/s.

Location of heat load	Recirculation (kg/sec)	Maximum temperature (°C)		Average temperature (°C)
		Pond A	Pond B	
Both	Off	52.8	52.3	50.2
	115	53.0	52.4	50.1
	230	53.1	52.2	49.9
Pond A	Off	53.7	51.6	50.2
	115	53.8	51.5	50.1
	230	53.4	51.5	50.0
Pond B	Off	52.0	53.2	50.3
	115	51.9	53.7	50.2
	230	51.8	53.7	50.0

Table 6.6: Summary of water temperature for test cases with a make-up flow rate of 115 kg/s.

Location of heat load	Recirculation (kg/sec)	Maximum temperature (°C)		Average temperature (°C)
		Pond A	Pond B	
Both	Off	36.8	36.3	34.5
	115	37.2	36.7	34.3
	230	37.0	36.5	34.1
Pond A	Off	37.7	35.5	34.4
	115	37.5	35.3	34.1
	230	37.4	35.3	34.1
Pond B	Off	35.8	36.9	34.5
	115	36.0	37.8	34.6
	230	35.6	37.9	34.1

## 6.6 Summary

A CFD model was developed for Sellafield's cooling pond considering the water zone only. The effect of the humid air zone and the ventilation system were introduced to the model in terms of heat transfer coefficient at the water surface which was obtained from the spreadsheet model. The fuel assemblies were approximated to porous medium with a volumetric heat source. The CFD model was validated against temperature measurements that were collected from the site. Moreover, the transient predictions of the numerical model were verified by comparing the rate of temperature increase with its counterpart from the spreadsheet model. From the validation exercises, good agreements were observed. Furthermore, the validity of well-mixed hypothesis to be adopted in such application was confirmed.

The CFD results revealed that the velocity magnitudes within the water body are very small except the regions near to the inlet pond and the recirculation inlet. In a similar manner, the temperature distribution shows small variations. To examine the effect of the

recirculation and the heat load distribution, a parametric study was conducted. This study showed that the temperature uniformity is not very sensitive to the recirculation where a relatively higher sensitivity to the heat load distribution was observed. The maximum recorded temperature difference between the average and peak values was about 3.8 °C, only under the presented conditions. The minimum localised temperature was always found in pond section 2 due to its proximity to the make-up supply.

# Chapter 7      Micro-Level Numerical Analysis of the Cooling Pond

## 7.1 Introduction

The fuel rack arrangement can be described as a cluster of vertical cylinders containing the spent fuel. Generally, there are several types of the fuel assemblies that been designed for specific purposes. However, due to safety regulation issues, Sellafield Ltd. proposed a new rack design where each of the fuel rods is contained by a square cross section rack fabrication as shown in Figure 7.1. A grid spacer is allocated between the racks to support the racks and maintain the distance between them. A rectangular lid with two holes is placed on top of the racks.

This chapter discusses the micro-level analysis of the cooling pond that is represented by detailed modelling of the fuel assemblies, which was approximated to porous medium in the previous macro model of the pond. In order to achieve that, establishing a methodology for modelling submerged vertical cylinders will allow a clearer understanding of the flow behaviour in such situations. In addition, it will partially validate the modelling methodology of the rack arrangement. The experiment conducted by Kimura et al. [103] was selected for the purpose of validation. This experiment was selected for few reasons as listed below.

- Water is the heat transfer medium.
- The vertical position and shape of the cylinder.
- The cylinder is heated with a uniform heat flux, which is similar to the condition in the rack arrangement.
- Involves flow transition from laminar to turbulent.
- Allows examining the curvature effect on the heat transfer characteristics numerically.

- Top surface of water is exposed to the atmosphere to allow evaporation to take place.

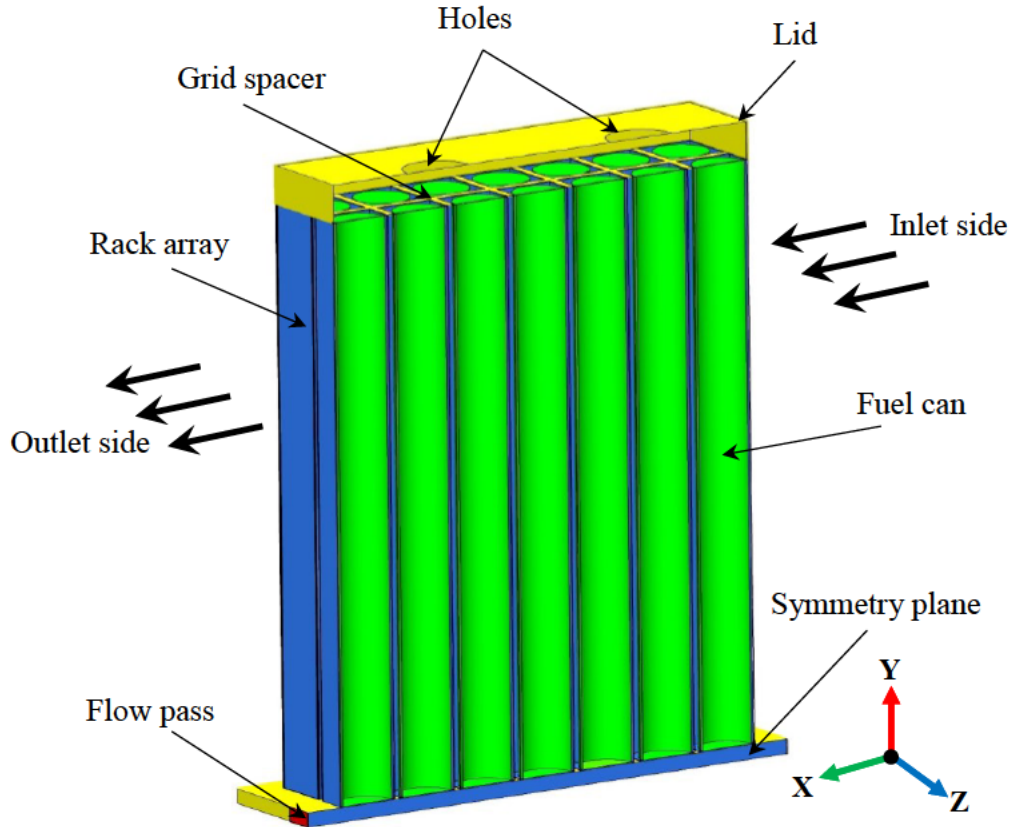


Figure 7.1: Half geometry of the fuel rack assembly.

## 7.2 Modelling of fluid flow and heat transfer around vertical cylinders

### 7.2.1 Modelling methodology

A sketch of the experimental setup for Kimura et al. [103] is shown in Figure 7.2. The cylinder is heated with a constant heat flux of  $5000 \text{ W/m}^2$  and the water was initially at the ambient temperature of  $22^\circ\text{C}$ . The water free surface is exposed to the ambient air. Due to the symmetry of computational domain, only one-quarter of the geometry is considered. The heat transfer from the free water surface is treated in the same manner as described in Chapter 4.

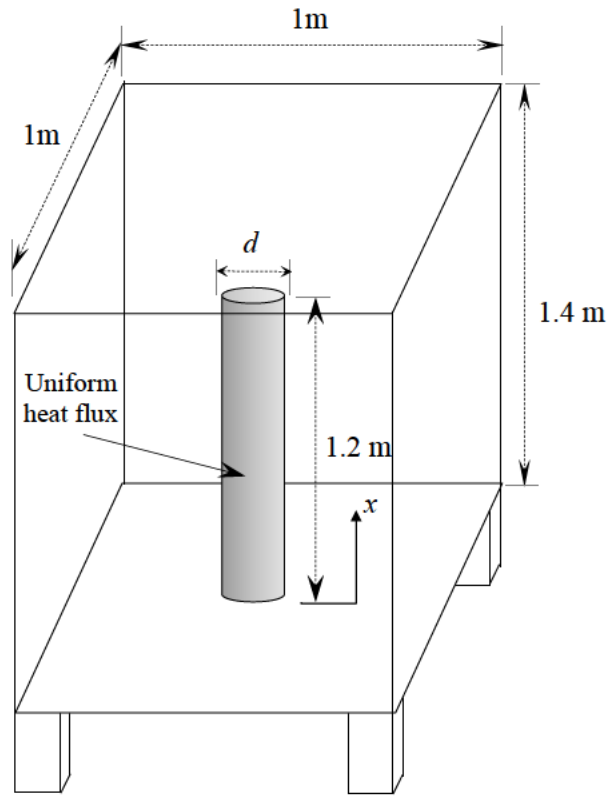


Figure 7.2: Sketch of the experimental apparatus used by Kimura et al. [103].

The problem involved flow transition from laminar to turbulent within the boundary layer as the maximum modified Rayleigh number, based on the cylinder length, reached a magnitude of the order of  $10^{14}$ . However, to capture the transition region,  $y^+$  at the cylinder surface is kept within the recommended range, 0.001 to unity, during the simulation [17]. Furthermore, the simulations were conducted for three cylinders with different diameters, 10, 26 and 165 mm. The mesh is generated with approximately 380,000 cells and is shown in Figure 7.3. The physical properties of water were considered to be temperature dependent and were evaluated by using Eq. (4.14).

The results obtained from the simulations were processed and displayed in the form of surface temperature, heat transfer coefficient along the cylinder surface, and  $Nu_x$  vs.  $Ra_x^*$ .

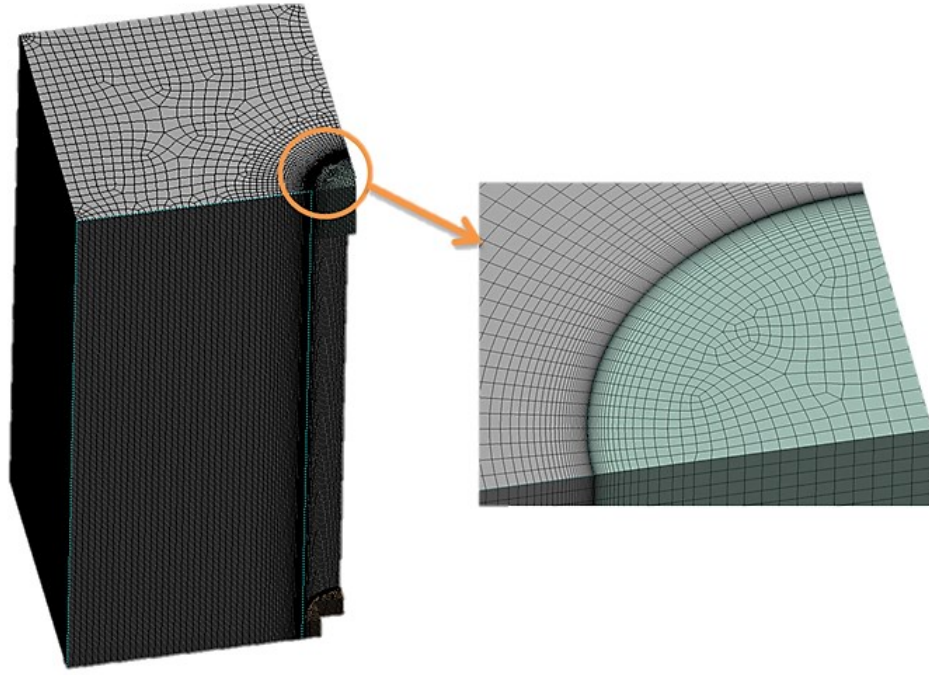


Figure 7.3: Grid distribution of the computational domain.

### 7.2.2 Performance of turbulence models

Reliable prediction of the flow field and heat transfer characteristics depends on suitable turbulence models. This section presents a comparative assessment of five RANS turbulence models for computation of heat transfer characteristics of a vertical cylinder. The RANS models used in the present study are namely  $k-\epsilon$ , *low-Re  $k-\epsilon$* ,  $k-\omega$  *STT* (2-equations), *Transitional  $k-k\ell-\omega$*  (3-equations) and *Transition SST* (4-equations) [137].

The performance of each turbulence model is assessed with respect to the predicted local heat transfer coefficient ( $h_x$ ) distribution as illustrated in Figure 7.4. The local heat transfer coefficient is calculated from:

$$h_x = \frac{q}{(T_{wall} - T_{\infty})} \quad (7.1)$$

where  $q$  is the supplied heat flux at the cylinder surface,  $T_{wall}$  is the wall temperature, and  $T_{\infty}$  is the water ambient temperature.



The heat transfer distribution predicted by the *Transition SST* turbulence model compares very well with the experimental data where the transition region was well defined as shown in Figure 7.4. On the other hand, all other turbulence models showed poorer prediction, especially the *Transitional k-kl- $\omega$*  model, which did not detect the onset of transition. The *k- $\epsilon$*  model has also failed to capture the flow transition from laminar to turbulent, but it seems to provide an average of the heat transfer coefficient along the cylinder surface. However, the *k- $\omega$  SST* model detected the flow separation but its location was delayed and shifted downstream. The predicted heat transfer coefficient by the *low-Re k- $\epsilon$*  model is the second closest result to the experimental data.

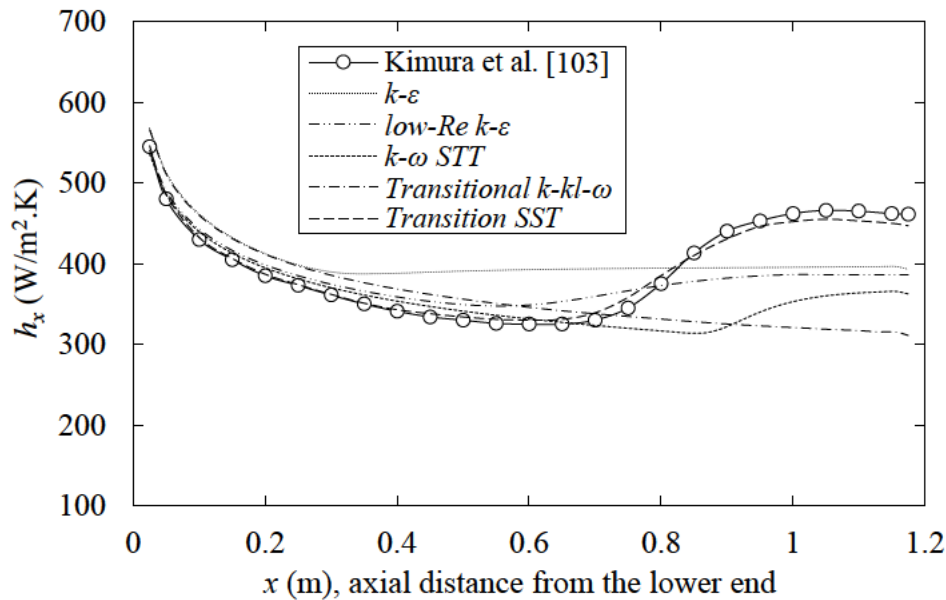


Figure 7.4: Local heat transfer coefficient for  $d = 10$  mm.

The *Transition SST* model was further used to model other cylinders with two different diameters, 26 and 165 mm. Figures 7.5 and 7.6 illustrate the numerical and experimental heat transfer coefficient for  $d = 26$  mm and  $d = 165$  mm respectively. Again, the *Transition SST* model shows a high performance to describe the heat transfer coefficient in all the flow regimes. The minor differences that can be observed are probably due to uncertainty in geometry and experimental data [103].

It can be clearly seen from Figures 7.4 to 7.6 that the heat transfer coefficient falls gradually as the cylinder height increases up to the point where the flow transition is initiated. After that, at the top region of the cylinder, the flow became fully turbulent

resulting in enhancement of the heat transfer. This can be explained by the dependency of the physical properties of water on the temperature, any change in the temperature will directly affect the flow and heat transfer characteristics.

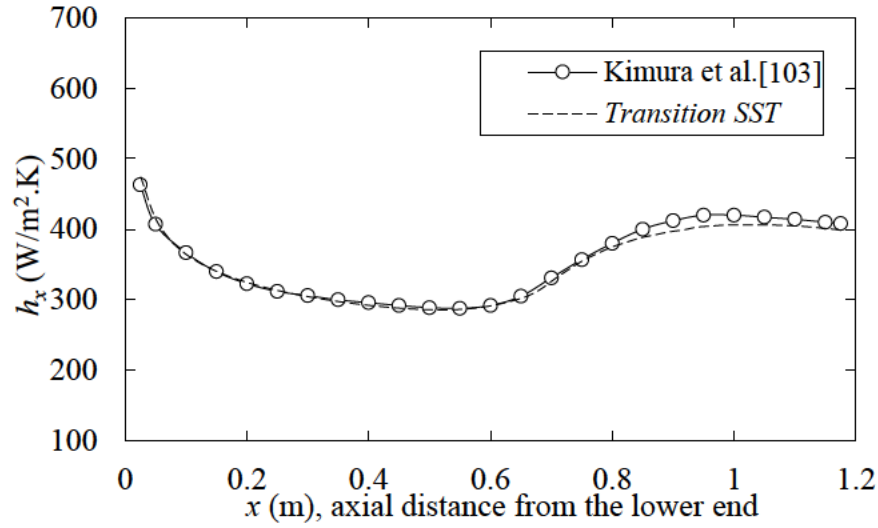


Figure 7.5: Local heat transfer coefficient for  $d = 26$  mm.

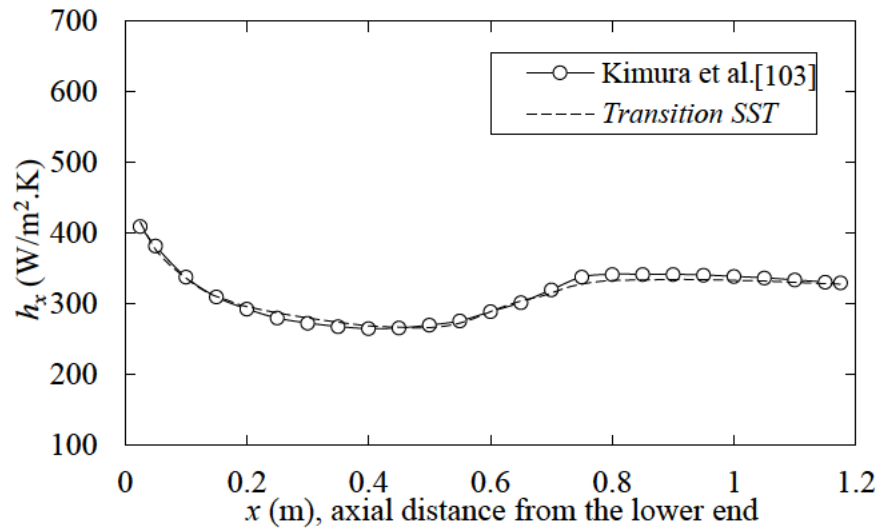


Figure 7.6: Local heat transfer coefficient for  $d = 165$  mm.

Figure 7.7 shows the viscosity and the thermal conductivity of water within the boundary layer in the vertically upward direction. The increase of surface temperature in the upward direction results in a decrease of the dynamic viscosity,  $\mu$ , and increases the thermal conductivity,  $k$ . When the surface temperature reached the peak, the water viscosity was at its lowest value which in turn increases the Rayleigh number encouraging the flow to

change its regime. At the same time, the thermal conductivity decreases due to the high temperature offering greater resistance to the heat transfer. After the flow is fully turbulent, the turbulence activities lead to reducing the temperature in the top region of the cylinder. Accordingly, the thermal conductivity increases offering less resistance to heat transfer. In general, the heat transfer coefficient is enhanced more for smaller cylinder diameters.

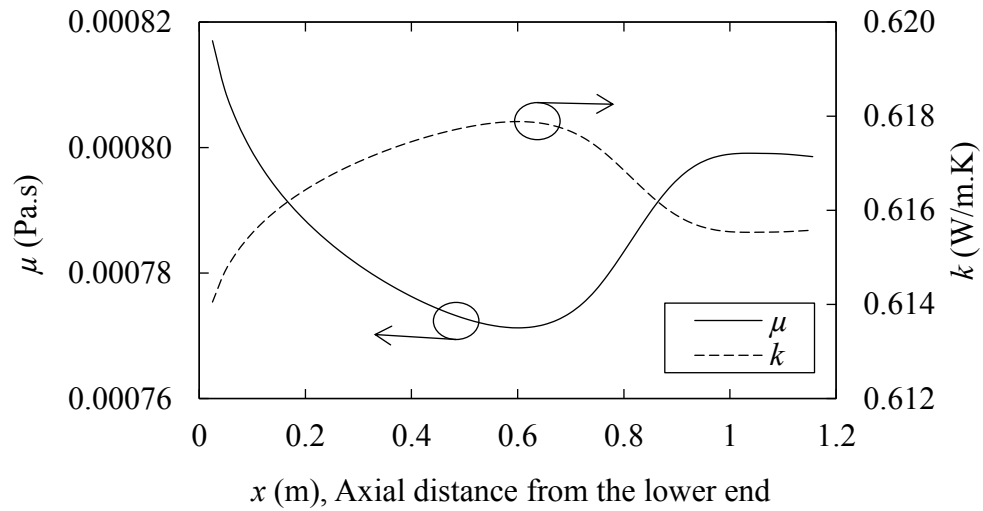


Figure 7.7: Water dynamic viscosity and thermal conductivity distributions along the cylinder surface for  $d = 10$  mm.

### 7.2.3 Heat transfer characteristics

The plots of the nondimensional local Nusselt number,  $Nu_x$ , against the local modified Rayleigh number,  $Ra_x^*$ , are shown in Figure 7.8. For the largest diameter, 165 mm, the predicted data agreed well with the correlation values for Fujii et al. [138] for vertical flat plate in the laminar regime shown in Figure 7.8 (c). Also, these data match with those obtained by Kimura et al. [103] over the laminar region as well as the turbulent region.

Figures 7.8 a-b show a comparison for the smaller diameters, 10 mm and 26 mm respectively. Overall, the current data are in good agreement with those reported by Kimura et al. [103], however, there is a deviation from the flat plate data reported by Fujii et al. [138] and this increases for the smallest diameter, 10 mm. The reason for this discrepancy is probably due to the high curvature effect of the cylinder, which is a general shortcoming of linear eddy viscosity models [16].

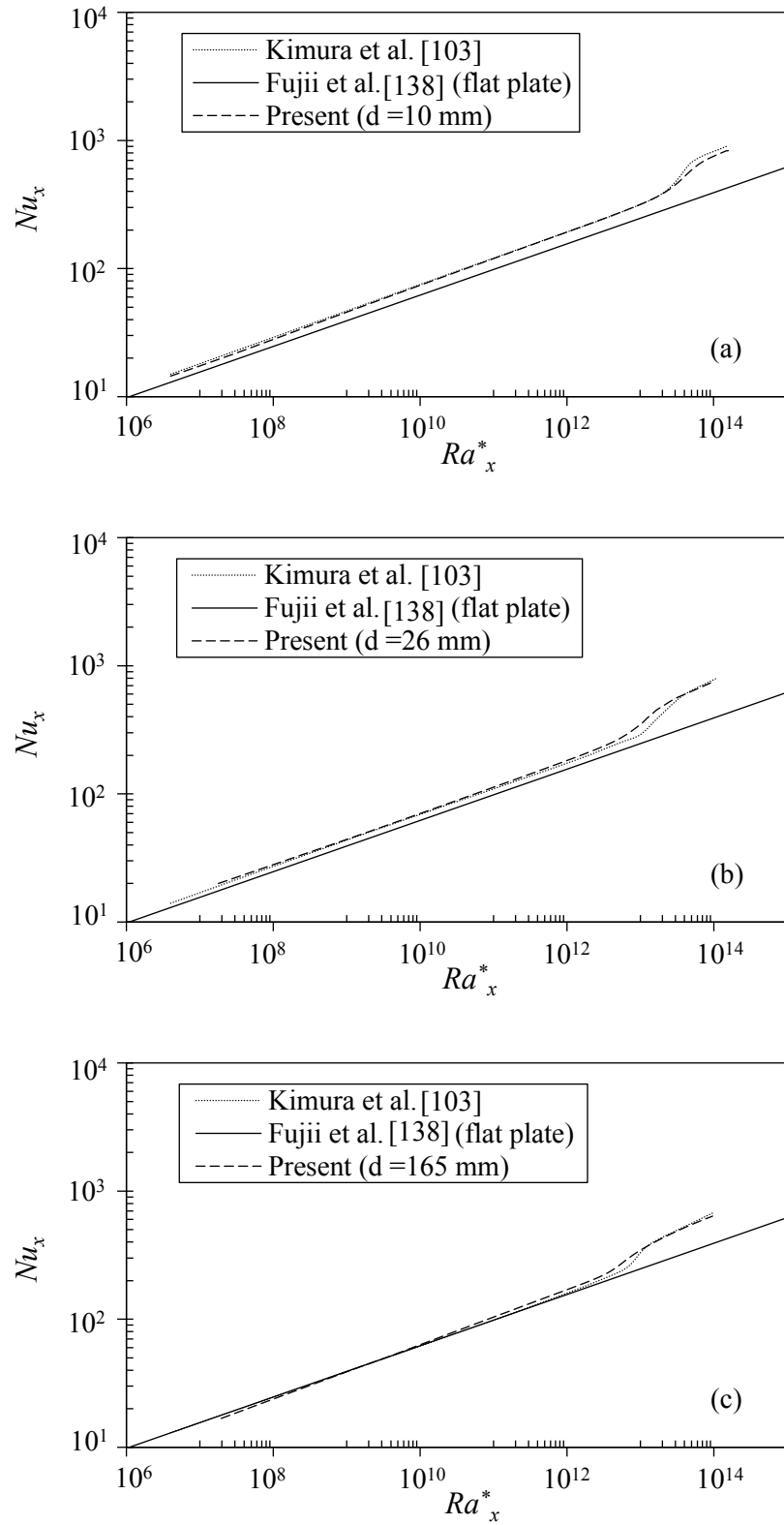


Figure 7.8: Comparisons of a local Nusselt number for different diameters (a)  $d = 10$  mm, (b)  $d = 26$  mm, and (c)  $d = 165$  mm.

#### 7.2.4 Visualisation of surface temperature

Figure 7.9 shows the temperature distributions along the surface of the cylinder for three different diameters. The colours shown in this visualisation are indicating as follows, black (low temperature), light grey (moderate temperature), and dark grey (high temperature). It can be seen from the temperature distributions shown in Figure 7.9 that the numerical approach is able to provide good predictions. The lowest temperatures were recorded in the bottom section of the cylinder, and then the temperature starts to increase in the vertically upward direction up to the separation point where the transition from laminar to turbulent occurs. After that, the temperature starts to decline where the turbulent flow is observed. The observed temperature gradient in the bottom part of the cylinder is due to the effect of the buoyancy-driven flow within the boundary layer. This flow behaviour should be more pronounced with increasing the axial distance. According to the visualisation photographs in Figure 7.9 the location of the onset of transition changes in the vertically upward direction as the cylinder diameter decreases, which is probably due to the curvature effect. When the boundary layer becomes turbulent, the temperature starts to decrease gradually in the vertically upward direction.

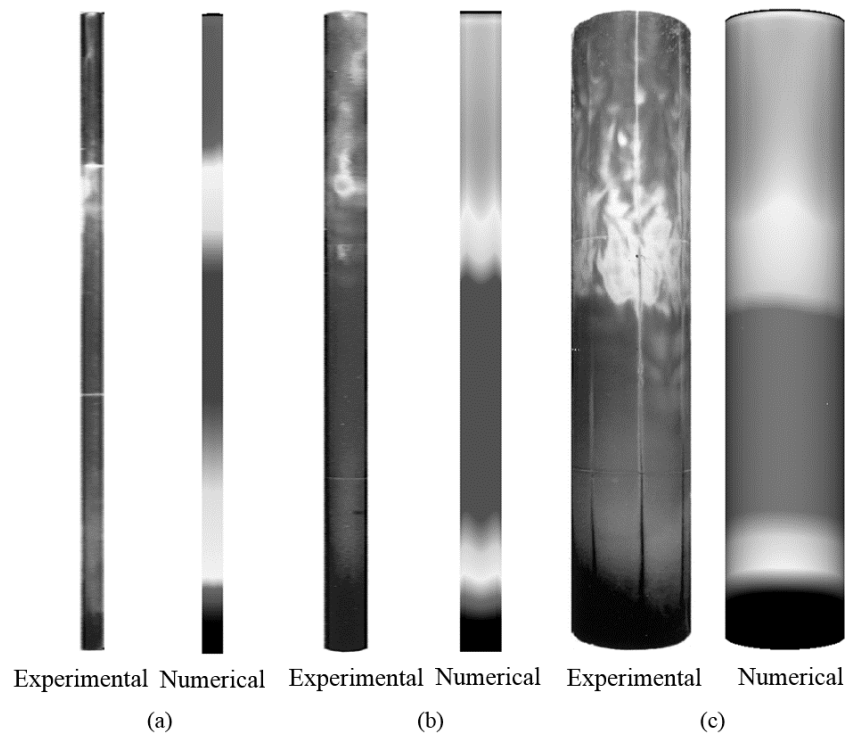




Figure 7.9: Numerical and experimental [103] temperature distribution along the cylinder surface (a)  $d = 10$  mm, (b)  $d = 26$  mm, and (c)  $d = 165$  mm.

### 7.3 Modelling of the fuel rack assembly

In this section, the computational analysis of fuel rack is presented, which essentially comprises a number of vertical cylinders that releases heat at a constant rate. The geometry of the rack arrangement is shown in Figure 7.1. Due to the symmetry of the computational domain, only half of the geometry is considered. 

---

 The mesh was generated with around 8 million cells where refinement was used in the regions between the racks and the fuel cans surfaces to ensure the  $y^+$  value is always less than one. The uniform heat flux boundary condition was used at the fuel cans surface, which is 550 W/m<sup>2</sup>. During the simulations, the pond water temperature represents the inlet flow temperature. At the inlet side, as shown in Figure 7.1, velocity inlet boundary condition is implemented in X-direction with the magnitude of 0.001 m/s, which is the typical velocity in the cooling pond, and temperature of 20 °C. Sensitivity tests were carried out for velocities of 0.0005 m/s and 0.002 m/s which showed very insignificant effect on velocity and temperature within the rack which is the zone of interest for this study. At the outlet side, outflow condition was used.

The problem involved flow transition from laminar to turbulent along the surface of the fuel rods as the maximum modified Rayleigh number reached a magnitude of the order of  $10^{15}$ . Due to the superior performance for this kind of flow as evidenced by section 7.2.2, the *Transition SST* turbulence model is used to take into consideration the turbulent effects. The top water surface was treated in the similar manner as described in Chapter 4. Various time steps were carefully examined to obtain the convergence. The transient calculation was conducted using a time step of 0.1 sec until the solution reached the steady state.

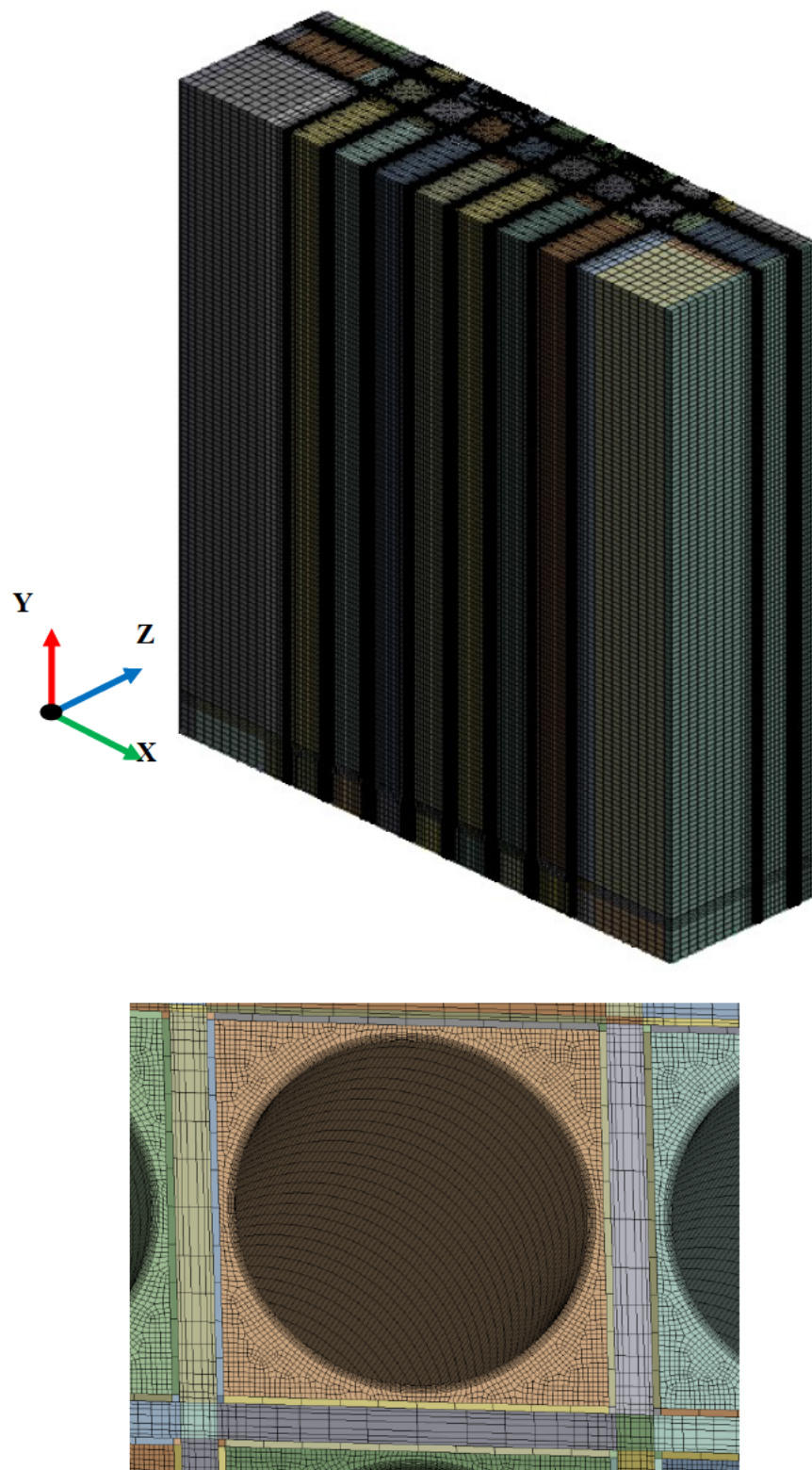


Figure 7.10: Computational grid for a fuel assembly.



### 7.3.1 Flow field and streamlines

Figures 7.11 and 7.12 show the streamlines of the water flow through the rack arrangement and the velocity contours on the symmetry plane. The water enters the rack assembly from the flow passes located at the bottom from both sides then starts to flow vertically upward due to the buoyancy force. It can be seen that the flow within the racks tends to be weak compared to the flow around the entire arrangement. Also, plumes of relatively higher velocity magnitudes from the lid holes can be observed. This is also in line with the plot of the vector field at the lid region as shown in Figure 7.13.

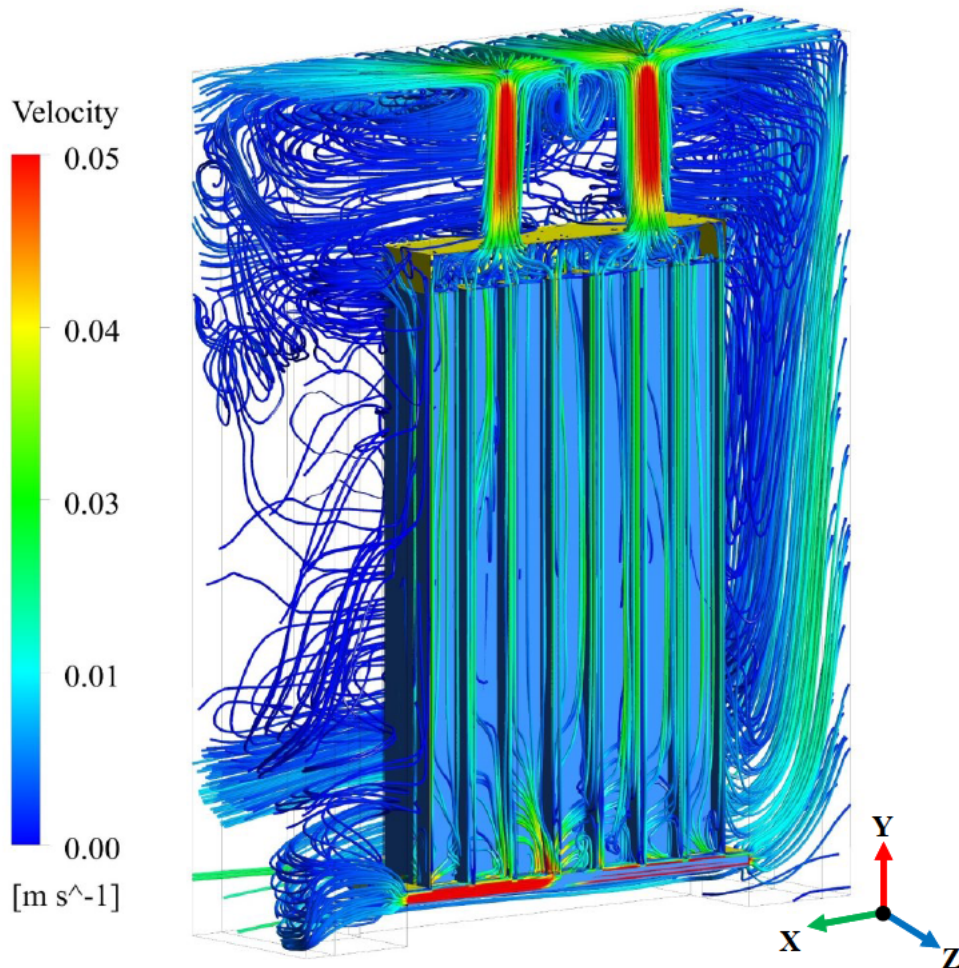


Figure 7.11: Streamlines of the flow through the rack arrangement.



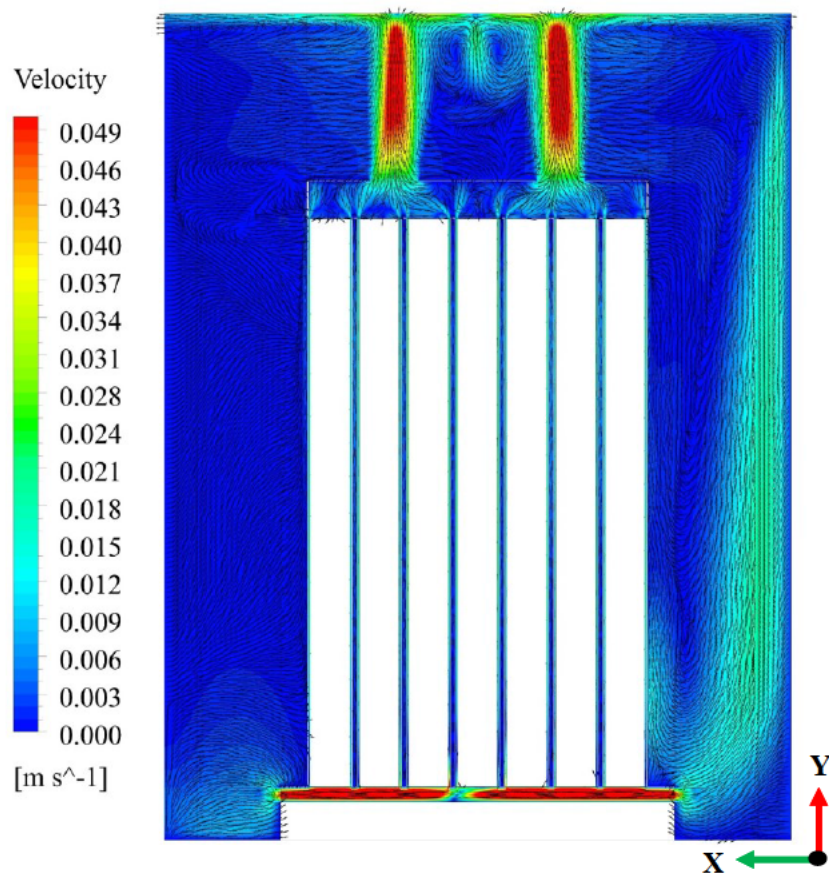


Figure 7.12: Velocity contour on the symmetry plane.

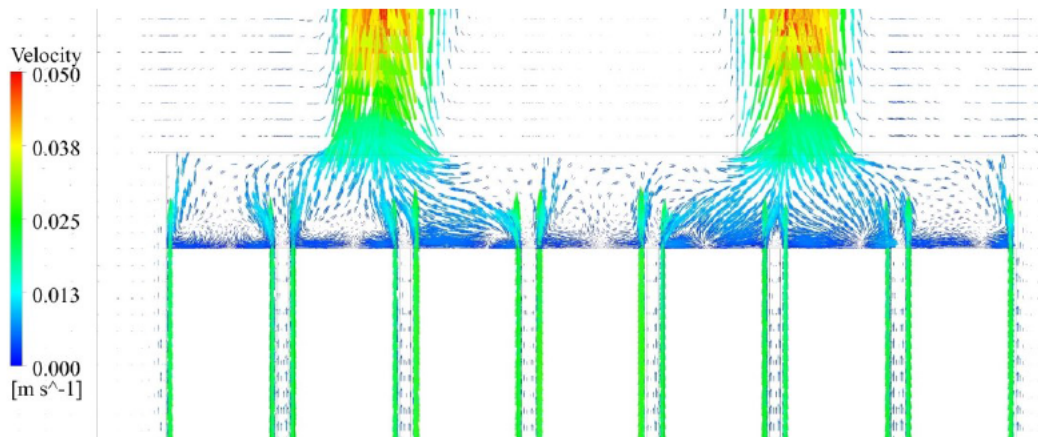


Figure 7.13: Vector field on the symmetry plane.

### 7.3.2 Temperature distribution

The temperature distribution on the symmetry plane is shown in Figure 7.14. It can be clearly seen that the temperature distributions are lined up with the velocity profile for

the same plane. Moreover, the peak temperatures were recorded in the regions enclosed by the fuel cans and the rack fabrications. Figure 7.15 illustrates the temperature profiles on the horizontal planes parallel to the X-Z plane. It can be seen that, inside the racks, the temperature at the bottom plane is relatively lower than the upper plane and this is due to the buoyancy-driven flow in these regions.

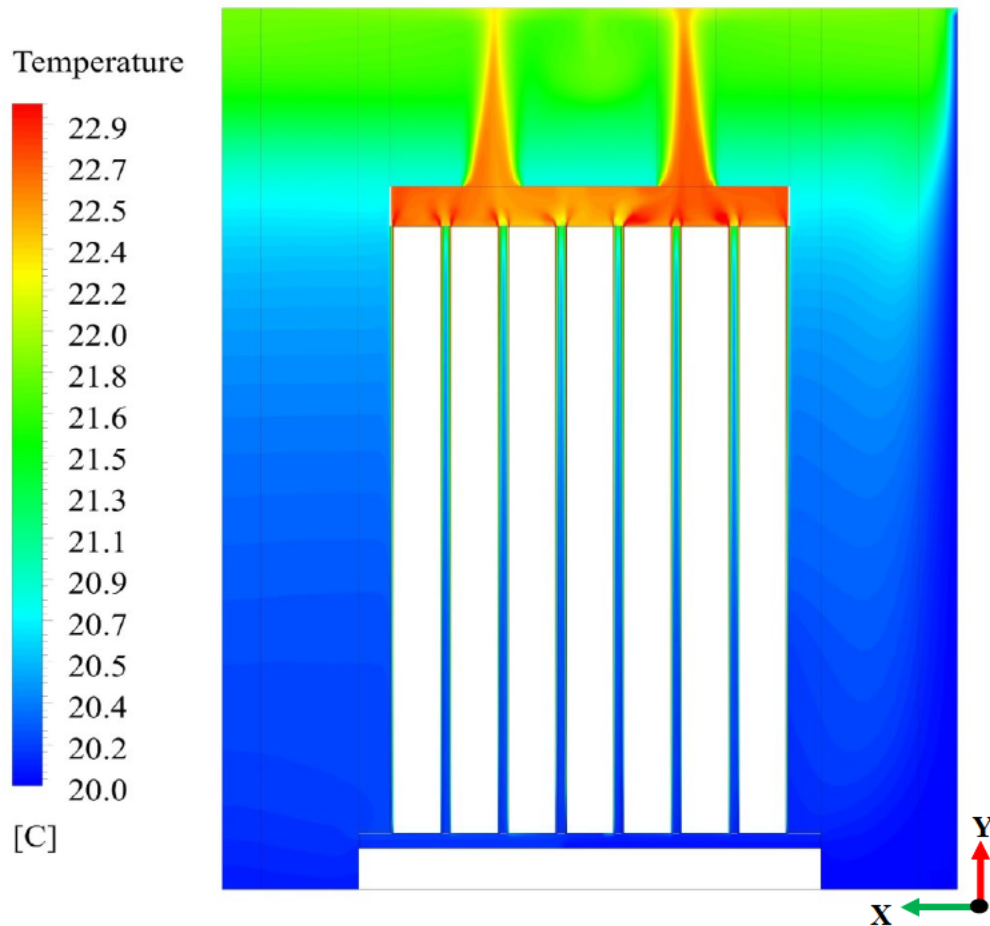


Figure 7.14: Temperature profiles on the symmetry plane.

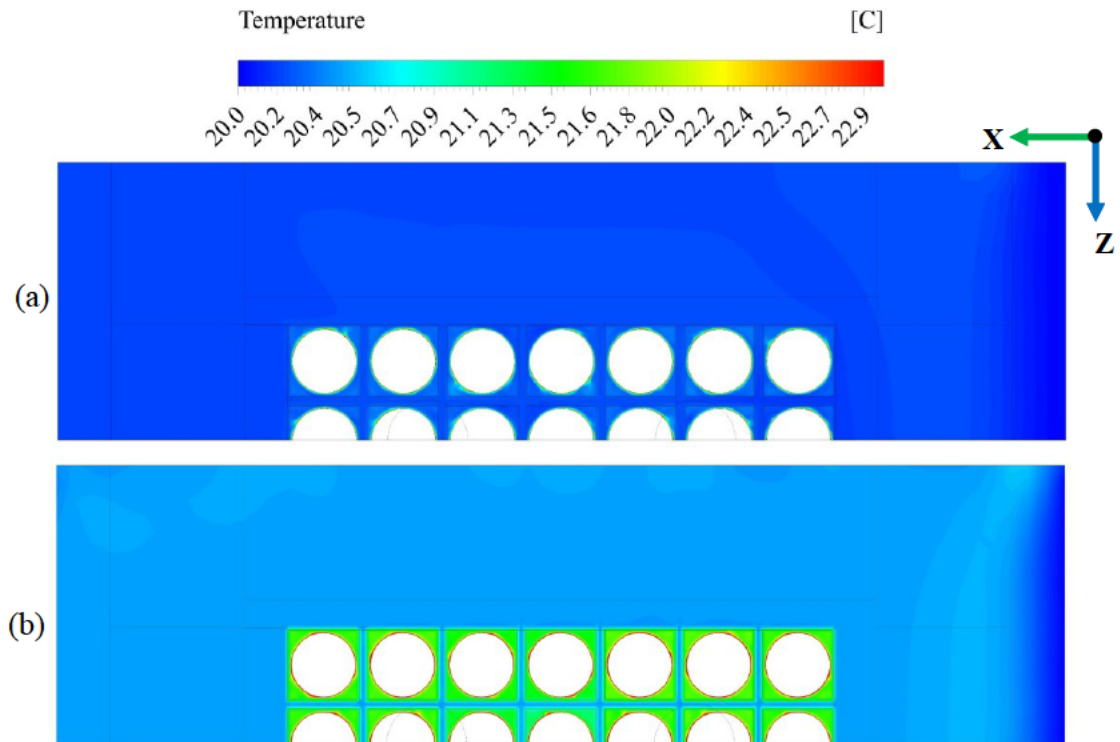


Figure 7.15: Temperature distributions on the horizontal planes at (a)  $Y=1\text{m}$  and (b)  $Y=3\text{m}$  measured from the bottom.

### 7.3.3 Determination of maximum water temperature

As shown in the previous section, the water temperature within the fuel assemblies can be higher than the pond temperature and hence estimation of the maximum temperature will be useful. In order to achieve that, the CFD model for the fuel arrangement was further used to perform a parametric study by varying the heat load and the pond water temperature as shown in Table 7.1. This results in a total of 25 simulations to be carried out.

Table 7.1: Pond temperature and heat flux used in the parametric study.

Pond temperature (°C)	Heat flux (W/m <sup>2</sup> )
20	20
30	75
40	150
50	350
60	550

As mentioned before, the peak value of water temperature within the assembly was always found in the regions enclosed by the fuel cans and the rack fabrications, more specifically near to the surfaces of the cans. The simulation results were obtained in terms of maximum temperature difference ( $\Delta T_{max}$ ) between the peak and pond values as shown below:

$$\Delta T_{max} = T_{peak} - T_p \quad (7.2)$$

The obtained  $\Delta T_{max}$  from all of the simulations were plotted with regard to the pond temperature and the heat flux illustrated in Figure 7.16. It can be clearly seen that the value of  $\Delta T_{max}$  increases as the heat flux increases. On the other hand,  $\Delta T_{max}$  decreases as the pond temperature increase, especially for high heat flux values, the decrease is more obvious. Also, it seems that at the lowest pond temperature the maximum values of  $\Delta T_{max}$  are achieved.

The data shown in Figure 7.16 were used to obtain a correlation of  $\Delta T_{max}$  as a function of the heat flux as well as the pond temperature, which is expressed as:

$$\Delta T_{max} = 0.1492 (q)^{0.7786} (T_p)^{-0.55} \quad (7.3)$$

here the value of  $T_p$  is in Celsius and  $q$  is the heat flux in W/m<sup>2</sup>.

The empirical coefficients of Eq. (7.3) were obtained after several trials such that one single expression could describe  $\Delta T_{max}$ . The developed correlation is way is always over predicts  $\Delta T_{max}$  and the maximum recorded difference between the correlation and the simulation values was about + 9.9% for  $q=20 \text{ W/m}^2$  and  $T_p=50 \text{ }^\circ\text{C}$ . However, the developed correlation is only valid for the range of heat fluxes and pond temperatures as given in Table 7.1. This correlation can be introduced to the spreadsheet model (Chapter 5) to evaluate the maximum localised temperature in the pond water, which is critical safety issue for pond operation.

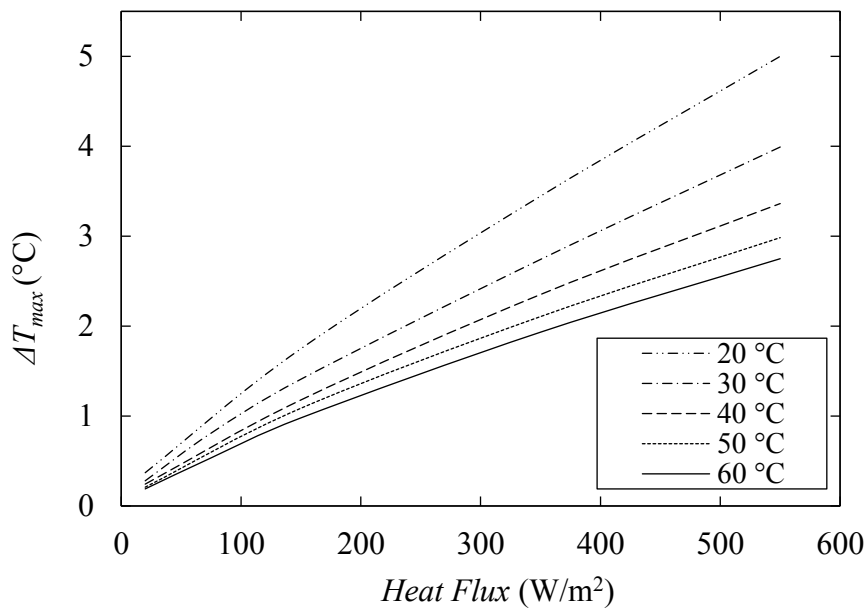


Figure 7.16: Maximum Temperature difference as a function of the heat flux and pond temperature.

## 7.4 Summary

The modelling methodology of a heated vertical cylinder submerged in a water tank was successfully established. Numerical simulation was conducted and the results were validated against the experimental data reported by Kimura et al. [103]. The CFD model was able to predict the temperature distribution along the heated surface of the cylinder and locating the flow separation point with good accuracy. The predicted results showed sensitivity to various eddy viscosity models where *Transition SST* model was the only model, amongst the selected models able to capture the transition region with good

accuracy. It is believed that the results obtained from this study will be useful for modelling flow in situations where a large number of heated cylinders are involved.

A CFD model of the fuel assemblies was developed where the knowledge gained from the modelling of the vertical cylinder was implemented. The fluid flow and heat transfer characteristics were established. The results showed that the water contained in the regions between the racks and the fuel cans is almost stagnant and the highest temperatures were recorded in the same regions irrespective of the pond temperature and heat flux and are largely determined by the geometry.

A parametric study was conducted by varying the pond temperature and the heat flux to determine the maximum temperature within the rack. As a result, a correlation for the temperature difference, between the maximum and pond, was proposed as a function of the heat flux. This correlation can be adapted to the spreadsheet model developed in the previous chapter.

## **Chapter 8 Study of Thermal Performance of the SNF Ponds Using Spreadsheet Model**

### **8.1 Introduction**

After confirming its reliability, the spreadsheet model was used to study the thermal behaviour of the Sellafield cooling pond to assess the appropriateness of using particular assumptions in the analysis of loss of cooling scenario. From the point of view of safety and economics, it is essential to analyse the performance of the pond under accident scenarios as well as under normal operating conditions. As shown from the literature, Chapter 2, that the analysis of the SNF cooling ponds performance under normal operating conditions was less discussed in the literature, in particular for large-scale cooling ponds.

This study splits into two main parts; the first part is the analysis of the pond behaviour under different conditions, when include maximum heat load and loss of cooling scenario. In the same part, the rate of temperature increase as well as the impact of the weather conditions are evaluated. In the second part, a sensitivity study is conducted using Taguchi method and the statistical method of ANOVA to assess the effect of the operational configurations on the cooling performance.

### **8.2 Analysis of the pond thermal behaviour**

#### **8.2.1 Maximum heat load**

The calculations in this section are performed considering that the pond is loaded with the maximum possible heat load and all of the cooling systems are in place and under control. The maximum heat load is 10 MW, which corresponds to the maximum expected amount of spent fuel to be stored and is assumed to be uniformly distributed throughout

the pond. In order to obtain conservative results, the considered heat load in the calculation is greater than the maximum value by 10%. The input parameters used in this calculation are listed in Table 8.1.

Table 8.1: Configurations used in the case of normal operating conditions.

Parameter	Value
Heat load (MW)	11
Outside environment temperature (°C)	14
Recirculation flow rate (kg/s)	115.74
Cooling tower efficiency (%)	60
Make-up rate (kg/s)	13.9
Make-up temperature (°C)	14
Ventilation inlet rate (m <sup>3</sup> /s)	12

The results for the maximum heat load case are presented in Figure 8.1 in terms of bulk water and hall temperatures. As shown in this figure, at the beginning of the calculations the water and air temperatures have the same value of 14 °C. As time progresses, both water and air temperatures increase until the steady state is reached at values of 41.5 °C for the water and about 31.3 °C for the indoor air.

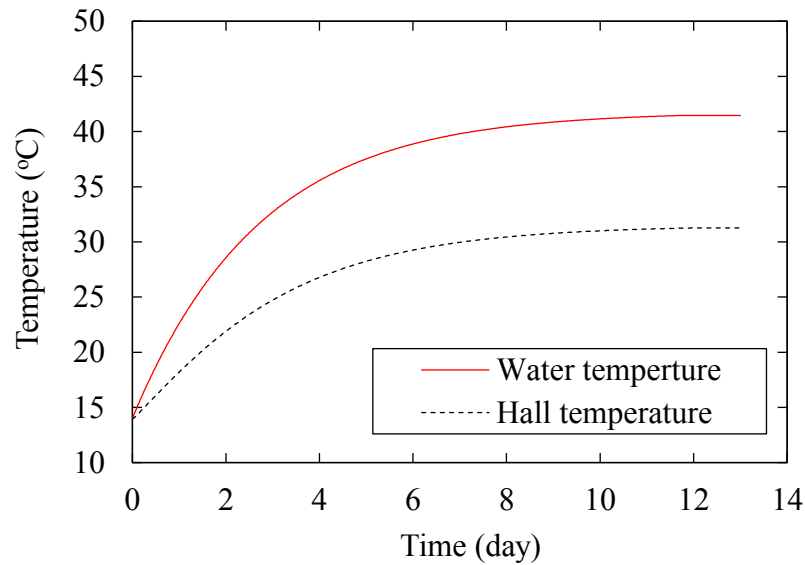


Figure 8.1. Water and air temperatures of the cooling pond under the maximum heat load.



The decay heat is removed via different modes as shown in Figure 8.2. Furthermore, this figure illustrates the contribution of each of the heat removal modes to the total heat removed from the water body. The decay heat removed by the recirculation dominates the cooling processes with a percentage of 77 % of the total heat loss. It appears that the heat loss from the water surface represents a relatively small proportion (8%) of the total heat loss, but it cannot be ignored. However, the scenario can be different for lower heat loads as in the cases presented in the validation section for the Sellafield cooling pond as shown in Figure 5.7.

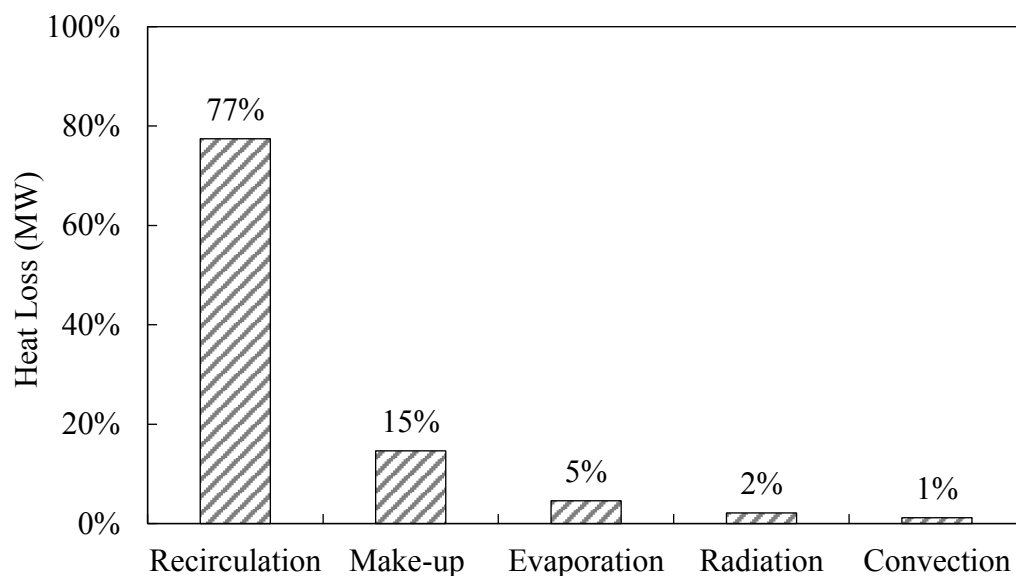
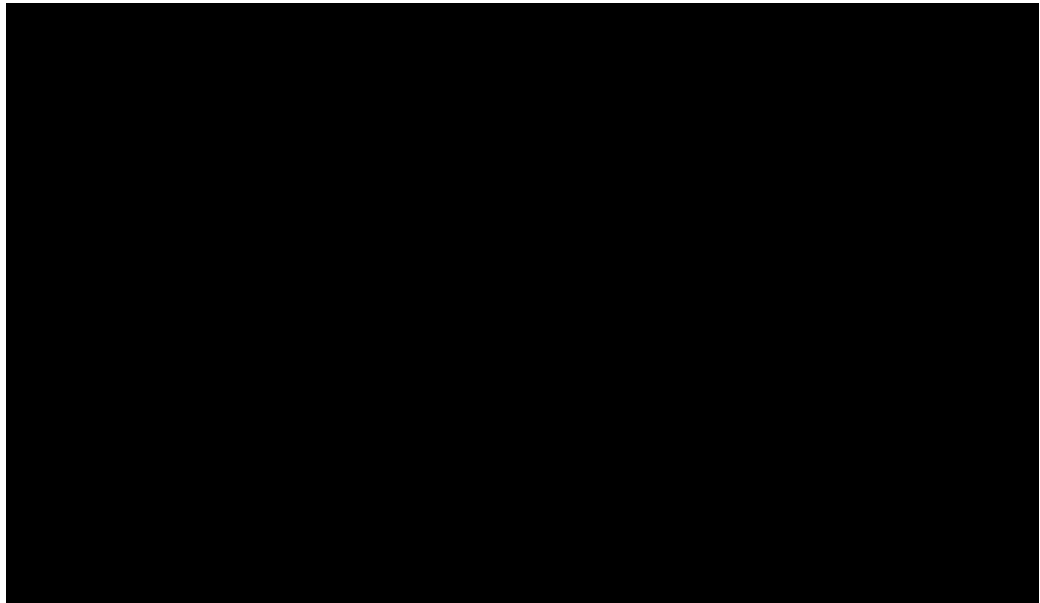
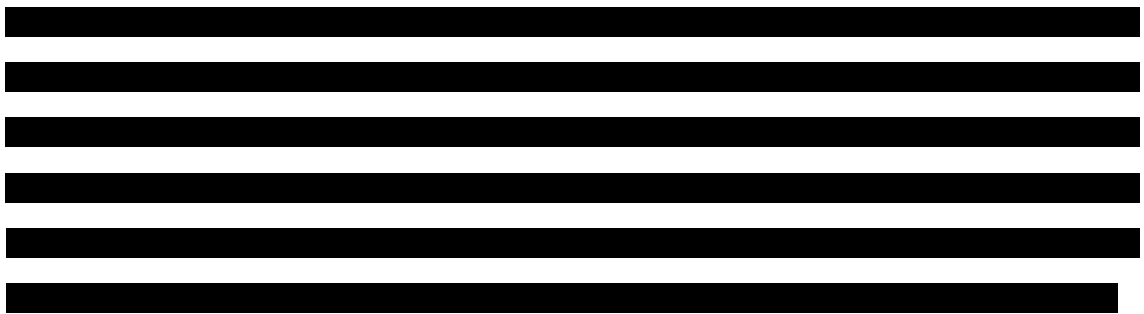


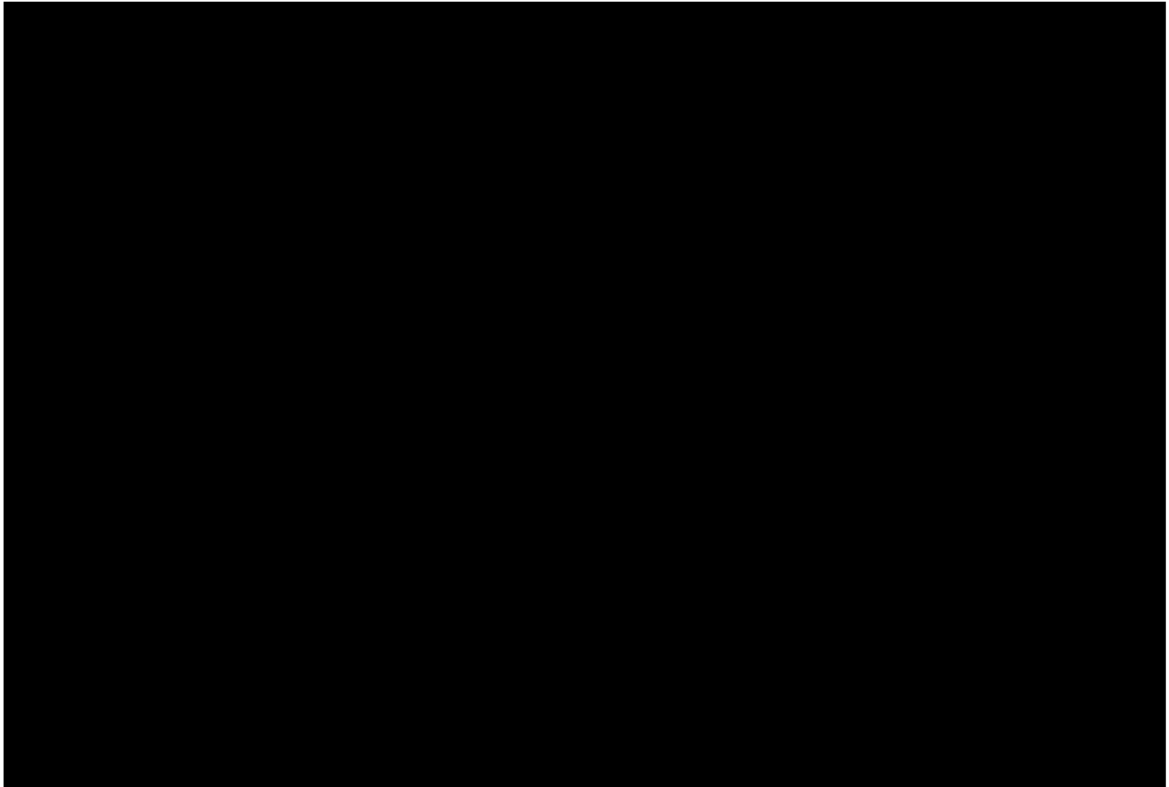
Figure 8.2. Contribution of different heat removal modes under the maximum heat load.

### 8.2.2 Loss of cooling scenario

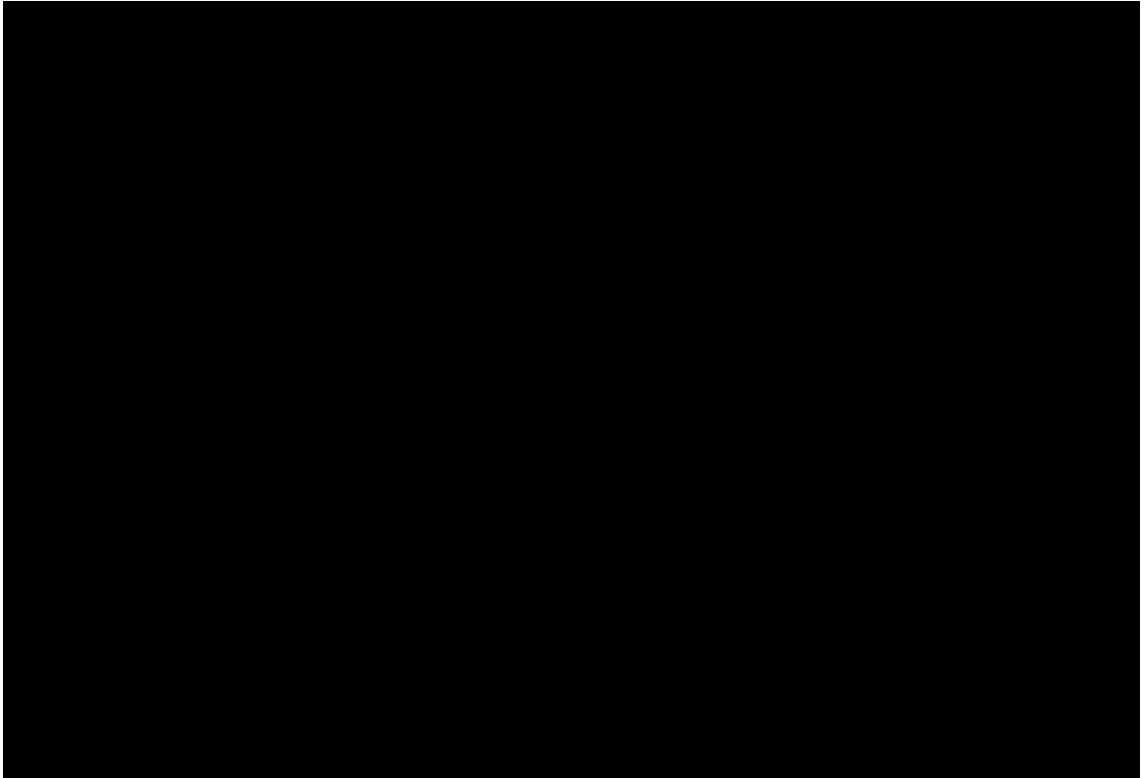
The calculations are conducted for the cooling pond taking the outcomes from the previous case of normal operating conditions as initial values. Moreover, the calculations are performed for two different conditions at the water surface. The first condition ignores the heat loss from the water surface except for the boiling heat transfer, which is represented in the graphs (Figures 8.3 and 8.4) by “Heat off”. The second condition takes into account all the heat transfer modes at the water surface, which is represented in the graphs by “Heat on”.



For the “Heat on” condition, the estimation of the time required for the fuel assembly to start to be uncovered is the same as in the “Heat on” case. On the other hand, water reaches its saturation temperature 2 days earlier than the predicted time in the “Heat on” case. However, these differences, in the presented case, are still within a good level and provide a conservative treatment for the accident scenario. For different conditions, the assumption that the heat loss from the water surface can be neglected may not be appropriate. For example, Figure 8.5 shows the effect of heat load on the validity of this assumption for different heat loads.



In Figure 8.5, for the “Heat off” situation, the sensible heating is faster for the high heat load and once the temperature reaches the boiling point, for both heat loads, the curves become parallel to X-axis. It can also be seen that adopting such “Heat off” assumption can significantly over predicts the water temperature, especially for low heat load values. In Figure 8.5, the difference between the predictions of water temperature using both assumptions is around 48% for a heat load of 0.5 MW, whereas only 18% is observed for the heat load of 2 MW. This implies that the over prediction is higher for the low heat load. This is due, as discussed before, to the large exposed area of the water surface to the ambient air, which increases the surface heat loss. Hence, such an assumption should be carefully considered while performing the analysis of accident scenarios for large-scale cooling ponds.



### **8.2.3 Rate of temperature increase**

Loss of an adequate cooling capability of the spent fuel cooling ponds, due to station blackout or any other causes, can lead to a rapid increase in pond temperature. The pond temperature may continue to increase until it reaches its boiling temperature resulting in loss of pond water at a high rate. This is can be enough to dry out the pond in very few days depending on the amount of fuel stored and its radioactivity level.

In order to estimate the rate of temperature increase per day ( $\theta$ ) under different heat load conditions, an analysis using the spreadsheet thermal model was conducted. In this analysis, it was assumed that none of the cooling systems is functioning. This analysis is conducted for “Heat on” and “Heat off” conditions, same as described in the previous section. For the “Heat on” condition the increase of pond temperature is not linear, and hence, the rate of temperature increase per day is taken as an average value and is defined as shown below:

$$\text{Rate of temperature increase per day } (\theta) = \left( \frac{T_s - T_o}{t_s} \right) \quad (8.1)$$

where  $T_o$  and  $T_s$  are the initial and steady state water temperatures respectively, and  $t_s$  is the time required to reach steady state temperature.

Figure 8.6 shows the rate of temperature increase per day for “Heat on” and “Heat off” conditions. It can be seen that the value of  $\theta$  increases almost linearly as the heat load increases for both conditions while using the “Heat off” condition leads to higher values of  $\theta$  and is more evident for higher values of heat load. It can be clearly seen that the value of  $\theta$  increases by just under 1 °C/day for the “Heat off” condition and about 0.85 °C/day for the other condition.

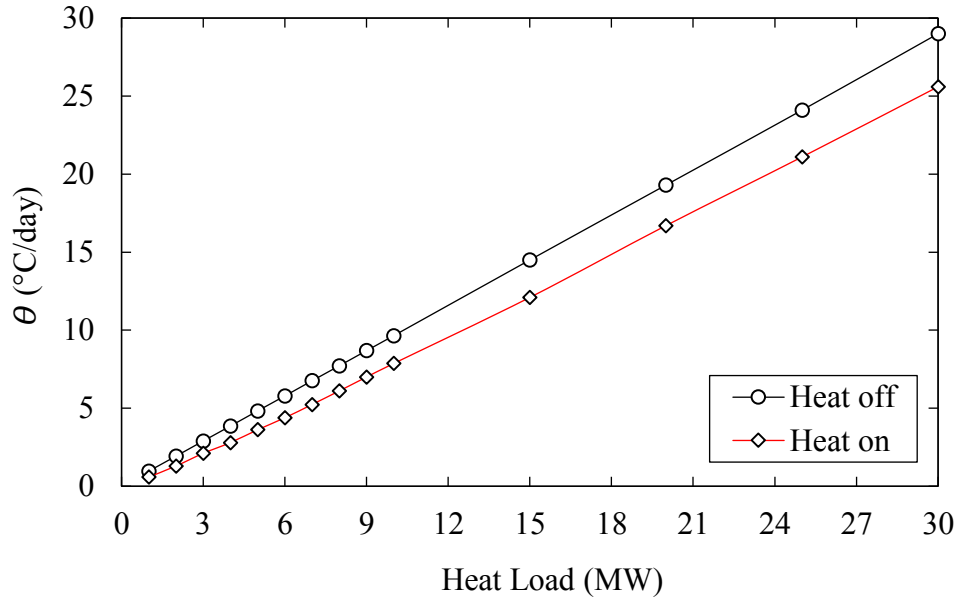


Figure 8.6: Rate of temperature increase per day for different heat load values.

Figure 8.7 represents the time required to reach the steady state temperature for different values of heat load. It can be seen that the time required to reach the steady-state conditions tends to decrease exponentially as the value of the heat load increases.

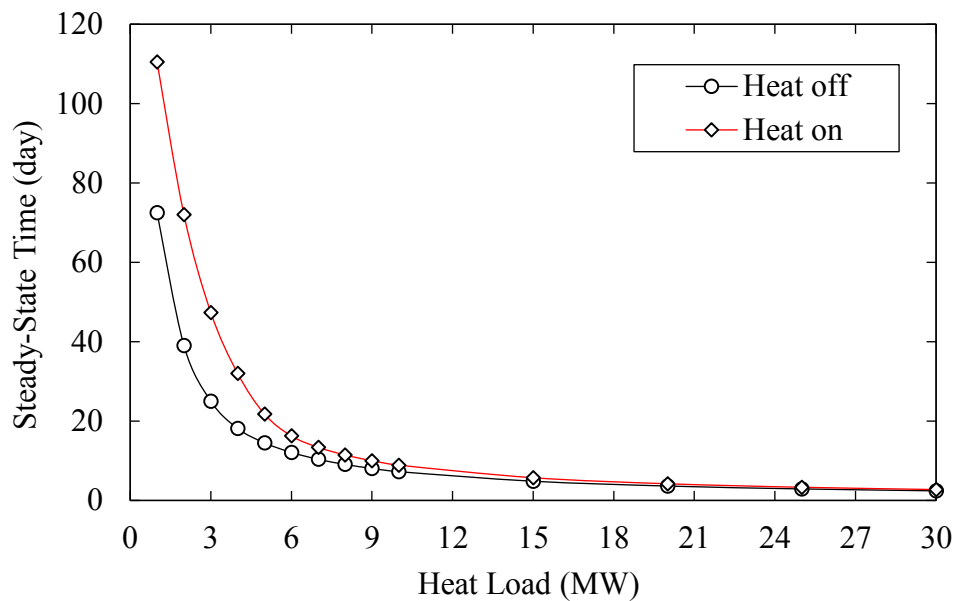


Figure 8.7: Time to reach steady state for different heat load values.

#### 8.2.4 Impact of weather conditions

The outside weather conditions are represented in the spreadsheet model in terms of outside air temperature and relative humidity. Changes in these conditions may have an effect on the cooling performance of the spent pond. To examine the potential effects, a sensitivity study was conducted by varying the outside air temperature and relative humidity. As can be seen in Figure 8.8, the outside air temperature has a significant effect on the water temperature. Increasing the outside air temperature by about 10 °C results in an increase in the water temperature by approximately 9 °C. This is because of the make-up water and ventilation air temperatures are mostly determined by the outside temperature. In addition, the temperature drop in the cooling tower, as shown in Figure 5.2, is affected by the conditions outside.

On the other hand, the relative humidity of the outside air does not have a considerable effect, as shown in Figure 8.9. This may be because of the air change per hour (ACH) for the pond hall is very low for this type of applications, at about 0.333 per hr. Meanwhile, the amount of water vapour emerging from the water surface due to evaporation is high enough to rapidly increase the relative humidity of the moist air within the pond hall.

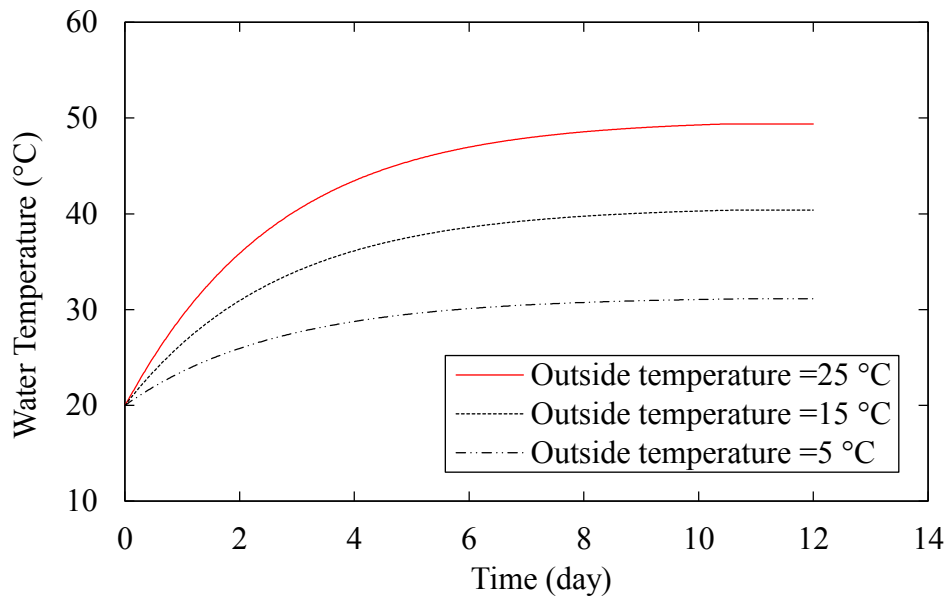


Figure 8.8. Effect of outside ambient air temperature on water temperature assuming 0% relative humidity.

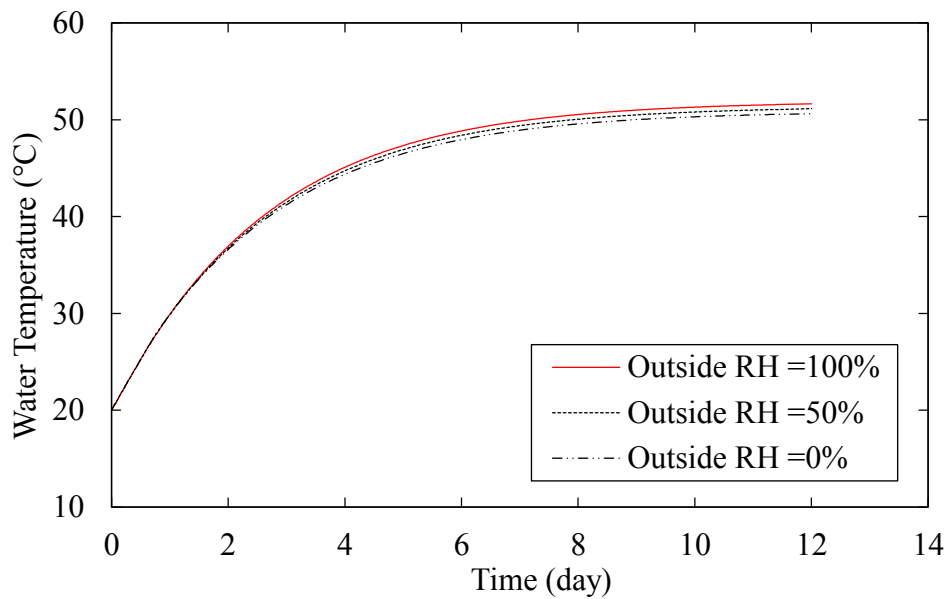


Figure 8.9. Effect of outside relative humidity on water temperature assuming an air temperature of 25 °C.

### 8.3 Sensitivity study

The cooling performance of the SNF cooling pond is measured by the ability of the pond to control the water temperature. It was shown in the previous sections that the cooling

performance of the pond could be more sensitive to some operational conditions than others. However, the sensitivity of the performance to the operational conditions can vary depending on the chosen configurations. In the previous section, for example, the outside air temperature was found to have a significant effect on the pond performance while the outside air relative humidity has a negligible effect. In order to scrutinise the effect of each of these operational conditions under various configurations, a sensitivity analysis was conducted using the statistical method of ANOVA. Conducting such an analysis can be useful for various reasons as mentioned below:

- Examine the robustness of the spreadsheet model to perform under different input parameter.
- Searching for errors in the model by encountering unexpected relationships between inputs and outputs.
- Offers more understanding of the relationships among input and output parameters, which is the cooling performance in the current study. This would be beneficial to make more reliable recommendations when decisions being made during accident scenario as well as normal operating conditions.
- Identifying the inputs that lead to significant impact on the output parameters. This can lead to simplification of the analytical model by fixing inputs that have no or insignificant impact on the outputs.
- Providing more understanding of the interaction between the input variable and its effect on the outputs.

In this section, the spreadsheet model is used to perform several simulations for different configurations of the operational conditions. After that, all of the results are collected and analysed using ANOVA analysis.

### **8.3.1 Screening process**

In the case of dealing with a large number of parameters, a primary sensitivity test can ease the study by focusing on the more sensitive parameters. Not knowing the sensitivity of parameters used in the model can result in time being inefficiently spent on non-sensitive ones. The objective of the screening process is to weed out uninfluential input



parameters by identifying input parameters that have a significant effect on the model outputs. After that, the most important factors can be further analysed via higher-resolution design.

The model input parameters can be split into uncontrolled and controlled parameters. The uncontrolled parameters are:

- Heat load
- Outside air temperature
- Outside air relative humidity

While the controlled parameters are:

- Ventilation inlet flow rate
- Make-up water flow rate
- Recirculation flow rate
- Cooling tower efficiency i.e. recirculation temperature drop

It can be noticed that the controlled parameters represent the main cooling mechanisms exist in the cooling ponds installation.

In this part, Taguchi method is used to design the configurations of the experiment. This analysis involved 7 input parameters at 2 different levels. A full factorial experiment would require 128 runs while Taguchi method with a  $L_{32}(2^7)$  orthogonal array (32 runs, 7 variables, 2 levels) would only require 32 runs.

All of the simulations conducted in this study are initialized with initial values assuming that the cooling ponds are suffering from loss of cooling i.e. water and air temperatures having a value of 100 °C. This allows studying the influence of the input parameters on the pond performance at the steady-state conditions as well as during the recovery from a loss of the cooling event. In addition, the ventilation and make-up water temperatures are assumed to have the same temperature as the outside environmental temperature.

However, the levels for each of the input parameters must be selected very carefully to minimise the interaction between their effects. In order to achieve that, the following

considerations should be taken into account while choosing the levels of each input parameter in the ANOVA analysis:

- Neither recirculation flow rate nor cooling tower efficiency to be set to zero. Since the recirculation cooling is the product of the flow rate and the temperature drop, setting any of them to zero means that the effect of the other would not be measured.
- The levels for each input parameter should provide bounding values of these parameters. This will allow examining the effect of each of the input parameters on the water temperature based on its extreme values.
- The combination of the input parameters must provide some cooling to the pond water. Otherwise, the pond temperature will remain at its initial value (100 °C) and the effect of the input parameters cannot be investigated. For example, if the heat load is chosen to have a very high value, the minimum values for the other input parameters should be sufficient to overcome the generated heat and drop the water temperature down.

The input parameters and levels used in the screening process are carefully selected according to the above mentioned considerations and shown in Table 8.2. The analysis involved 32 runs using an orthogonal array of  $L_{32} (2^7)$  as shown in Table 8.3.

Table 8.2: Input parameters and levels used in the screening process.

Input parameters	Levels	
	I	II
A, Outside air temperature (°C)	2	30
B, Cooling tower efficiency (%)	10	60
C, Ventilation inlet flow rate (m <sup>3</sup> /day)	0	12
D, Make-up water flow rate (m <sup>3</sup> /day)	0	1,200
E, Recirculation flow rate (m <sup>3</sup> /s)	2,500	10,000
F, Heat load (MW)	1	10
G, Outside air relative humidity (%)	40	100

After conducting the calculations using the spreadsheet model, the ANOVA analysis is carried out to assess the influence of each input parameter on the steady state temperature of the pond water. The statistical analysis is performed using Minitab software [128]. In the ANOVA analysis, the effects of the input parameters on the pond water temperature are measured by the Percentage Contribution Ratio (PCR) to the total mean effect and can be expressed as:

$$\text{PCR} = \frac{\text{Sum of squares of input parameter}}{\text{Total Sum of squares}} \times 100 \quad (8.2)$$

Table 8.3: Experimental design of  $L_{32} (2^7)$  Taguchi orthogonal array.

Run order	A	B	C	D	E	F	G
1	2	10	0	0	2500	1	40
2	2	10	0	0	10000	1	100
3	2	10	0	1200	2500	10	40
4	2	10	0	1200	10000	10	100
5	2	10	12	0	2500	10	100
6	2	10	12	0	10000	10	40
7	2	10	12	1200	2500	1	100
8	2	10	12	1200	10000	1	40
9	2	60	0	0	2500	10	100
10	2	60	0	0	10000	10	40
11	2	60	0	1200	2500	1	100
12	2	60	0	1200	10000	1	40
13	2	60	12	0	2500	1	40
14	2	60	12	0	10000	1	100
15	2	60	12	1200	2500	10	40
16	2	60	12	1200	10000	10	100
17	30	10	0	0	2500	10	100
18	30	10	0	0	10000	10	40
19	30	10	0	1200	2500	1	100
20	30	10	0	1200	10000	1	40
21	30	10	12	0	2500	1	40
22	30	10	12	0	10000	1	100
23	30	10	12	1200	2500	10	40
24	30	10	12	1200	10000	10	100
25	30	60	0	0	2500	1	40
26	30	60	0	0	10000	1	100
27	30	60	0	1200	2500	10	40
28	30	60	0	1200	10000	10	100
29	30	60	12	0	2500	10	100
30	30	60	12	0	10000	10	40
31	30	60	12	1200	2500	1	100
32	30	60	12	1200	10000	1	40

Table 8.4 shows ANOVA results for pond water temperature during the screening process. All the P-values are less than 0.05 except for the outside air relative humidity, G, the P- value is 0.578. This indicating that the outside air relative humidity has an insignificant effect on the pond water temperature. Meanwhile, all the other input parameters expected to affect the pond water temperature and found statistically significant at 95% level of confidence.

Table 8.4: Summary of ANOVA for the screening process using Taguchi method.

Source	DF	SS	MS	F-value	P-value	PCR
A	1	2369.7	2369.7	15.93	0.001	7.5%
B	1	2444.1	2444.1	16.43	0	7.8%
C	1	708.1	708.1	4.76	0.039	2.3%
D	1	428.3	428.3	2.88	0.03	1.4%
E	1	1979.5	1979.5	13.3	0.001	6.3%
F	1	19455.9	19455.9	130.76	0	61.9%
G	1	47.2	47.2	0.32	0.578	0.2%
Error	24	3248.5	135.4			10.3%
Total	31	31415.6				100%
DF = Degree of freedom				* Significant at the 5% level and confidence level of 95%		
SS = Sum of squares						
F =F-test value				P-value = Probability value		

Reducing the number of runs by using Taguchi method may lead to less accurate outcomes of the ANOVA analysis. For this reason, the same test is conducted using a full factorial design in order to examine the accuracy of Taguchi method under the presented case. The outcomes from ANOVA obtained by using Taguchi method and full factorial design are compared as shown in Figure 8.10 in term of PCR for each of the input parameters. The comparison confirms the reliability of using Taguchi method to design the experiment and can be used in further analysis.

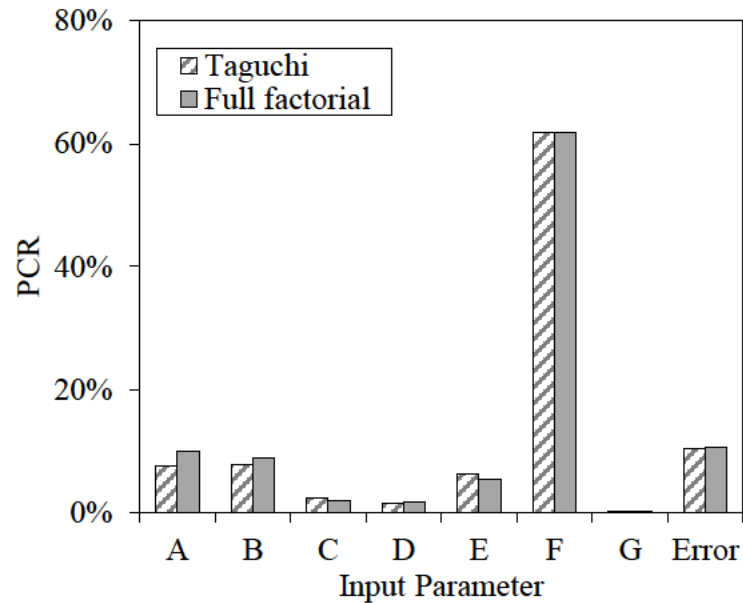


Figure 8.10: Comparison between PCRs obtained by Taguchi method and full factorial design.

### 8.3.2 ANOVA at different heat loads

The screening process showed that the outside air relative humidity, G, has an insignificant effect on the water temperature. Hence, this parameter can be excluded from any further analysis and devote the effort on the other input parameters. In addition, instead of taking the heat load as an input parameter, it can be fixed and the analysis can be conducted individually at each heat load value. This reduces the number of input parameters to 5 parameters. The sensitivity study can be conducted using Taguchi method with a  $L_{27} (2^5)$  orthogonal array (27 runs, 5 variables, 3 levels). This reduces the number of runs from 243 (in the full factorial design) to 27 runs.

The input parameters are carefully selected according to the considerations mentioned before. The used input parameters and their levels are shown in Table 8.5. For convenience and consistency, the same numbering system for the input parameters is used as in the screening process and this system will remain in use throughout this chapter.

Table 8.5: Input parameters and levels used in the ANOVA analysis with 5 input parameters.

Input parameters	Levels		
	I	II	III
A, Outside air temperature (°C)	2	10	30
B, Cooling tower efficiency (%)	5	30	60
C, Ventilation inlet flow rate (m <sup>3</sup> /day)	0	6	12
D, Make-up water flow rate (m <sup>3</sup> /day)	0	600	1,200
E, Recirculation flow rate (m <sup>3</sup> /s)	2,500	5,000	10,000

In the ANOVA analysis, the effects of the input parameters on the pond water temperature are measured by the PCR to the total mean effect at various time periods. The results from the ANOVA analysis are presented via bar charts under different heat load values as shown in Figures 8.11 to 8.14. It can be clearly seen that the effect of each input parameter on the water temperature varies with the time. Since water temperature is initiated from the boiling point, the progression of time represents a drop in water temperature. Therefore, the PCR of each input parameter also varies according to the water temperature.

In general, the effect of the recirculation cooling mechanism is the highest amongst all of the others mechanisms. This is evidenced by the large PCR for the recirculation flow rate and the cooling tower efficiency, as combined, throughout all of the periods considered up to the steady-state. However, the most influential parameter is the cooling tower efficiency with PCR, which varies from 27% to 45%, depending on the value of the heat load. On the other hand, the influence of the outside air temperature is the lowest, except in few occasions, which will be discussed later.

At day 2, it was found that the influence of the ventilation system is higher than any other period with PCR ranging from 28% to 47% while the outside air temperature and make-up water have the lowest effect on the water temperature with PCR ranging from 4% to 20%. As the time progresses, the effect of the ventilation system continues to decline until it reaches its minimum value at the steady-state conditions. In contrast to the ventilation,

the influence of the make-up water flow rate and the outside air temperature on the water temperature increases as long as the water temperature is declining.

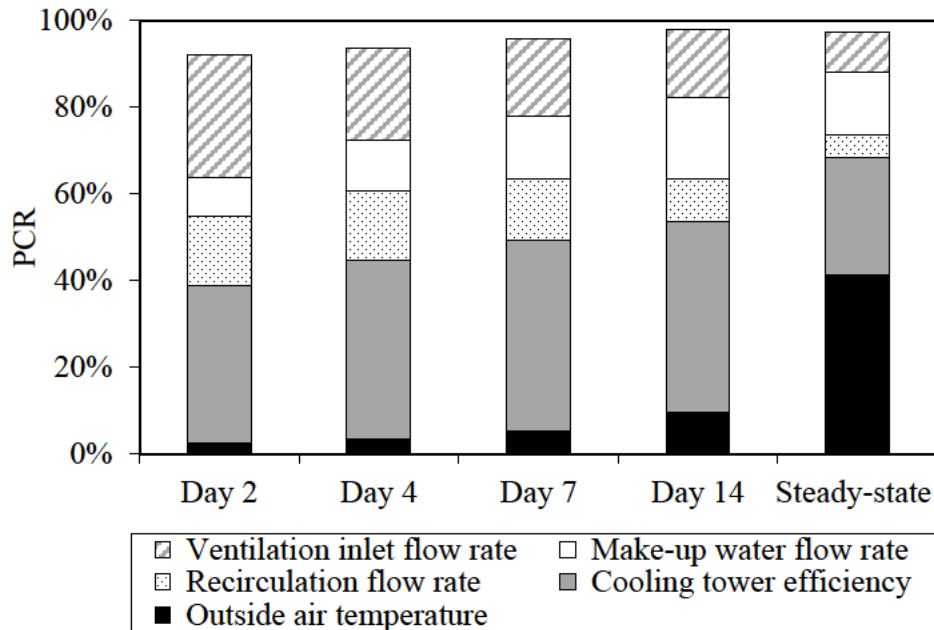


Figure 8.11: PCR of the input parameters for heat load of 1 MW.

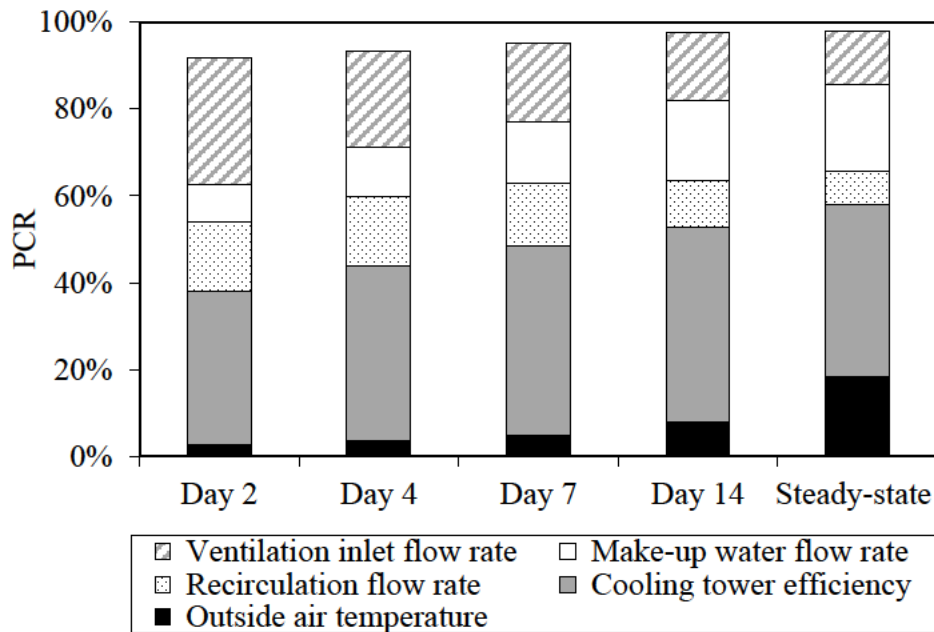


Figure 8.12: PCR of the input parameters for heat load of 2 MW.



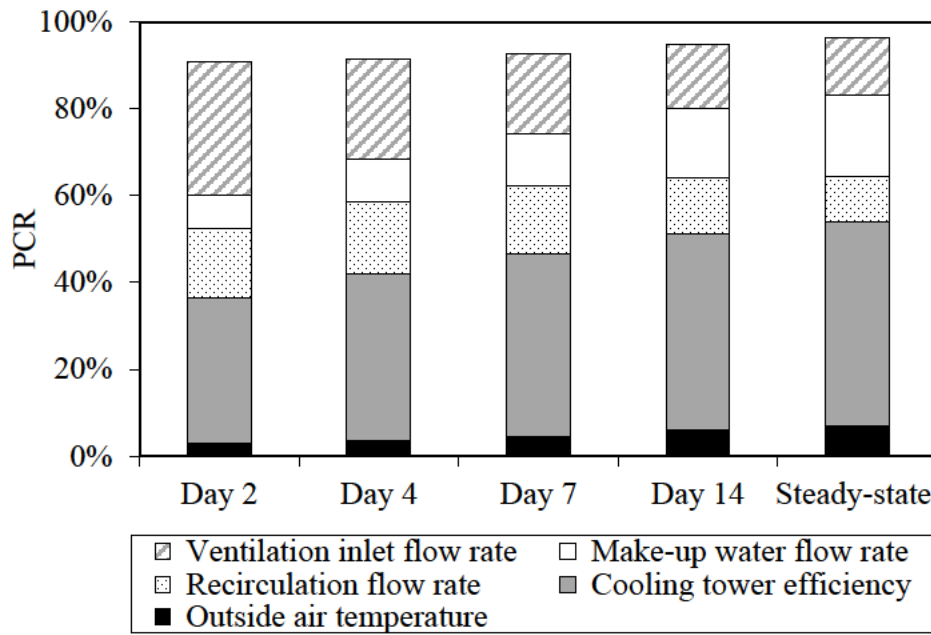


Figure 8.13: PCR of the input parameters for heat load of 5 MW.

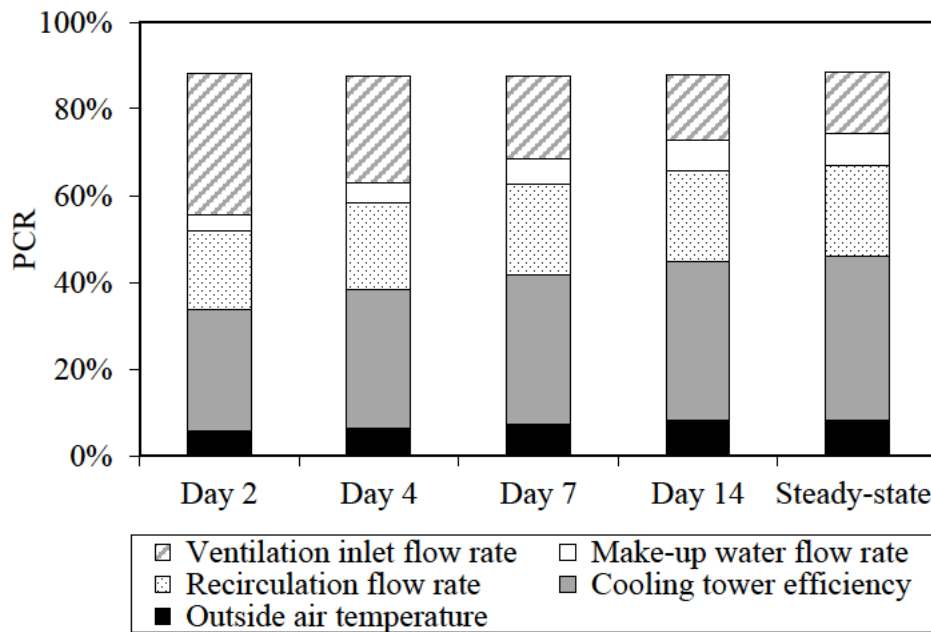


Figure 8.14: PCR of the input parameters for heat load of 10 MW.

It can be seen that the effects of the input parameters vary depending on the heat load value. In order to make a better comparison, the ANOVA results are rearranged and plotted at each heat load as shown in Figures 8.15 to 8.19.

During the first 12 days after the recovery of cooling, the effect of the outside air temperature is not sensitive to low values of the heat load as shown in Figure 8.15. For high heat load, however, the effect is more pronounced but not significant as the PCR varies 3% to a maximum of 7% during this period. The same behaviour is observed for the period starting from almost day 12 up to the steady-state but only under high values of heat load. The effect of the outside air temperature increases very rapidly for low values of heat load. This indicates that the outside air temperature is only significant at low heat load and low water temperature in the same time.

Figure 8.16 shows the effect of the heat load on the PCR of the cooling tower efficiency. It can be seen that the PCR of the cooling tower efficiency, up to day 12, decreases as the heat load increases by almost 7%. After day 12, the effect of the cooling tower efficiency sharply declines for low heat loads while under high heat loads the PCR follows the previous behaviour. This is implying that the effect of the cooling tower efficiency is dominated by water temperatures up to day 12 and after that is more dominated by the outside air temperature as evidenced by Figure 8.15.

The effect of the heat load on the performance of the ventilation system is shown in Figure 8.17. In general, the PCR of the ventilation inlet flow rate increases as the heat load increases, however, this increase is more noticeable at the low heat load values.

Figure 8.18 shows the effect of the heat load on the PCR of the make-up water flow rate. The same effect, as in the cooling tower efficiency plot, can be observed on PCR of the make-up water flow rate. The effect of the make-up water flow rate decreases as the heat load increases up to 12 days and then shows a sudden drop only for the low heat load values. It can be clearly seen that the sudden increase in the PCR of the outside air temperature is followed by a sudden decrease in the PCRs of the cooling tower efficiency and the make-up water flow rate. This reveals that there is an interaction between the PCR of the outside air temperature and the PCRs of cooling tower efficiency and make-up water flow rate.

Finally, the effect of the heat load on the contribution of the recirculation flow rate is shown in Figure 8.19. It can be noticed that the PCR of the recirculation flow rate generally increases as the heat load increases and becomes more obvious as the water temperature goes toward the steady-state conditions.

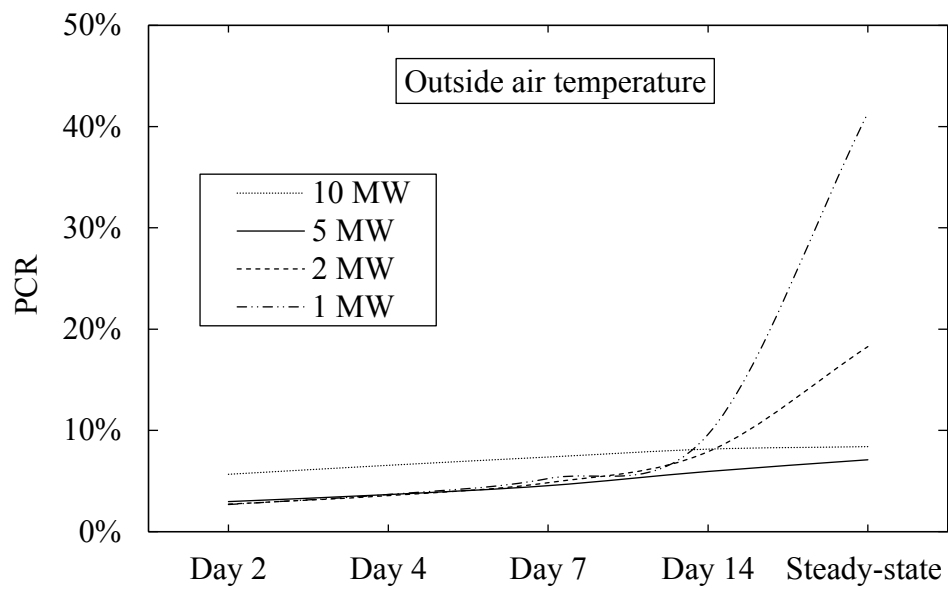


Figure 8.15: Effect of heat load on the PCR of the outside air temperature.

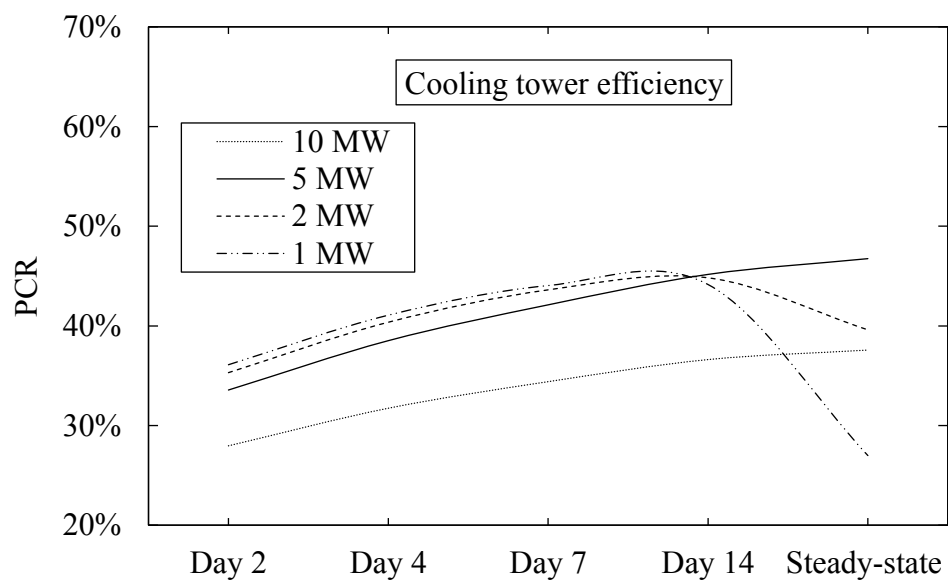


Figure 8.16: Effect of heat load on the PCR of the cooling tower efficiency.

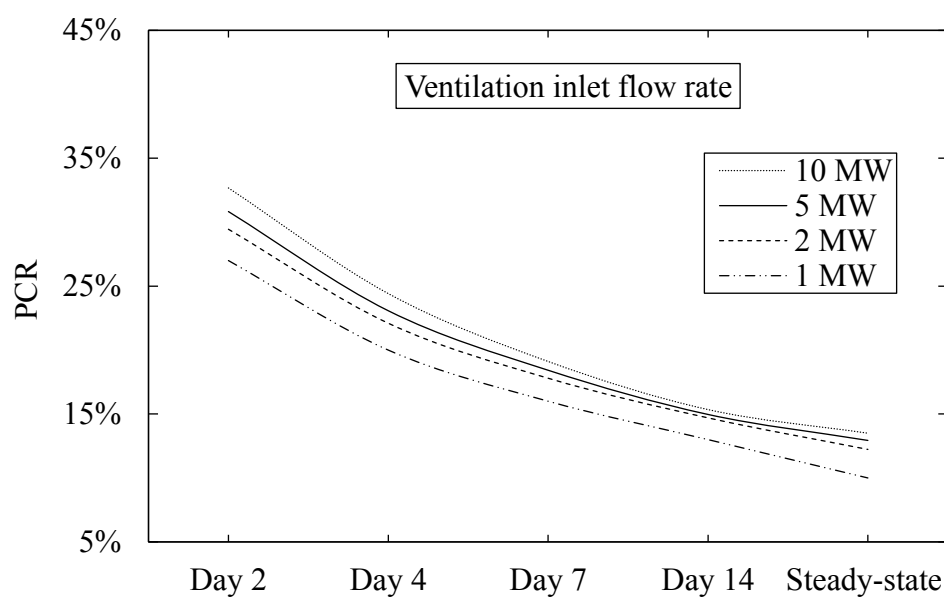


Figure 8.17: Effect of heat load on the PCR of the ventilation inlet flow rate.

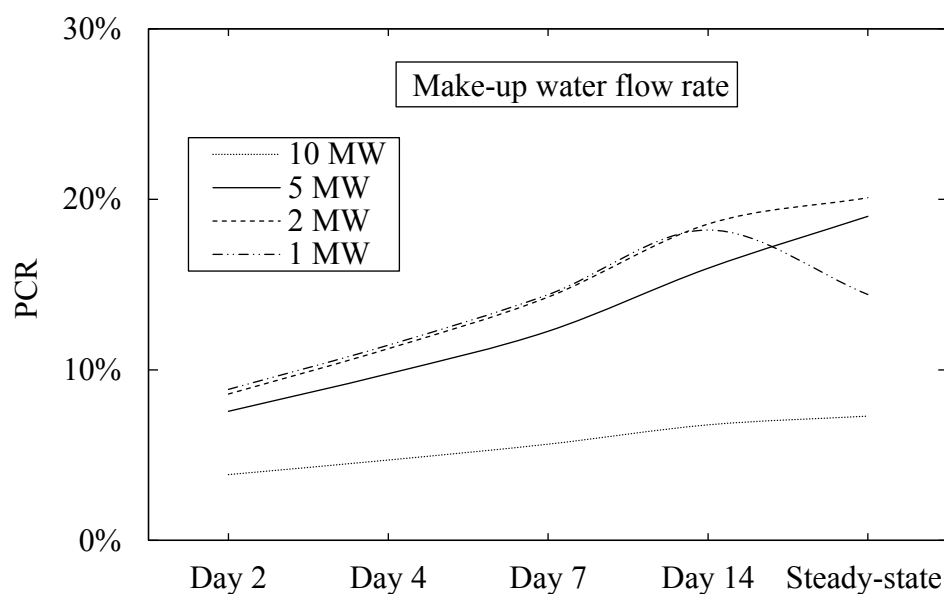


Figure 8.18: Effect of heat load on the PCR of the make-up water flow rate.

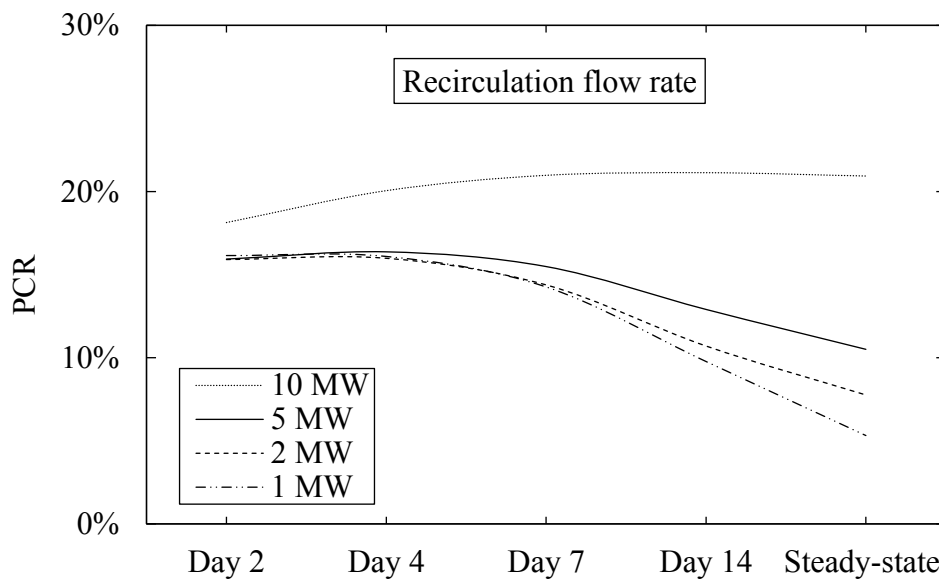


Figure 8.19: Effect of heat load on the PCR of the recirculation flow rate.

### 8.3.3 Recommendations based on ANOVA results

The outcomes from ANOVA can be concluded in term of recommendations that may be able to aid the organisation to manage their cooling pond more efficiently. These recommendations may be only valid for the range of the configurations considered in this study. A description of the loss of cooling scenario and its consequences are shown in Figure 8.20. Additionally, some recommendations during the recovery from an accident scenario are also given in Figure 8.20.

Generally, the difference between the contributions of the ventilation system and make-up water to the overall cooling is not very big, except in the very first few days of the recovery process. During the very first few days, the cooling by means of ventilation is more effective choice compared to the make-up water. However, as the time advances, ventilation and make-up water start to swap positions but this only for low and intermediate heat load values. For high heat load values, the cooling provided by ventilation is more effective than the cooling by make-up water.

From the point of view thermal performance, when recovering from a loss of cooling scenario, it is recommended that the first cooling mechanism to be recovered is the recirculation cooling, for all of the reported values of heat load.

However, in some occasions, the pond can suffer from a rapid loss of cooling water. This is when the generated heat from the fuel rods is large enough to causes the water to boil very quickly and evaporate at high rates. [REDACTED]

[REDACTED]. In such situations, recovering the supply of the make-up water is the best choice in order to prevent the fuel assemblies of being exposed to the ambient air.

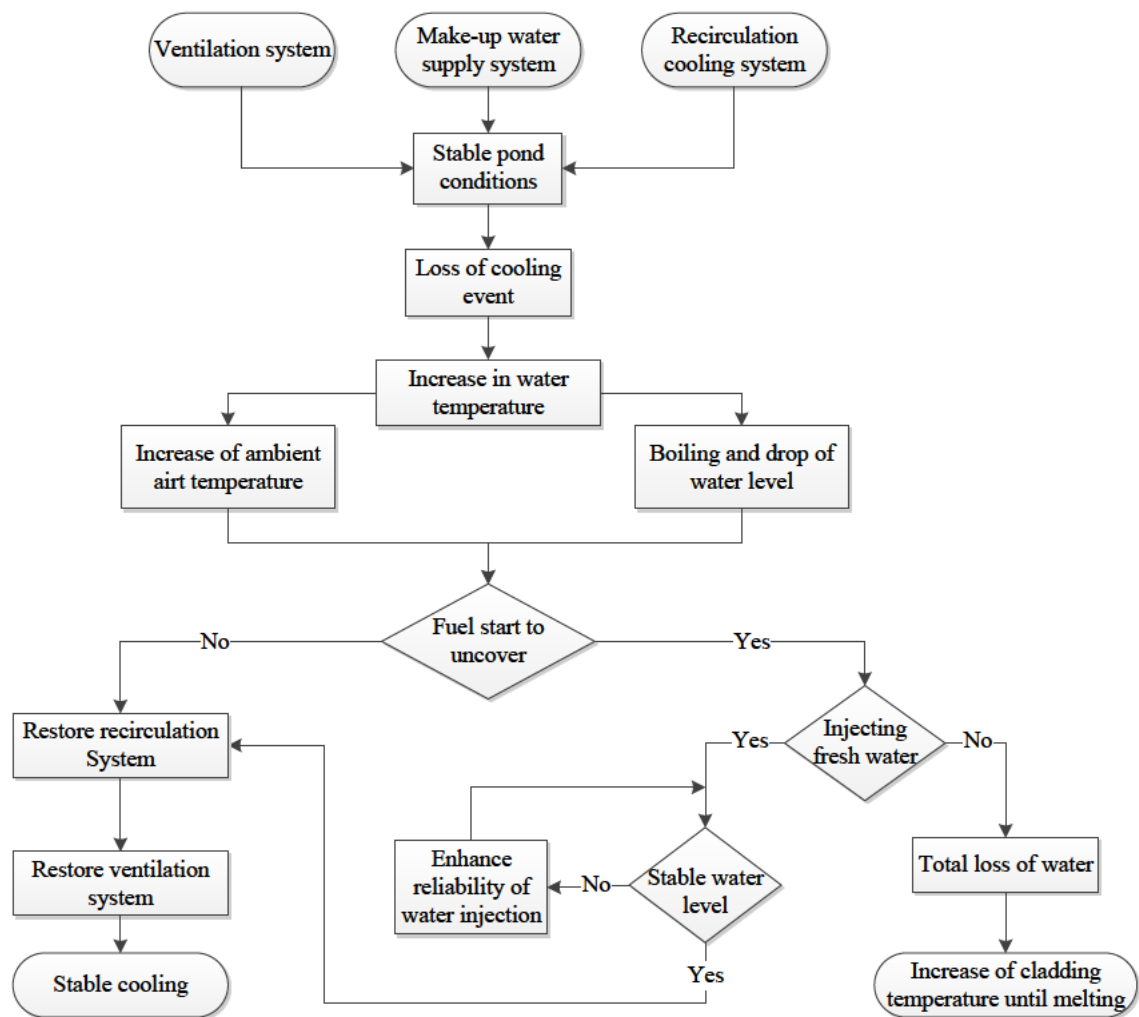


Figure 8.20: Illustration of the main events during the loss of cooling scenario and recommended reactions to be taken.

## **8.4 Summary**

A number of studies were performed to analyse the performance of the SNF cooling pond at the Sellafield site using the spreadsheet model. These studies are: analysis of the pond thermal behaviour of the pond and a sensitivity study.

In the analysis of the thermal behaviour, the first analysis concerned the performance of the pond under normal operating conditions where the pond water and air temperatures are evaluated considering that the pond is loaded with the maximum possible heat load. In the same study, the proportions of heat removal components were quantified. In addition, a loss of cooling analysis was conducted under two water surface conditions; one when the surface heat transfer is disabled, and another when it is taken into consideration. It was found that the assumption leading to ignoring the heat loss from the water surface is not always a good choice.

Further analysis was conducted in order to estimate the rate of temperature increase per day. It was found that the rate of temperature increase per day increases with the heat load and addition of every 1 MW causes an increase by less than 1 °C/day. The last study was performed to examine the sensitivity of the pond water temperature to variation in outside weather conditions. The outcomes reveal that water temperature is rather insensitive to the outside relative humidity. On the other hand, relatively high sensitivity was observed to variations in outside temperature.

In the sensitivity study, the Taguchi method and the statistical method of ANOVA were used to assess the influence of the input parameters on the spreadsheet model's predictions, and hence, the cooling performance of the cooling pond. The ANOVA results reveal that the efficiency of the cooling tower is the most influential parameter on the cooling performance of the SNF cooling pond within the considered values of heat load. It was also confirmed that the effect of the outside air relative humidity is not significant. However, the indoor relative humidity still plays a big role on the evaporation rate as well as the overall performance of the pond.

## Chapter 9 Conclusion and Recommendations for Future Work

### 9.1 Conclusion

The literature review showed the relevance of developing accurate and feasible models for investigating thermal-hydraulic behaviours of SNF cooling ponds during normal operating conditions as well as the loss of cooling scenarios. Most of the reported studies focused on investigations of the severe accident scenarios. On the other hand, none of the studies has investigated the thermal performance of the spent fuel cooling pond during the normal operating conditions to understand the effect of each of the cooling systems. Furthermore, all of the spent fuel cooling ponds that have been considered are of a relatively small size. However, due to the continued increase in spent fuel production, some countries have constructed centralised ponds to keep up with the incoming spent fuel until a more permanent solution is found. To the best of our knowledge, through investigation of centralised large-scale ponds have not reported before, which may be partially due to security concerns and the commercially sensitive nature of the work.

Treatment of the boundary conditions at the free water surface was achieved by analytically modelling of the heat transfer component and developing an expression for the overall heat transfer coefficient,  $h_{overall}$ , as a function of the surface temperature. The evaporation rate was expressed via the definition of Stefan's law to take into account the advection. The modelling methodology was numerically validated against experimental data of the cooling process of water which was reported by Bower et al. [82]. The advantage of the proposed modelling methodology is that it allows simulating the heat loss from water surface due to evaporation without the need to use the multiphase models with reasonable accuracy.

A spreadsheet model of the cooling pond is proposed based on the well-mixed assumption. The main modes of heat transfer processes within the pond installation were considered in this model where the ventilation system is also incorporated. The proposed



model was validated against reliable data reported in the literature for the Maine Yankee cooling pond as well as some measurements from the Sellafield site. This allowed testing the performance of the spreadsheet under various operational scenarios and different pond sizes. During the validation, unlike the typical ponds considered in the literature, the heat loss from the water surface in Sellafield's pond was dominant. The advantage of the spreadsheet model is that it is able to provide very quick answers for "what-if" scenarios, which is required at the decision-making stage to aid the organisation in the operation of their cooling ponds more efficiently.

A CFD model was developed for Sellafield's cooling pond considering the water zone only. This model was coupled with the spreadsheet model to introduce the humid air zone and the ventilation system to the CFD model in terms of heat transfer coefficient at the water surface. The fuel assemblies were approximated to porous medium with a volumetric heat source. The CFD model was validated against temperature measurements that were collected from the site. Besides, the transient results of the numerical model were verified by comparing the rate of temperature increase with its counterpart from the spreadsheet model. After that, a parametric study was conducted by varying the heat load distribution and the flow rates of the make-up water and recirculation. It was found that the distribution of the water temperature is not very sensitive to the recirculation flow rate while a relatively higher sensitivity was observed to the location of the fuel. Generally, the temperature variation within water was relatively small as the maximum difference between the average and peak values was about 3.8 °C, except in some locations near to the inlet pond where larger variations were observed. This confirms the reliability of the well-mixed hypothesis that was adopted in the spreadsheet model.

A numerical simulation was conducted for heated vertical cylinder submerged in a water tank and the obtained data were validated against the experimental data reported by Kimura et al. [103]. The CFD model was able to predict the temperature distribution along the heated surface of the cylinder and locating the flow separation point with good accuracy. The predicted results showed sensitivity to various eddy viscosity models where *Transition SST* model was the only model, amongst the selected models able to capture the transition region with good accuracy.

A CFD model of the fuel assemblies was developed where the knowledge gained from the modelling of the vertical cylinder was partially implemented. The fluid flow and heat transfer characteristics were established. The results showed that the water contained in the regions between the racks and the fuel cans is almost stagnant and the highest temperatures were recorded in the same regions. A parametric study was conducted by varying the pond temperature and the heat flux to determine the maximum temperature within the rack. As a result, a correlation for the temperature difference, between the maximum and pond, was proposed as a function of the heat flux.

The proposed spreadsheet model was used to perform a range of studies on the pond performance. The first study evaluated the pond thermal behaviour when the pond is loaded with the maximum possible heat load. Another study has concerned the loss of cooling scenario and the effect of the assumption of neglecting the heat loss from the water surface. It was found that such an assumption was not applicable for low values of heat load. It was also found that the pond would take about one week to reach the boiling point and further one month for the fuel assembly to uncover. The last study was conducted using Taguchi and ANOVA statistical methods to assess the influence of the input parameters on the pond cooling performance. The ANOVA results reveal that the efficiency of the cooling tower is the most influential parameter on the cooling performance under the considered values of heat load. It was also confirmed that the effect of the outside air relative humidity is not very significant. However, the indoor relative humidity still plays a big role in establishing the evaporation rate from the water surface, and hence the cooling performance.

## **9.2 Future work**

- An analytical model for the fuel cladding would be useful to evaluate the maximum cladding temperature and can be also introduced to the spreadsheet model.
- [REDACTED]  
[REDACTED]  
[REDACTED]  
[REDACTED]



## References

- [1] G. Recktenwald and M. Deinert, "Cost probability analysis of reprocessing spent nuclear fuel in the US," *Energy Economics*, vol. 34, pp. 1873-1881, 2012.
- [2] P. L. Joskow and J. E. Parsons, "The future of nuclear power after Fukushima," 2012.
- [3] S.-i. Tanaka, "Accident at the Fukushima Daiichi nuclear power stations of TEPCO: outline & lessons learned," *Proceedings of the Japan Academy, Series B*, vol. 88, pp. 471-484, 2012.
- [4] *Institute for Nuclear Power Operations (INPO). (November, 2011). Special Report on the Nuclear Accident at the Fukushima Daiichi Nuclear Power Station. Accessed 20 February 2015. Available:*  
<https://www.nrc.gov/docs/ML1134/ML11347A454.pdf>
- [5] Y. V. Kozlov, V. Safutin, N. Tikhonov, A. Tokarenko, and V. Spichev, "Long-term storage and shipment of spent nuclear fuel," *Atomic Energy*, vol. 89, pp. 792-803, 2000.
- [6] A. Jenkins, Submerged water jet decontamination of multi-element bottles, in WM2011 Conference. 2011: Phoenix, Arizona. p. 9.
- [7] B. Y. Moratilla Soria, M. Uris Mas, M. Estadieu, A. Villar Lejarreta, and D. Echevarria-López, "Recycling versus long-term storage of nuclear fuel: economic factors," *Science and Technology of Nuclear Installations*, vol. 2013, 2013.
- [8] K. Fukuda, W. Danker, J. Lee, A. Bonne, and M. Crijns, "IAEA Overview of global spent fuel storage," *Storage of spent fuel from Power Reactors, C&S Paper Series*, 2003.
- [9] B. Zohuri and N. Fathi, *Thermal-hydraulic analysis of nuclear reactors*: Springer, 2015.

- 
- [10] W. Kuo, G. Yun, and Z. He-yi, "Spent fuel pool transient analysis under accident case and the flow establishment process of passive cooling system," in *Information Systems for Crisis Response and Management (ISCRAM), 2011 International Conference on*, 2011, pp. 482-491.
- [11] UK Government. (September 15, 2016). *Government confirms Hinkley Point C project following new agreement in principle with EDF*. Accessed 10 Januray 2017. Available: <https://www.gov.uk/government/news/government-confirms-hinkley-point-c-project-following-new-agreement-in-principle-with-edf>
- [12] S. Glasstone and A. Sesonske, "Nuclear reactor engineering: Reactor systems engineering. Volume Two," 1994.
- [13] W. J. Garland, "Decay heat estimates for MNR," *McMaster Nuclear Reactor, McMaster University, Ontario*, 1999.
- [14] H. Feiveson, Z. Mian, M. Ramana, and F. von Hippel, "Managing Spent Fuel from Nuclear Power Reactors Experience and Lessons from Around the World," *International Panel on Fissile Materials*, 2011.
- [15] *Sellafield Ltd. Ongoing Receipt of AGR Fuel*. Accessed 20 May 2016. Available: <http://www.sellafieldsites.com/solution/spent-fuel-management/ongoing-receipt-of-agr-fuel/>
- [16] H. K. Versteeg and W. Malalasekera, *An introduction to computational fluid dynamics: the finite volume method*: Pearson Education, 2007.
- [17] ANSYS, "Fluent Theory and Guide," 2016.
- [18] Y. Morino, T. Ohara, and M. Nishizawa, "Atmospheric behavior, deposition, and budget of radioactive materials from the Fukushima Daiichi nuclear power plant in March 2011," *Geophysical research letters*, vol. 38, 2011.
- [19] Y. Masumoto, Y. Miyazawa, D. Tsumune, T. Tsubono, T. Kobayashi, H. Kawamura, *et al.*, "Oceanic dispersion simulations of <sup>137</sup>Cs released from the Fukushima Daiichi nuclear power plant," *Elements*, vol. 8, pp. 207-212, 2012.
-

- 
- [20] H. Kawamura, T. Kobayashi, A. Furuno, T. In, Y. Ishikawa, T. Nakayama, *et al.*, "Preliminary numerical experiments on oceanic dispersion of  $^{131}\text{I}$  and  $^{137}\text{Cs}$  discharged into the ocean because of the Fukushima Daiichi nuclear power plant disaster," *Journal of Nuclear Science and Technology*, vol. 48, pp. 1349-1356, 2011.
- [21] T. Takemura, H. Nakamura, M. Takigawa, H. Kondo, T. Satomura, T. Miyasaka, *et al.*, "A numerical simulation of global transport of atmospheric particles emitted from the Fukushima Daiichi Nuclear Power Plant," *Sola*, vol. 7, pp. 101-104, 2011.
- [22] L. E. Herranz, J. Penalva, and F. Fera, "CFD analysis of a cask for spent fuel dry storage: Model fundamentals and sensitivity studies," *Annals of Nuclear Energy*, vol. 76, pp. 54-62, 2015.
- [23] X. Heng, G. Zuying, and Z. Zhiwei, "A numerical investigation of natural convection heat transfer in horizontal spent-fuel storage cask," *Nuclear Engineering and Design*, vol. 213, pp. 59-65, 2002.
- [24] S. H. Yoo, H. C. No, H. M. Kim, and E. H. Lee, "CFD-assisted scaling methodology and thermal-hydraulic experiment for a single spent fuel assembly," *Nuclear Engineering and Design*, vol. 240, pp. 4008-4020, 2010.
- [25] S. H. Yoo, H. C. No, H. M. Kim, and E. H. Lee, "Full-scope simulation of a dry storage cask using computational fluid dynamics," *Nuclear Engineering and Design*, vol. 240, pp. 4111-4122, 2010.
- [26] K. Bang, J. Lee, J. Seo, and K. Seo, "Heat transfer performance tests using a half scale horizontal storage module," *Nuclear Engineering and Design*, vol. 240, pp. 4123-4127, 2010.
- [27] D.-G. Lee, J.-H. Park, Y.-H. Lee, C.-Y. Baeg, and H.-J. Kim, "Natural convection heat transfer characteristics in a canister with horizontal installation of dual purpose cask for spent nuclear fuel," *Nuclear Engineering and Technology*, vol. 45, pp. 969-978, 2013.
-

- 
- [28] D. Kim, S.-J. Yook, and K.-S. Lee, "Investigation of radiative and convective heat transfer in storage vaults for improving space efficiency," *International Journal of Heat and Mass Transfer*, vol. 80, pp. 301-308, 1// 2015.
- [29] D. Kim, S.-J. Yook, K.-S. Lee, S.-H. Yu, and K.-s. Bang, "Scaling method for storage vaults based on thermal-hydraulic characteristics," *Nuclear Engineering and Design*, vol. 275, pp. 242-248, 2014.
- [30] Y.-S. Tseng, J.-R. Wang, F. P. Tsai, Y.-H. Cheng, and C. Shih, "Thermal design investigation of a new tube-type dry-storage system through CFD simulations," *Annals of Nuclear Energy*, vol. 38, pp. 1088-1097, 2011.
- [31] J. Lee, W. Choi, K. Bang, K. Seo, and S. Yoo, "Thermal-fluid flow analysis and demonstration test of a spent fuel storage system," *Nuclear Engineering and Design*, vol. 239, pp. 551-558, 2009.
- [32] H. Kim, O. J. Kwon, G.-U. Kang, and D.-G. Lee, "Comparisons of prediction methods for peak cladding temperature and effective thermal conductivity in spent fuel assemblies of transportation/storage casks," *Annals of Nuclear Energy*, vol. 71, pp. 427-435, 2014.
- [33] J.-H. Ko, J.-H. Park, I.-S. Jung, G.-U. Lee, C.-Y. Baeg, and T.-M. Kim, "Shielding analysis of dual purpose casks for spent nuclear fuel under normal storage conditions," *Nuclear Engineering and Technology*, vol. 46, pp. 547-556, 2014.
- [34] Y. S. Jeong and I. C. Bang, "Hybrid heat pipe based passive cooling device for spent nuclear fuel dry storage cask," *Applied Thermal Engineering*, vol. 96, pp. 277-285, 2016.
- [35] T.-C. Hung, V. K. Dhir, B.-S. Pei, Y.-S. Chen, and F. P. Tsai, "The development of a three-dimensional transient CFD model for predicting cooling ability of spent fuel pools," *Applied Thermal Engineering*, vol. 50, pp. 496-504, 2013.
- [36] C. Ye, M. Zheng, M. Wang, R. Zhang, and Z. Xiong, "The design and simulation of a new spent fuel pool passive cooling system," *Annals of Nuclear Energy*, vol. 58, pp. 124-131, 2013.
-

- 
- [37] Z. Xiong, C. Ye, M. Wang, and H. Gu, "Experimental study on the sub-atmospheric loop heat pipe passive cooling system for spent fuel pool," *Progress in Nuclear Energy*, vol. 79, pp. 40-47, 2015.
- [38] C. Yanagi, M. Murase, Y. Yoshida, T. Iwaki, and T. Nagae, "Evaluation of heat loss and water temperature in a spent fuel pit," *Journal of Power and Energy Systems*, vol. 6, pp. 51-62, 2012.
- [39] C. Yanagi, M. Murase, Y. Yoshida, Y. Utanohara, T. Iwaki, and T. Nagae, "Numerical Simulation of Water Temperature in a Spent Fuel Pit during the Shutdown of Its Cooling Systems," *Journal of Power and Energy Systems*, vol. 6, pp. 423-434, 2012.
- [40] S. Chen, W. Lin, Y. Ferng, C. Chieng, and B. Pei, "Development of 3-D CFD methodology to investigate the transient thermal-hydraulic characteristics of coolant in a spent fuel pool," *Nuclear Engineering and Design*, vol. 275, pp. 272-280, 2014.
- [41] S. W. Churchill and H. H. Chu, "Correlating equations for laminar and turbulent free convection from a vertical plate," *International journal of heat and mass transfer*, vol. 18, pp. 1323-1329, 1975.
- [42] K.-I. Ahn, J.-U. Shin, and W.-T. Kim, "Severe accident analysis of plant-specific spent fuel pool to support a SFP risk and accident management," *Annals of Nuclear Energy*, vol. 89, pp. 70-83, 2016.
- [43] R. Gauntt, R. Cole, S. Hodge, S. Rodriguez, R. Sanders, R. Smith, *et al.*, "MELCOR computer code manuals," *Sandia National Laboratories, NUREG/CR*, vol. 6119, 2000.
- [44] Y.-S. Chen and Y.-R. Yuann, "Accident mitigation for spent fuel storage in the upper pool of a Mark III containment," *Annals of Nuclear Energy*, vol. 91, pp. 156-164, 2016.
- [45] S. Carlos, F. Sanchez-Saez, and S. Martorell, "Use of TRACE best estimate code to analyze spent fuel storage pools safety," *Progress in Nuclear Energy*, vol. 77, pp. 224-238, 11// 2014.
-



- 
- [46] R. Gay and D. Gloski, "Verification of the GFLOW computer code using experimental data from the Maine Yankee spent-fuel storage pool. Final report," NUS Corp., Menlo Park, CA (USA)1983.
- [47] V. Ognerubov, A. Kaliatka, and V. Vileiniškis, "Features of modelling of processes in spent fuel pools using various system codes," *Annals of Nuclear Energy*, vol. 72, pp. 497-506, 2014.
- [48] P. Groudev, A. Stefanova, and M. Manolov, "Investigation of dry out of SFP for VVER440/V230 at Kozloduy NPP," *Nuclear Engineering and Design*, vol. 262, pp. 285-293, 2013.
- [49] X. Wu, W. Li, Y. Zhang, W. Tian, G. Su, and S. Qiu, "Analysis of the loss of pool cooling accident in a PWR spent fuel pool with MAAP5," *Annals of Nuclear Energy*, vol. 72, pp. 198-213, 2014.
- [50] H. Wang, L. Ge, J. Shan, J. Gou, and B. Zhang, "Safety Analysis of CPR1000 Spent Fuel Pool in Case of Loss of Heat Sink," in *2013 21st International Conference on Nuclear Engineering*, 2013, pp. V004T09A096-V004T09A096.
- [51] W. Fu, X. Li, X. Wu, and Z. Zhang, "Investigation of a long term passive cooling system using two-phase thermosyphon loops for the nuclear reactor spent fuel pool," *Annals of Nuclear Energy*, vol. 85, pp. 346-356, 2015.
- [52] A. Kaliatka, V. Ognerubov, V. Vileiniškis, and E. Ušpuras, "Analysis of the processes in spent fuel pools in case of loss of heat removal due to water leakage," *Science and Technology of Nuclear Installations*, vol. 2013, 2013.
- [53] A. Kaliatka, V. Ognerubov, and V. Vileiniskis, "Analysis of the processes in spent fuel pools of Ignalina NPP in case of loss of heat removal," *Nuclear Engineering and Design*, vol. 240, pp. 1073-1082, 2010.
- [54] J. R. Wang, H. T. Lin, Y. S. Tseng, and C. K. Shih, "Application of TRACE and CFD in the spent fuel pool of Chinshan nuclear power plant," in *Applied Mechanics and Materials*, 2012, pp. 78-82.
-

- 
- [55] D. Grgić, R. Ječmenica, and D. Pevec, "Thermal-hydraulic modeling of reracked spent fuel pool," in *International Conference Nuclear Energy in Central Europe 2000*, 2000.
- [56] CD-adapco, "STAR-CCM+ User Guide 6.02," *CD-adapco, Melville, NY*, 2011.
- [57] T. George, S. Claybrook, L. Wiles, and C. Wheeler, "GOTHIC Containment Analysis Package, User Manual, Version 7.2 b, NAI 8907-02 Rev 18," 2009.
- [58] U. N. R. Commission, "TRACE V5. 0 User Manual," *Division of Risk Assessment and Special Projects, Office of Nuclear Regulatory Research, Washington, DC*, 2010.
- [59] C. Allison and R. Wagner, "RELAP5/SCDAPSIM/MOD3. 2 (am+) Input Manual Supplemental," *Innovative Systems Software, LLC*, 2001.
- [60] K. Trambauer, C. Bals, J. Schubert, and H. Austregesilo, "ATHLET-CD Mod. 2.2–Cycle A (Update 1)–User’s Manual," GRS-P-42009.
- [61] K. Carlson, R. Riemke, S. Rouhani, R. Shumway, and W. Weaver, "RELAP5/MOD3 Code Manual Volume I: Code Structure, System Models and Solution Methods," *US NRC NUREG/CR-5535, Washington (DC, USA) June*, 1990.
- [62] R. Henry, "MAAP5–Modular Accident Analysis Program for LWR Power Plants, User’s Manual, Fauske and Associates Inc.," 2008.
- [63] C. Fletcher and R. Schultz, "RELAP5/MOD3 Code Manual Volume V: User’s Guidelines," *Idaho National Engineering Laboratory, Lockheed Idaho Technologies Company, Idaho Falls, Idaho*, vol. 83415, 1995.
- [64] J. Van Dorsselaere, C. Seropian, P. Chatelard, F. Jacq, J. Fleurot, P. Giordano, *et al.*, "The ASTEC integral code for severe accident simulation," *Nuclear Technology*, vol. 165, pp. 293-307, 2009.
- [65] T. L. George, "Gothic Containment Analysis Package User Manual," *Version*, vol. 4, pp. 8907-02, 1993.
-

- 
- [66] E. Sartori, "A critical review on equations employed for the calculation of the evaporation rate from free water surfaces," *Solar energy*, vol. 68, pp. 77-89, 2000.
- [67] M. Silberberg, *Chemistry: The Molecular Nature of Matter and Change*, 4th ed.: McGraw-Hill, 2006.
- [68] R. D. Thompson, *Atmospheric processes and systems*: Psychology Press, 1998.
- [69] F. C. McQuiston, J. D. Parker, and J. D. Spitler, *Heating, ventilating, and air conditioning: analysis and design*. Chichester: Wiley, 2005.
- [70] N. A. Vinnichenko, A. V. Uvarov, D. A. Vetukov, and Y. Y. Plaksina, "Direct computation of evaporation rate at the surface of swimming pool," ed, 2011, pp. 120-124.
- [71] G. B. Magin and L. E. Randall, *Review of literature on evaporation suppression*: US Government Printing Office, 1960.
- [72] E. E. Adams, D. J. Cosler, and K. R. Helfrich, "Evaporation from heated water bodies: predicting combined forced plus free convection," *Water resources research*, vol. 26, pp. 425-435, 1990.
- [73] E. Shaw, "Hydrology in practice 3rd ed," *Stanley Thornes Pub, UK pp569*, 1998.
- [74] P. Bansal and G. Xie, "A unified empirical correlation for evaporation of water at low air velocities," *International communications in heat and mass transfer*, vol. 25, pp. 183-190, 1998.
- [75] M. Lurie and N. Michailoff, "Evaporation from free water surface," *Industrial & Engineering Chemistry*, vol. 28, pp. 345-349, 1936.
- [76] R. Tang and Y. Etzion, "Comparative studies on the water evaporation rate from a wetted surface and that from a free water surface," *Building and Environment*, vol. 39, pp. 77-86, 2004.
- [77] R. Almanza and J. Lara, "Energy requirements for a swimming pool through a water-atmosphere energy balance," *Solar Energy*, vol. 53, pp. 37-39, 1994.
-

- 
- [78] C. C. Smith, G. Löf, and R. Jones, "Measurement and analysis of evaporation from an inactive outdoor swimming pool," *Solar Energy*, vol. 53, pp. 3-7, 1994.
- [79] M. Shah, "Rate of evaporation from undisturbed water pools to quiet air: evaluation of available correlations," *International Journal of HVAC&R Research*, vol. 8, pp. 125-131, 2002.
- [80] P. Mirza Mohammed Shah PhD, "New correlation for prediction of evaporation from occupied swimming pools," *ASHRAE Transactions*, vol. 119, p. 450, 2013.
- [81] T. Yamaji, T. Hirota, Y. Koizumi, and M. Murase, "Study on Heat Transfer From Hot Water to Cold Air With Evaporation," in *ASME 2013 International Mechanical Engineering Congress and Exposition*, 2013, pp. V08CT09A035-V08CT09A035.
- [82] S. Bower and J. Saylor, "A study of the Sherwood–Rayleigh relation for water undergoing natural convection-driven evaporation," *International Journal of Heat and Mass Transfer*, vol. 52, pp. 3055-3063, 2009.
- [83] E. Sparrow, G. Kratz, and M. Schuerger, "Evaporation of water from a horizontal surface by natural convection," *Journal of heat transfer*, vol. 105, pp. 469-475, 1983.
- [84] L. Boelter, H. Gordon, and J. Griffin, "Free evaporation into air of water from a free horizontal quiet surface," *Industrial & Engineering Chemistry*, vol. 38, pp. 596-600, 1946.
- [85] B. Sharpley and L. Boelter, "Evaporation of water into quiet air from a one-foot diameter surface," *Industrial & Engineering Chemistry*, vol. 30, pp. 1125-1131, 1938.
- [86] J. Lloyd and W. Moran, "Natural convection adjacent to horizontal surface of various planforms," *Journal of Heat Transfer*, vol. 96, pp. 443-447, 1974.
- [87] R. Goldstein, E. Sparrow, and D. Jones, "Natural convection mass transfer adjacent to horizontal plates," *International Journal of Heat and Mass Transfer*, vol. 16, pp. 1025-1035, 1973.
-

- 
- [88] S. Bower and J. Saylor, "Sherwood–Rayleigh parameterization for evaporation in the presence of surfactant monolayers," *AIChE Journal*, vol. 59, pp. 303-315, 2013.
- [89] S. Bower, "An investigation of the effects of surfactant monolayers on natural convection heat transfer and evaporative mass transfer," PhD, Mechanical Engineering, Clemson University, 2011.
- [90] A. Jodat, M. Moghiman, and E. Y. Rad, "An Experimental Study of the Ability of Similarity Theory to predict Water Evaporation Rate for Different Convection Regimes," *Arabian Journal for Science and Engineering*, vol. 38, pp. 3505-3513, 2013.
- [91] T. Cebeci, "Laminar-free-convective-heat transfer from the outer surface of a vertical slender circular cylinder," in *Heat transfer 1974; Proceedings of the Fifth International Conference, Tokyo, Volume 3*, 1974, pp. 15-19.
- [92] A. Bejan, *Convection heat transfer*: John wiley & sons, 2013.
- [93] F. Godaux and B. Gebhart, "An experimental study of the transition of natural convection flow adjacent to a vertical surface," *International Journal of Heat and Mass Transfer*, vol. 17, pp. 93-107, 1974.
- [94] R. Mahajan and B. Gebhart, "An experimental determination of transition limits in a vertical natural convection flow adjacent to a surface," *Journal of Fluid Mechanics*, vol. 91, pp. 131-154, 1979.
- [95] Y. Jaluria and B. Gebhart, "On transition mechanisms in vertical natural convection flow," *Journal of Fluid Mechanics*, vol. 66, pp. 309-337, 1974.
- [96] B. Gebhart, Y. Jaluria, R. L. Mahajan, and B. Sammakia, "Buoyancy-induced flows and transport," 1988.
- [97] P. Lykoudis, "Criteria for predicting the transition to turbulence in natural convection along a vertical surface," *Journal of heat transfer*, vol. 116, p. 633, 1994.
-

- 
- [98] T. L. Bergman and F. P. Incropera, *Fundamentals of heat and mass transfer*: John Wiley & Sons, 2011.
- [99] J. Holman, "Heat Transfer of International Edition," ed: McGraw-Hill, New York, 2009.
- [100] T. Fujii, M. Takeuchi, M. Fujii, K. Suzaki, and H. Uehara, "Experiments on natural-convection heat transfer from the outer surface of a vertical cylinder to liquids," *International Journal of Heat and Mass Transfer*, vol. 13, pp. 753IN1771-770IN4787, 1970.
- [101] J.-M. Buchlin, "Natural and forced convective heat transfer on slender cylinders," *Revue générale de Thermique*, vol. 37, pp. 653-660, 1998.
- [102] M. Al-Arabi and M. Khamis, "Natural convection heat transfer from inclined cylinders," *International Journal of Heat and Mass Transfer*, vol. 25, pp. 3-15, 1982.
- [103] F. Kimura, T. Tachibana, K. Kitamura, and T. Hosokawa, "Fluid flow and heat transfer of natural convection around heated vertical cylinders (effect of cylinder diameter)," *JSME International Journal Series B Fluids and Thermal Engineering*, vol. 47, pp. 156-161, 2004.
- [104] T. FUJII, "Experimental studies of free convection heat transfer," *Bulletin of JSME*, vol. 2, pp. 555-558, 1959.
- [105] M. Arshad, M. H. Inayat, and I. R. Chughtai, "Experimental study of natural convection heat transfer from an enclosed assembly of thin vertical cylinders," *Applied Thermal Engineering*, vol. 31, pp. 20-27, 2011.
- [106] H. Nagendra, M. Tirunarayanan, and A. Ramachandran, "Laminar free convection from vertical cylinders with uniform heat flux," *Journal of Heat Transfer*, vol. 92, pp. 191-194, 1970.
- [107] G.-U. Kang, B.-J. Chung, and H.-J. Kim, "Natural convection heat transfer on a vertical cylinder submerged in fluids having high Prandtl number," *International Journal of Heat and Mass Transfer*, vol. 79, pp. 4-11, 2014.
-

- 
- [108] H. Nagendra, M. Tirunarayanan, and A. Ramachandran, "Free convection heat transfer from vertical cylinders and wires," *Chemical Engineering Science*, vol. 24, pp. 1491-1495, 1969.
- [109] T. Chen and B. Armaly, "Natural convection along slender vertical cylinders with variable surface temperature," *Journal of heat transfer*, vol. 110, p. 103, 1988.
- [110] F. Tetsu and U. Haruo, "Laminar natural-convective heat transfer from the outer surface of a vertical cylinder," *International Journal of Heat and Mass Transfer*, vol. 13, pp. 607-615, 1970.
- [111] C. Popiel, J. Wojtkowiak, and K. Bober, "Laminar free convective heat transfer from isothermal vertical slender cylinder," *Experimental Thermal and Fluid Science*, vol. 32, pp. 607-613, 2007.
- [112] C. M. Lee and K. Lee, "A study on operation time periods of spent fuel interim storage facilities in South Korea," *Progress in Nuclear Energy*, vol. 49, pp. 323-333, 2007.
- [113] K. A. Rogers, "Fire in the hole: A review of national spent nuclear fuel disposal policy," *Progress in Nuclear Energy*, vol. 51, pp. 281-289, 2009.
- [114] A. J. Chorin, "Numerical solution of the Navier-Stokes equations," *Mathematics of computation*, vol. 22, pp. 745-762, 1968.
- [115] R. Deissler, "Derivation of the Navier–Stokes equation," *American Journal of Physics*, vol. 44, pp. 1128-1130, 1976.
- [116] T. Cebeci, J. P. Shao, F. Kafyeke, and E. Laurendeau, *Computational fluid dynamics for engineers*: Springer Berlin Heidelberg, 2005.
- [117] J. D. Anderson and J. Wendt, *Computational fluid dynamics* vol. 206: Springer, 1995.
- [118] G. Nardini and M. Paroncini, "Heat transfer experiment on natural convection in a square cavity with discrete sources," *Heat and Mass Transfer*, vol. 48, pp. 1855-1865, 2012.
-

- 
- [119] D. C. Wilcox, *Turbulence modeling for CFD* vol. 2: DCW industries La Canada, CA, 1998.
- [120] F. R. Menter, "Two-equation eddy-viscosity turbulence models for engineering applications," *AIAA journal*, vol. 32, pp. 1598-1605, 1994.
- [121] A.-J. N. Khalifa, "Natural convective heat transfer coefficient—a review: I. Isolated vertical and horizontal surfaces," *Energy conversion and management*, vol. 42, pp. 491-504, 2001.
- [122] I. Shyha, S. Gariani, and M. Bhatti, "Investigation of cutting tools and working conditions effects when cutting Ti-6Al-4V using vegetable oil-based cutting fluids," *Procedia Engineering*, vol. 132, pp. 577-584, 2015.
- [123] S. Debnath, M. M. Reddy, and Q. S. Yi, "Influence of cutting fluid conditions and cutting parameters on surface roughness and tool wear in turning process using Taguchi method," *Measurement*, vol. 78, pp. 111-119, 2016.
- [124] S. Chamoli, "A Taguchi approach for optimization of flow and geometrical parameters in a rectangular channel roughened with V down perforated baffles," *Case Studies in Thermal Engineering*, vol. 5, pp. 59-69, 2015.
- [125] M. Zeng, L. Tang, M. Lin, and Q. Wang, "Optimization of heat exchangers with vortex-generator fin by Taguchi method," *Applied Thermal Engineering*, vol. 30, pp. 1775-1783, 2010.
- [126] G. Taguchi, S. Chowdhury, and Y. Wu, *Taguchi's quality engineering handbook*: Wiley Online Library, 2005.
- [127] W. Penny and R. Henson, "Analysis of variance," *Statistical parametric mapping: The analysis of functional brain images*, pp. 166-177, 2006.
- [128] T. A. Ryan, B. L. Joiner, and B. F. Ryan, *Minitab™*: Wiley Online Library, 2004.
- [129] Y. Cengel, *Heat Transfer A Practical Approach*, McGraw-Hill, 2 ed., 2003.
- [130] T. L. Bergman, F. P. Incropera, D. P. DeWitt, and A. S. Lavine, *Fundamentals of heat and mass transfer*: John Wiley & Sons, 2011.
-



- 
- [131] R. J. LeVeque, *Finite difference methods for ordinary and partial differential equations: steady-state and time-dependent problems* vol. 98: Siam, 2007.
- [132] C. Siechert and E. Bott, *Microsoft® Office 2010 Inside Out*: Microsoft Press, 2010.
- [133] B. R. Hunt, R. L. Lipsman, and J. M. Rosenberg, *A guide to MATLAB: for beginners and experienced users*: Cambridge University Press, 2014.
- [134] L. D. Berman, *Evaporative cooling of circulating water*: Pergamon press, 1961.
- [135] A. C. Yunus and A. B. Michael, "Thermodynamics: An engineering approach," *McGraw-Hill, New York*, 2006.
- [136] J. D. Hoffman and S. Frankel, *Numerical methods for engineers and scientists*: CRC press, 2001.
- [137] F. Menter, R. Langtry, and S. Völker, "Transition modelling for general purpose CFD codes," *Flow, Turbulence and Combustion*, vol. 77, pp. 277-303, 2006.
- [138] T. Fujii, M. Takeuchi, M. Fujii, K. Suzaki, and H. Uehara, "Experiments on natural-convection heat transfer from the outer surface of a vertical cylinder to liquids," *International Journal of Heat and Mass Transfer*, vol. 13, pp. 753-787, 1970.
- [139] T. P. Majchrowski, "Chemical behaviour of a nuclear-grade magnesium alloy during storage," University of Aberdeen, 2015.

## Appendix A Stability Analysis

In order to estimate the maximum time step that can be used that maintains stable calculations, stability analysis for the presented system of differential equations has to be performed. However, such analysis can be performed for linear equations where the nonlinear equations have to be linearized before initiating such analysis.

The typical stability analysis can be accomplished as follows:

- Construct the FDE (finite difference equation) for the model ODE,  $\dot{y} + \Phi y = 0$
- Determine the amplification factor,  $G$ , of the FDE.
- Determine the conditions to ensure that  $|G| < 1$ .

The change of the amount of the pond hall humid air can be expressed as:

$$\dot{N}_h = \dot{N}_{vent,in} + \dot{N}_{ev} - \dot{N}_{vent,out} \quad (A-1)$$

where  $\dot{N}_h$  is the rate of change of the amount of humid air inside the hall and  $\dot{N}_{vent,out}$  is the ventilation outlet flow molar rate and can be calculated from:

$$\dot{N}_{vent,out} = A_{duct} \sqrt{2\rho_\infty \left[ \left( \frac{T_h R_o}{V_h} \right) N_h - P_{atm} \right]} \quad (A-2)$$

Therefore Eq. (A-1) can be rewritten as:

$$\dot{N}_h = \dot{N}_{vent,in} + \dot{N}_{ev} - A_{duct} \sqrt{2\rho_\infty \left[ \left( \frac{T_h R_o}{V_h} \right) N_h - P_{atm} \right]} \quad (A-3)$$

Then,  $\dot{N}_h$  can be expressed in a Taylor series taking  $t_0$  as a base point.

$$\dot{N}_h \approx f_0 + f_t|_0(t - t_0) + f_{n_h}|_0(N_h - N_{h_0}) + \dots \quad (\text{A-4})$$

here  $N_{h_0}$  is the initial amount of humid air inside the pond hall and:

$$f_0 = \frac{P_t V_h}{T_h R_o} \quad (\text{A-5})$$

$$f_{n_h}|_0 = -\frac{A_{duct} R_o T_h}{2V_h} \sqrt{\frac{2\rho_\infty}{\left(\frac{T_h R_o}{V_h}\right) N_{h_0} - P_{atm}}} \quad (\text{A-6})$$

Eq. (A-4) can be rewritten as:

$$\dot{N}_h \approx f_0 - \frac{A_{duct} R_o T_h}{2V_h} \sqrt{\frac{2\rho_\infty}{\left(\frac{T_h R_o}{V_h}\right) N_{h_0} - P_{atm}}} (N_h - N_{h_0}) \quad (\text{A-7})$$

Let:

$$\emptyset = \frac{A_{duct} R_o T_h}{2V_h} \sqrt{\frac{2\rho_\infty}{\left(\frac{T_h R_o}{V_h}\right) N_{h_0} - P_{atm}}} \quad (\text{A-8})$$

Hence, Eq. (A-7) can be written as:

$$\dot{N}_h + \emptyset N_h \approx (f_0 + \emptyset N_{h_0}) \quad (\text{A-9})$$

Comparing this ODE with the model linear ODE ( $\dot{y} + \Phi y = 0$ ) and ignoring the non-homogenous term ( $f_0 + \emptyset N_{h_0}$ ) we can find that  $\Phi = \emptyset$ .

Hence, the amplification factors can be written as:

$$G = (1 - \phi \Delta t) \quad (\text{A-10})$$

For stability, the condition of  $|G| \leq 1$  must be satisfied, therefore:

$$\Delta t \leq \frac{2}{\phi} \quad (\text{A-11})$$

Note that  $\phi$  changes as  $N_{h_0}$  changes. Thus, the stable step size changes as the solution advances. Also, time step may vary depending on the configuration of heat and mass flow rate.

[REDACTED]

[REDACTED]

[REDACTED]

[REDACTED]

## Appendix C UDF for the Overall Heat Transfer Coefficient

/\*  
 \*\*\*\*\*  
 UDF Overall Heat Transfer Coefficient at water surface  
 Ahmed Ramadan  
 \*\*\*\*\*  
 \*/

UDF Overall Heat Transfer Coefficient at water surface

Ahmed Ramadan

\*\*\*\*\*  
 \*/

#include "udf.h"

DEFINE\_PROFILE(htc, thread, position)

#include "udf.h"

DEFINE\_PROFILE(htc, thread, position)

{

face\_t f;

real y = F\_T(f,thread); /\* surface temperature \*/

begin\_f\_loop(f, thread)

{

F\_PROFILE(f, thread, position) = 0.008\*y\*y-4.9612\*y+776.14;

end\_f\_loop(f, thread)

}